VERTICO: The Virgo Environment Traced in CO Survey

Brown, T.; Wilson, C.D.; Zabel, N.; Davis, T.A.; Boselli, A.; Chung, A.; ... ; Yoon, H.

Citation

Brown, T., Wilson, C. D., Zabel, N., Davis, T. A., Boselli, A., Chung, A., ... Yoon, H. (2021). VERTICO: The Virgo Environment Traced in CO Survey. *The Astrophysical Journal Supplement Series*, *257*(2). doi:10.3847/1538-4365/ac28f5

Draft version November 2, 2021
Typeset using LATEX **twocolumn** style in AASTeX63

arXiv:2111.00937v1 [astro-ph.GA] 1 Nov 2021

VERTICO: The Virgo Environment Traced In CO Survey

Toby Brown,[1, 2] Christine D. Wilson,[2] Nikki Zabel,[3] Timothy A. Davis,[4] Alessandro Boselli,[5] Aeree Chung,[6] Sara L. Ellison,[7] Claudia D.P. Lagos,[8, 9] Adam R.H. Stevens,[8] Luca Cortese,[8, 9] Yannick M. Bahé,[10] Dhruv Bisaria,[11] Alberto D. Bolatto,[12, 13] Claire R. Cashmore,[14] Barbara Catinella,[8, 9] Ryan Chown,[2] Benedikt Diemer,[15] Pascal J. Elahi,[16] Maan H. Hani,[2] María J. Jiménez-Donaire,[17, 18] Bumhyun Lee,[19] Katya Leidig,[12] Angus Mok,[20] Karen Pardos Olsen,[21] Laura C. Parker,[2] Ian D. Roberts,[10] Rory Smith,[22, 23] Kristine Spekkens,[24] Mallory Thorp,[7] Stephanie Tonnesen,[25] Evan Vienneau,[2] Vicente Villanueva,[15] Stuart N. Vogel,[12] James Wadsley,[2] Charlotte Welker,[26] and Hyein Yoon[27, 9]

[1] *Herzberg Astronomy and Astrophysics Research Centre, National Research Council of Canada, 5071 West Saanich Rd, Victoria, BC, V9E 2E7, Canada*
[2] *Department of Physics & Astronomy, McMaster University, 1280 Main Street W, Hamilton, ON, L8S 4M1, Canada*
[3] *Kapteyn Astronomical Institute, University of Groningen, PO Box 800, NL-9700 AV Groningen, the Netherlands*
[4] *School of Physics & Astronomy, Cardiff University, Queens Buildings, The Parade, Cardiff CF24 3AA, UK*
[5] *Aix-Marseille Université, CNRS, CNES, LAM, Marseille, France*
[6] *Department of Astronomy, Yonsei University, 50 Yonsei-ro, Seodaemun-gu, Seoul 03722, South Korea*
[7] *Department of Physics & Astronomy, University of Victoria, Finnerty Road, Victoria, BC, V8P 1A1, Canada*
[8] *International Centre for Radio Astronomy Research, The University of Western Australia, 35 Stirling Hwy, 6009 Crawley, WA, Australia*
[9] *ARC Centre of Excellence for All Sky Astrophysics in 3 Dimensions (ASTRO 3D), Australia*
[10] *Leiden Observatory, Leiden University, PO Box 9513, 2300 RA Leiden, The Netherlands*
[11] *Department of Physics, Engineering Physics and Astronomy, Queen's University, Kingston, ON K7L 3N6, Canada*
[12] *Department of Astronomy, University of Maryland, College Park, MD, 20742, USA)*
[13] *Visiting Scholar at Flatiron Institute, Center for Computational Astrophysics (NY 10010, USA)*
[14] *E.A. Milne Centre for Astrophysics, The University of Hull, Cottingham Road, Kingston-Upon-Hull, HU6 7RX, UK*
[15] *Department of Astronomy, University of Maryland, College Park, MD 20742, USA*
[16] *Pawsey Supercomputing Centre, Commonwealth Scientific and Industrial Research Organisation*
[17] *Observatorio Astronómico Nacional (IGN), C/Alfonso XII, 3, E-28014 Madrid, Spain*
[18] *Centro de Desarrollos Tecnológicos, Observatorio de Yebes (IGN), 19141 Yebes, Guadalajara, Spain*
[19] *Kavli Institute for Astronomy and Astrophysics, Peking University, Beijing 100871, China*
[20] *Department of Physics & Astronomy, The University of Toledo, Toledo, OH 43606, USA*
[21] *Department of Astronomy and Steward Observatory, University of Arizona, Tucson, AZ 85721, USA*
[22] *Korea Astronomy and Space Science Institute (KASI), 776 Daedeokdae-ro, Yuseong-gu, Daejeon 34055, Korea*
[23] *University of Science and Technology (UST), Daejeon 34113, Korea*
[24] *Royal Military College of Canada, PO Box 17000, Station Forces, Kingston, ON, Canada K7K 7B4*
[25] *CCA, Flatiron Institute, 162 5th Ave, New York NY 10010*
[26] *Department of Physics and Astronomy, Krieger School of Art and Science, The Johns Hopkins University, Baltimore, MD, USA*
[27] *Sydney Institute for Astronomy, School of Physics, University of Sydney, NSW 2006, Australia*

ABSTRACT

We present the Virgo Environment Traced in CO (VERTICO) survey, a new effort to map ^{12}CO$(2-1)$, ^{13}CO$(2-1)$, and C^{18}O$(2-1)$ in 51 Virgo Cluster galaxies with the Atacama Compact Array, part of the Atacama Large Millimeter/submillimeter Array (ALMA). The primary motivation of VERTICO is to understand the physical mechanisms that perturb molecular gas disks, and therefore star formation and galaxy evolution, in dense environments. This first paper contains an overview of VERTICO's design and sample selection, ^{12}CO$(2-1)$ observations, and data reduction procedures. We characterize global ^{12}CO$(2-1)$ fluxes and molecular gas masses for the 49 detected VERTICO galaxies, provide upper limits for the two non-detections, and produce resolved ^{12}CO$(2-1)$ data products (median

Corresponding author: Toby Brown
tobiashenrybrown@gmail.com

resolution $= 8'' \approx 640$ pc). Azimuthally averaged ^{12}CO$(2-1)$ radial intensity profiles are presented along with derived molecular gas radii. We demonstrate the scientific power of VERTICO by comparing the molecular gas size–mass scaling relation for our galaxies with a control sample of field galaxies, highlighting the strong effect that radius definition has on this correlation. We discuss the drivers of the form and scatter in the size–mass relation and highlight areas for future work. VERTICO is an ideal resource for studying the fate of molecular gas in cluster galaxies and the physics of environment-driven processes that perturb the star formation cycle. Upon public release, the survey will provide a homogeneous legacy dataset for studying galaxy evolution in our closest cluster.

1. INTRODUCTION

Beginning with the pioneering works of Gunn & Gott (1972), Cowie & Songaila (1977), and Larson et al. (1980), the last 50 years have seen a steady stream of work demonstrating that galaxies' cold gas and star formation properties are influenced by the environment in which they reside (see reviews by Haynes et al. 1984; Boselli & Gavazzi 2006; Cortese et al. 2021, and references therein).

Much of this work has focused on local galaxy clusters as laboratories for studying the role environment plays in galaxy evolution. Containing hundreds or even thousands of galaxies, clusters are characterized by high internal velocity dispersion ($v_{\rm disp} \sim 10^2 - 10^3$ km s^{-1}) and a hot, diffuse intracluster medium (ICM, T $\sim 10^7 - 10^8$ K, $n \sim 10^{-4}$ cm^{-3}; Kaiser 1986; White et al. 1997).

Cluster members are subject to a diverse range of environmental effects that drive the observed increase in quenched (or quenching) galaxies with respect to the field (Balogh et al. 1998, 1999; Gómez et al. 2003; Boselli & Gavazzi 2006). Dynamical interactions between two or more systems can cause tidal stripping of stars and gas (Moore et al. 1999; Iono et al. 2005) or compression of the interstellar medium (ISM; Nehlig et al. 2016; Kaneko et al. 2018). Harassment by frequent, high-velocity galaxy–galaxy encounters is capable of tidally heating the ISM, shutting off inflow and evaporating gas reservoirs (Moore et al. 1996, 1998; Fujita 1998). Viscous stripping or thermal evaporation of the cold gas content of galaxies surrounded by a hot ICM can also suppress star formation (Cowie & Songaila 1977; Livio et al. 1980; Nulsen 1982). Starvation occurs when there is a lack of gas cooling and/or a cut off in the external gas supply, either to the halo or to the galaxy itself, meaning reservoirs consumed in star formation are not replenished (Larson et al. 1980; Balogh et al. 2000; Bekki et al. 2002). For galaxies entering a cluster, the interaction between the ISM and ICM has been observed to be strong enough to rapidly remove gas from the disk via ram pressure stripping (Gunn & Gott 1972; Hester 2006; Chung et al. 2009a; Fumagalli et al. 2014). More recently, evidence has also been presented for elevated gas densities caused by ram pressure, affecting the star formation efficiency (SFE) and the transition of atomic hydrogen gas to its molecular phase (Ebeling et al. 2014; Lee et al. 2017; Mok et al. 2017; Vulcani et al. 2018; Moretti et al. 2020a,b).

The common outcome of such processes is that they leave different imprints on galaxies' cold gas reservoirs. Thus, to understand the nature of these effects, we must establish their influence upon the constituent phases of the ISM. Pursuit of this understanding has demonstrated the widespread and systematic depletion of atomic hydrogen (H I) gas reservoirs — considered the gas supply for future star formation—in cluster galaxies with respect to the field (e.g., Davies & Lewis 1973; Chamaraux et al. 1980; Giovanelli & Haynes 1985; Gavazzi et al. 2008; Chung et al. 2009a; Hughes & Cortese 2009; Cortese et al. 2011; Jaffé et al. 2016; Brown et al. 2017; Healy et al. 2020).

Similarly, there have been many efforts to determine cluster galaxies' molecular hydrogen gas (H_2) content, the fuel for on-going star formation. The low temperatures found in giant molecular gas clouds and lack of a dipole moment emission mechanism make the H_2 molecule very difficult to observe directly. Instead the bulk of molecular gas is usually traced via indirect means, the most common and reliable of which are the low-J rotational transitions of carbon monoxide (CO), although even this method is not without its uncertainties (see Bolatto et al. 2013, for a thorough review of this topic).

Because of the more stringent instrumental and observational requirements relative to longer-wavelength radio observations, the findings from studies of molecular gas have necessarily focused on smaller samples and lacked the consistency found in H I studies. A number of prominent early works using unresolved detections found no differences between the molecular gas content of field and cluster galaxies, concluding that molecular gas disks that are bound deep within the gravitational potential well of the system are largely immune to environmental effects (Stark et al. 1986; Kenney & Young 1986, 1989; Boselli et al. 1997). However, more recent efforts to survey global molecular gas reservoirs in a large number of local cluster galaxies tend to favour a scenario whereby the star-forming gas is depleted in dense environments, albeit to a lesser extent than the H I (Boselli et al. 2002; Wilson et al. 2009; Corbelli et al. 2012; Boselli et al. 2014; Mok et al. 2016; Chung et al. 2017; Koyama et al. 2017; Stevens et al. 2021).

Studies using resolved observations of molecular gas in a small number of systems generally support the picture of environmental mechanisms perturbing molecular gas reservoirs in clusters, and demonstrate that environmental influences often manifest themselves on the sub-kpc scale of bars, disks, streams, tails, and warps (e.g., Nehlig et al. 2016; Mok et al. 2017; Lee et al. 2017; Lee & Chung 2018; Moretti et al. 2018; Jáchym et al. 2019; Zabel et al. 2019; Cramer et al. 2019, 2020; Lizée et al. 2021). Interestingly, some of these studies find that environmental mechanisms have contrasting effects on the gas content or star formation properties of galaxies. For example, elevated star formation has been found at the ISM–ICM interface in cluster galaxies, implying that ram-pressure stripping is able to either increase the amount of gas available for star formation or the SFE of the surviving gas (or a combination of both; e.g., Ebeling et al. 2014; Nehlig et al. 2016; Zabel et al. 2020; Lizée et al. 2021). On the other hand, Moretti et al. (2018) find that ram-pressure stripping decreases the SFE of stripped molecular gas, and Mok et al. (2017) report enhanced molecular gas masses in cluster galaxies relative to the field (see also Moretti et al. 2020b), concluding that the environment is aiding the transition from atomic to molecular gas while lowering the SFE. Recent work attributes the triggering of active galactic nuclei (AGN) to central gas flows driven by ram pressure, suggesting a causal link between galaxy environment and energetic AGN feedback (Poggianti et al. 2017).

Despite continuous progression in our understanding, the dichotomy in approaches taken by molecular gas studies—large statistical surveys of global properties versus resolved mapping of gas reservoirs in a small number of galaxies—has left two significant questions unanswered:

1. What is the relationship between different environmental mechanisms and molecular gas density, morphology, kinematics, and chemistry?
2. When, where, and how do environmental mechanisms alter the rate and efficiency of star formation?

Answering these questions requires a merging of these two methodologies. In other words, we need resolved spectroscopic imaging of molecular gas disks across a large homogeneous sample of galaxies that are experiencing the full complement of environmental mechanisms. These observations must be combined with multi-wavelength data covering the full galactic ecosystem and accompanied by state-of-the-art models and simulations.

With this goal in mind, we present the Virgo Environment Traced in CO (VERTICO) survey, a Large Program with the Atacama Large Millimeter/submillimeter Array (ALMA) designed to map molecular gas in 51 Virgo Cluster galaxies on sub-kpc scales. The primary motivation of VERTICO is to understand the physical mechanisms that drive galaxy evolution in dense environments. We also aim to provide a homogeneous legacy dataset for studying galaxy evolution in the nearest massive cluster to the Milky Way.

This first paper contains an overview of the VERTICO survey design and sample selection, observations and data reduction procedures, global molecular gas properties, and derived data products. We present early science results on the radial distribution of molecular gas in VERTICO galaxies and compare the molecular gas disk sizes and masses to a control sample of field galaxies. We also highlight areas for future work. The paper is structured as follows: Section 2 presents the sample; Section 3 describes the observations, including our data reduction method and integrated CO properties; Section 4 gives the methodology and examples of key data products; Section 5 is a brief comparative analysis of molecular gas disk sizes and masses between VERTICO and a sample of field galaxies; finally, Section 6 presents a summary of this paper and looks forward to the next steps.

Throughout this paper, we assume a common distance of 16.5 Mpc to all Virgo galaxies based upon the Virgo Cluster distance found by Mei et al. (2007). Where relevant, all astrophysical quantities are derived using a Kroupa initial mass function (IMF; Kroupa 2001) or rescaled from literature values using

$$M_{\star,\,\mathrm{K}} = 1.06\ M_{\star,\,\mathrm{C}} = 0.62\ M_{\star,\,\mathrm{S}}, \qquad (1)$$

where the subscripts K, C, and S denote the Kroupa, Chabrier (2003), and Salpeter (1955) IMFs, respectively (Salim et al. 2007; Elbaz et al. 2007; Zahid et al. 2012; Speagle et al. 2014).

2. THE VERTICO SAMPLE

VERTICO targets 51 Virgo Cluster galaxies included in the Very Large Array Imaging of Virgo in Atomic gas (VIVA) survey (Chung et al. 2009a). The full VIVA survey contains 53 galaxies, however, we exclude two very low-mass systems (IC3355 and VCC2062) that were deemed unlikely to be detected. VIVA was selected by Chung et al. (2009a) to sample a range of star formation properties in the classification scheme published by

Koopmann & Kenney (2004, normal, enhanced, anemic, truncated), which is in turn based upon the spatial distribution of Hα and R-band emission. The resulting sample of primarily late-type galaxies spans a broad range in stellar mass ($10^{8.3} \leq M_\star/\mathrm{M}_\odot \leq 10^{11}$) and specific star formation rate (sSFR = SFR/$M_\star$; $10^{-11.5} \leq$ sSFR/yr^{-1} $\leq 10^{-9.5}$). VERTICO targets have existing resolved multi-wavelength observations tracing their stellar component, star formation activity, and H I gas content. Galaxy H I gas reservoirs exhibit signatures of the full complement of environmental effects, including the gas tails and truncated disks typical of stripping, fading gas disks of starvation, and morphological asymmetries and kinematic misalignment from gravitational perturbations (Chung et al. 2009a; Yoon et al. 2017). Every galaxy has existing resolved multi-wavelength observations tracing the stellar component and star formation activity (e.g., Wright et al. 2010; Alam et al. 2015; Martin et al. 2005, see Section 2.1 for further details). Furthermore, 15 galaxies already have archival Atacama Compact Array (ACA) observations of the ^{12}CO$(2-1)$ emission line, hereafter CO$(2-1)$. The remaining 36 targets were observable in CO$(2-1)$ within a feasible amount of time for an ALMA Large Program using the ACA. The full VERTICO sample is listed in Table 1. Optical inclinations and East-of-North position angles are calculated from fits to the Sloan Digital Sky Survey (SDSS; York et al. 2000; Alam et al. 2015) r-band photometry described in Section 4.2.

Table 1. The VERTICO target sample.

Galaxy	R.A. (J2000)	Dec. (J2000)	$v_{\rm opt}$ km s^{-1}	i °	P.A. °
IC3392*	$12^{\rm h}28^{\rm m}43.27^{\rm s}$	$14^\circ59'57.48''$	1678	68	219
IC3418*	$12^{\rm h}29^{\rm m}43.50^{\rm s}$	$11^\circ24'08.00''$	38	62	233
NGC4064	$12^{\rm h}04^{\rm m}11.26^{\rm s}$	$18^\circ26'39.12''$	1000	70	150
NGC4189*	$12^{\rm h}13^{\rm m}47.47^{\rm s}$	$13^\circ25'34.68''$	1995	42	70
NGC4192*	$12^{\rm h}13^{\rm m}48.58^{\rm s}$	$14^\circ53'57.12''$	-118	83	333
NGC4216*	$12^{\rm h}15^{\rm m}54.19^{\rm s}$	$13^\circ08'54.96''$	30	90	20
NGC4222	$12^{\rm h}16^{\rm m}22.56^{\rm s}$	$13^\circ18'25.20''$	225	90	238
NGC4254*†	$12^{\rm h}18^{\rm m}49.68^{\rm s}$	$14^\circ25'05.52''$	2453	39	243
NGC4293*†	$12^{\rm h}21^{\rm m}13.47^{\rm s}$	$18^\circ23'03.12''$	717	67	239
NGC4294	$12^{\rm h}21^{\rm m}17.81^{\rm s}$	$11^\circ30'39.24''$	421	74	151
NGC4298*†	$12^{\rm h}21^{\rm m}33.12^{\rm s}$	$14^\circ36'19.80''$	1122	52	132
NGC4299*	$12^{\rm h}21^{\rm m}40.71^{\rm s}$	$11^\circ30'06.12''$	209	14	128
NGC4302*	$12^{\rm h}21^{\rm m}42.24^{\rm s}$	$14^\circ35'57.12''$	1111	90	356
NGC4321*†	$12^{\rm h}22^{\rm m}54.77^{\rm s}$	$15^\circ49'33.24''$	1579	32	280
NGC4330	$12^{\rm h}23^{\rm m}16.95^{\rm s}$	$11^\circ22'04.08''$	1567	90	238
NGC4351*	$12^{\rm h}24^{\rm m}01.30^{\rm s}$	$12^\circ12'15.12''$	2388	48	251
NGC4380*	$12^{\rm h}25^{\rm m}22.16^{\rm s}$	$10^\circ01'00.12''$	935	61	158
NGC4383*	$12^{\rm h}25^{\rm m}25.47^{\rm s}$	$16^\circ28'11.64''$	1663	56	17
NGC4388	$12^{\rm h}25^{\rm m}46.61^{\rm s}$	$12^\circ39'46.44''$	2538	83	271
NGC4394	$12^{\rm h}25^{\rm m}55.66^{\rm s}$	$18^\circ12'52.20''$	772	32	312
NGC4396*	$12^{\rm h}25^{\rm m}59.66^{\rm s}$	$15^\circ40'10.20''$	-115	83	304
NGC4402†	$12^{\rm h}26^{\rm m}07.34^{\rm s}$	$13^\circ06'45.00''$	190	80	270
NGC4405	$12^{\rm h}26^{\rm m}07.11^{\rm s}$	$16^\circ10'51.60''$	1751	46	18
NGC4419	$12^{\rm h}26^{\rm m}56.35^{\rm s}$	$15^\circ02'51.36''$	-228	74	131
NGC4424*†	$12^{\rm h}27^{\rm m}11.69^{\rm s}$	$09^\circ25'14.16''$	447	61	274

Table 1 *continued*

Table 1 *(continued)*

Galaxy	R.A. (J2000)	Dec. (J2000)	$v_{\rm opt}$	i	P.A.
			km s^{-1}	°	°
NGC4450[*]	$12^{\rm h}28^{\rm m}29.23^{\rm s}$	$17^\circ05'04.56''$	2048	51	170
NGC4457[*†]	$12^{\rm h}28^{\rm m}59.02^{\rm s}$	$03^\circ34'14.16''$	738	37	256
NGC4501[*]	$12^{\rm h}31^{\rm m}59.33^{\rm s}$	$14^\circ25'10.92''$	2120	65	320
NGC4522	$12^{\rm h}33^{\rm m}39.72^{\rm s}$	$09^\circ10'26.76''$	2332	82	35
NGC4532[*]	$12^{\rm h}34^{\rm m}19.35^{\rm s}$	$06^\circ28'05.52''$	2154	64	159
NGC4533	$12^{\rm h}34^{\rm m}22.03^{\rm s}$	$02^\circ19'33.24''$	1753	80	342
NGC4535[*†]	$12^{\rm h}34^{\rm m}20.26^{\rm s}$	$08^\circ11'53.52''$	1973	48	12
NGC4536[*†]	$12^{\rm h}34^{\rm m}27.12^{\rm s}$	$02^\circ11'16.08''$	1894	74	118
NGC4548[*†]	$12^{\rm h}35^{\rm m}26.64^{\rm s}$	$14^\circ29'43.80''$	498	37	318
NGC4561[*]	$12^{\rm h}36^{\rm m}08.14^{\rm s}$	$19^\circ19'21.72''$	1441	28	60
NGC4567	$12^{\rm h}36^{\rm m}33.07^{\rm s}$	$11^\circ15'29.16''$	2213	49	251
NGC4568[*]	$12^{\rm h}36^{\rm m}34.34^{\rm s}$	$11^\circ14'21.84''$	2260	70	211
NGC4569[*†]	$12^{\rm h}36^{\rm m}50.12^{\rm s}$	$13^\circ09'55.08''$	-220	69	203
NGC4579[*†]	$12^{\rm h}37^{\rm m}43.44^{\rm s}$	$11^\circ49'05.52''$	1627	40	273
NGC4580[*]	$12^{\rm h}37^{\rm m}48.38^{\rm s}$	$05^\circ22'06.24''$	1227	46	337
NGC4606	$12^{\rm h}40^{\rm m}57.62^{\rm s}$	$11^\circ54'43.56''$	1653	69	38
NGC4607	$12^{\rm h}41^{\rm m}12.39^{\rm s}$	$11^\circ53'09.60''$	2284	90	2
NGC4651[*]	$12^{\rm h}43^{\rm m}42.72^{\rm s}$	$16^\circ23'37.68''$	788	53	75
NGC4654[*†]	$12^{\rm h}43^{\rm m}56.76^{\rm s}$	$13^\circ07'32.52''$	1035	61	300
NGC4689[*†]	$12^{\rm h}47^{\rm m}45.68^{\rm s}$	$13^\circ45'42.12''$	1522	38	341
NGC4694[*†]	$12^{\rm h}48^{\rm m}15.08^{\rm s}$	$10^\circ59'00.60''$	1211	62	323
NGC4698[*]	$12^{\rm h}48^{\rm m}22.99^{\rm s}$	$08^\circ29'15.00''$	1032	66	347
NGC4713[*]	$12^{\rm h}49^{\rm m}57.65^{\rm s}$	$05^\circ18'39.60''$	631	45	89
NGC4772	$12^{\rm h}53^{\rm m}29.12^{\rm s}$	$02^\circ10'06.24''$	1042	60	325
NGC4808[*]	$12^{\rm h}55^{\rm m}48.94^{\rm s}$	$04^\circ18'15.12''$	738	72	127
VCC1581	$12^{\rm h}34^{\rm m}45.05^{\rm s}$	$06^\circ18'03.24''$	2141	43	329

Note—Columns are (1) galaxy name and unique identifier in this paper; (2) right ascension (J2000) of the galaxy optical center; (3) declination (J2000) of the galaxy optical center; (4) optical heliocentric recession velocity; (5) optical $r-$band inclination; (6) optical $r-$band position angle of the kinematically redshifted half of the galaxy, calculated East-of-North. Columns (2)—(4) are drawn from the NASA/IPAC Extragalactic Database (https://ned.ipac.caltech.edu/). Columns (5) and (6) are calculated using fits to SDSS photometry described in Section 4.2. This table is published in its entirety in machine-readable format.

[*] Data are from 7m and Total Power arrays. Other observations are 7m array only.

[†] Data are archival ALMA ACA (7m + total power) ^{12}CO$(2-1)$ observations at comparable sensitivity to our Cycle 7 observations. The sources of these data are the PHANGS-ALMA program (Leroy et al. 2021a, 14 galaxies) and one regular PI program (Cramer et al. 2019, NGC4402). See Section 3 and the Acknowledgments section for further details.

2.1. *The Virgo Cluster*

The Virgo Cluster resides at a distance of 16.5 Mpc and contains thousands of member galaxies, making it the closest massive galaxy cluster to the Milky Way. The main body of the cluster centered on M87 has an estimated mass $M_{200} = 10^{14-14.6}$ $\mathrm{M}_\odot$ and radius $r_{200} = 1.08 - 1.55$ Mpc (Böhringer et al. 1994; Nulsen & Bohringer 1995; Girardi et al. 1998; Schindler et al. 1999; McLaughlin 1999; Gavazzi et al. 1999; Mei et al. 2007; Urban et al. 2011; Kim et al. 2014; Boselli et al. 2018), where M_{200} is the total mass within r_{200}, the radius at which the enclosed mean mass density is 200 times the critical cosmic mass density. A comprehensive list of mass, size, and distance estimates for Virgo is provided by Boselli et al. (2018, table 1 in that work). The cluster is dynamically young, contains significant substructure and is actively accreting members. This ensures Virgo's membership includes both infalling and virialised systems on a wide range of orbits throughout the cluster (Tully & Shaya 1984; Gavazzi et al. 1999; Karachentsev et al. 2014; Sorce et al. 2016; Yoon et al. 2017; Morokuma-Matsui et al. 2021).

For these reasons, the Virgo region has been remarkably well surveyed at almost every wavelength: X-ray (ROSAT – Böhringer et al. 1994; ASCA – Shibata et al. 2001; XMM-Newton – Urban et al. 2011), ultra-violet (UV; the GALEX Ultra-violet Virgo Cluster Survey, GUViCS – Boselli et al. 2011), optical (SDSS – York et al. 2000; the Next Generation Virgo Survey, NGVS – Ferrarese et al. 2012; the Virgo Environmental Survey Tracing Ionised Gas Emission, VESTIGE – Boselli et al. 2018), infrared (the Wide-field Infrared Survey Explorer, WISE – Wright et al. 2010; the Herschel Reference Survey, HRS – Boselli et al. 2010; the Herschel Virgo Cluster Survey, HeViCS – Davies et al. 2010) and 21 cm radio (VIVA; Chung et al. 2009a). These surveys map the hot ICM, and the stellar mass, dust, SFR, and atomic and ionized gas properties of Virgo members in extraordinary detail. Almost all these data have VERTICO's angular resolution or better, while the 21 cm observations are coarser ($\sim 15''$). This combination of richness, proximity, wavelength coverage, and data quality is not available for any other galaxy cluster.

At mm wavelengths, Boselli et al. (2014) provide a census of unresolved CO$(1-0)$ observations and global molecular gas properties for approximately 150 Virgo members, showing that Virgo galaxies are, on average, deficient in molecular gas in comparison to similar field galaxies. Resolved studies of CO$(2-1)$ and CO$(3-2)$ have mapped the distribution of molecular gas at 1–2 kpc scale in ~ 30 late-type cluster members (Pappalardo et al. 2012; Mok et al. 2017) and there are also published sub-kiloparsec resolution CO$(2-1)$ observations for a handful of Virgo spirals (Lee et al. 2017; Cramer et al. 2020; Lizée et al. 2021). The key contribution of VERTICO to this field is homogeneous observations of molecular gas at sub-kiloparsec resolution for a large sample of cluster galaxies.

2.2. *Sample Properties*

The global stellar mass and star formation rate (SFR) estimates used in this paper are drawn from the $z = 0$ Multi-wavelength Galaxy Database (z0MGS; Leroy et al. 2019). They were downloaded via the NASA/IPAC Infrared Science Archive[1]. The SFRs are derived from GALEX NUV and WISE band 4 (22 μm) luminosities, while the stellar masses are based upon a variable WISE band 1 (3.4 μm) mass-to-light ratio predicted using the specific SFR-like quantity, SFR-to-WISE band 1 luminosity. Global H I mass estimates are taken from the VIVA survey. The median uncertainties are 0.1 dex for stellar and H I mass, and 0.2 dex for SFR. One galaxy, IC3418, is not included in the z0MGS, so we adopt the literature values of $M_\star = 10^{8.37}$ $\mathrm{M}_\odot$ and SFR $= 0.1$ $\mathrm{M}_\odot$ yr^{-1} (Fumagalli et al. 2011; Jáchym et al. 2013). These properties are derived using spectral energy distribution fits to optical and UV observations, and a far-UV luminosity–SFR relation modified for dwarf galaxies. Without formal uncertainties quoted in these works, we assign an uncertainty of 0.3 dext to the logarithmic values of stellar mass and SFR for IC3418.

Figure 1 presents the scaling relations between and distributions of global stellar mass, sSFR, and H I properties of the VERTICO sample (blue points and histograms). We compare the VERTICO sample with the 1,179 galaxies in the extended GALEX Arecibo SDSS Survey (xGASS, grey distributions) that have their 'best' SFR measurement within that catalog and including H I non-detections as 3σ upper limits (Catinella et al. 2018)[2]. Following Catinella et al. (2018), the xGASS sample is weighted to correct for the flat stellar mass distribution and recover a volume-limited sample for $M_\star \geq 10^9$ $\mathrm{M}_\odot$ and $z \leq 0.05$. The lower left panel shows the normalized distribution of stellar mass for both samples. Barring two galaxies (IC3418, VCC1581), VERTICO targets have $M_\star \geq 10^9$ $\mathrm{M}_\odot$. Compared to the representative xGASS sample, VERTICO has an excess of galaxies above $M_\star \sim 10^{10}$ $\mathrm{M}_\odot$. The stellar mass–sSFR relation is provided in the upper left and the sSFR distribution is shown in lower center. VERTICO contains galaxies that are either star-forming (i.e., blue cloud) or transitioning from star-forming towards

---

[1] https://irsa.ipac.caltech.edu/data/WISE/z0MGS/overview.html

[2] https://xgass.icrar.org/

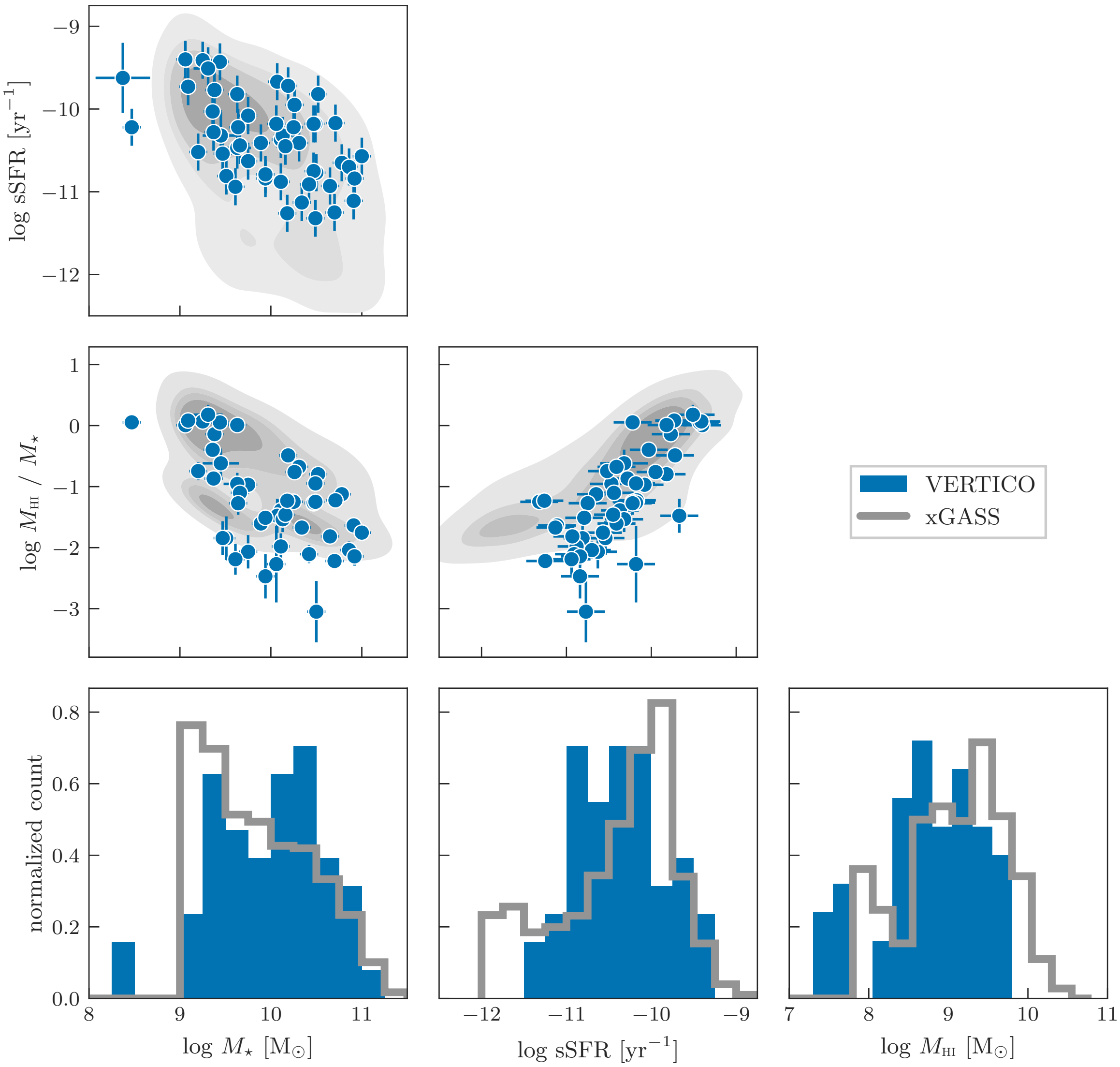

Figure 1. Global properties of the VERTICO sample (blue points and histograms) compared to the representative xGASS survey (grey distributions, 1179 galaxies; Catinella et al. 2018). Left to right from the upper left; sSFR vs. stellar mass, H I gas fraction vs. stellar mass, H I gas fraction vs. sSFR, the normalized stellar mass, sSFR, and H I mass distributions. Panels in the same row share the same y-axis range.

quiescence (i.e., green valley) with no systems that are already quenched (sSFR $\leq 10^{-11.5}$ yr^{-1}). We note that this bias towards star-forming or transitioning galaxies is by selection, with the VIVA survey not including quenched or early-type galaxies. Atomic gas fractions ($M_{\rm HI}/M_\star$) as a function of stellar mass and sSFR are shown in the left and center panels of the second row, respectively. VERTICO galaxies exhibit a broad range in H I gas fraction for their stellar and star formation properties, spanning ~ 3 dex in gas fraction at both fixed stellar mass and sSFR. The distribution of $M_{\rm HI}$ in the lower right panel shows that the VERTICO sample is marginally offset to lower H I gas masses compared to the representative xGASS sample. Yoon et al. (2017) demonstrate that the majority of the VIVA (and therefore the VERTICO) sample entered the cluster relatively recently (i.e., are not yet virialized). Combined with the targeting of late-type galaxies that were likely to be detected in H I, this naturally results in an absence of passive systems. Indeed, in the SFR–$M_\star$ parameter space, Mun et al. (2021) show that the Virgo Cluster has a well-populated quiescent sequence that is not sampled by VIVA. Given we are missing the bulk of the passive, gas-poor population, our sample thus cannot be considered representative of Virgo's entire population. This is by construction with the sample selection designed to target galaxies that are either being, will be, or recently have been actively quenched. Despite the star-forming nature of the sample, VERTICO probes a large range in H I gas fraction, covering the full gas-rich to gas-poor parameter space at both fixed stellar mass and sSFR.

Figure 2 shows the ROSAT All Sky Survey mosaic of the Virgo Cluster (hard band: 0.4–2.4 keV) with the VERTICO CO$(2-1)$ peak temperature maps overlaid. ROSAT images and exposure maps were obtained from NASA's High Energy Astrophysics Science Archive Research Center[3]. An exposure-corrected X-ray mosaic of the Virgo cluster area was produced with the `reproject_image_grid` function from the Chandra Interactive Analysis of Observations[4] software package (CIAO; Fruscione et al. 2006). This mosaic was then adaptively smoothed to emphasize emission on different scales with the CIAO function `csmooth` (Ebeling et al. 2006). The figure shows VERTICO CO$(2-1)$ peak temperature maps at the locations of the target galaxies relative to the ROSAT image. VERTICO galaxies are distributed throughout the Virgo Cluster with a large range of cluster-centric radii ($\sim 0.2 - 2\times\ r_{200}$). For illustration, the angular size of the VERTICO maps has been increased by a factor of twenty. See Section 4 for a full description of the CO maps.

3. OBSERVATIONS

We observed 36 targets in CO$(2-1)$, ^{13}CO$(2-1)$, C^{18}O$(2-1)$, and ALMA Band 6 continuum in ALMA Cycle 7. We set a spectral bandwidth of 1875 MHz to ensure we cover emission from the target itself and potential interactions. We average the basic Frequency Division Mode channel spacing by a factor of four to achieve a raw spectral resolution of 1.953 MHz $\approx$ 2.5 km s^{-1}. We bin by a further factor of four during the data processing to yield cubes with a final resolution of $\sim$ 10 km s^{-1}. While all lines are observed with the same bandwidth and approximate channel width, tuning constraints on the spectral setup means that we do not require the line frequencies to be in the center of the spectral window. The target galaxies are combined with archival ACA CO$(2-1)$ data (7-m and Total Power arrays) for 14 massive Virgo Cluster spirals from the ALMA component of the Physics at High Angular resolution in Nearby Galaxies project (PHANGS-ALMA; Leroy et al. 2021a) and one from a regular program (2016.1.00912.S; Cramer et al. 2020) to make the final VERTICO sample of 51 galaxies.

Observations and theory suggest that gas transitions from predominantly atomic to molecular at $\sim$ 10 M$_\odot$ pc^{-2} at solar metallicity (Leroy et al. 2008; Krumholz et al. 2009). CO$(3-2)$ James Clerk Maxwell Telescope (JCMT) 15$''$ observations of 13 H I-selected Virgo galaxies demonstrate H$_2$ surface densities of $\sim$ 6 M$_\odot$ pc^{-2} at the outskirts of molecular disks (Mok et al. 2017). We choose a 5σ sensitivity limit of 8.5 M$_\odot$ pc^{-2} per 10 km s^{-1} channel, ensuring we detect the diffuse gas that is below the atomic-to-molecular transition density and most susceptible to environmental influence. This mass surface density sensitivity corresponds to a root mean square (rms) of 10.6 mJy beam^{-1} per 10 km s^{-1} channel. The total integration time required to successfully reach this sensitivity across all 36 Cycle-7 targets was 186.5 hours. Each galaxy was observed with a mosaic (between three and 31 pointings with an average of 13) with Nyquist spacing. We obtained Total Power observations for 25 out of 36 Cycle-7 targets where galaxy CO disks were expected to extend more than 29$''$.

3.1. *Data Reduction*

For the galaxies in the VERTICO Cycle-7 sample, we used the calibrated *uv* data delivered by ALMA and we imaged all the available $J = 2-1$ CO lines [CO$(2-1)$, ^{13}CO$(2-1)$, C^{18}O$(2-1)$]. All galaxies were observed with ACA mosaics. The spatial extent of each mosaic was set to cover the CO$(3-2)$ emission from the JCMT–Next Generation Virgo Legacy Survey (JCMT–NGLS; Wilson et al. 2009) if available, or the Herschel Spectral and Photometric Imaging Receiver (SPIRE) 250μm flux maps published by Ciesla et al. (2012) and downloaded from the Herschel Database in Marseille[5]. For the 14 VERTICO targets that are also part of PHANGS-ALMA [which have CO$(2-1)$, C^{18}O$(2-1)$, ACA 7m and Total Power data], as well as for the one archival target that was not part of PHANGS-ALMA [NGC4402; CO$(2-1)$ only, no Total Power data], we retrieved the raw ACA *uv* data from the ALMA archive and calibrated it using CASA version 5.6. Th ree of these galaxies (NGC4254, NGC4321, NGC4535) remained in ALMA quality assurance (QA3) at the time of VERTICO imaging and the calibrated *uv* data for these galaxies were kindly provided to us in private communication by Adam Leroy on behalf of the PHANGS-ALMA team. The ^{13}CO$(2-1)$ and C^{18}O$(2-1)$ observations have been processed in the same manner as the CO$(2-1)$ data. However, the presentation of those data, along with an expanded analysis using spectral stacking, will be the focus of future work.

To image the VERTICO ACA data, we used the PHANGS-ALMA Imaging Pipeline Version 1.0 (Leroy

---

[3] https://heasarc.gsfc.nasa.gov/

[4] https://cxc.cfa.harvard.edu/ciao/

[5] http://hedam.lam.fr

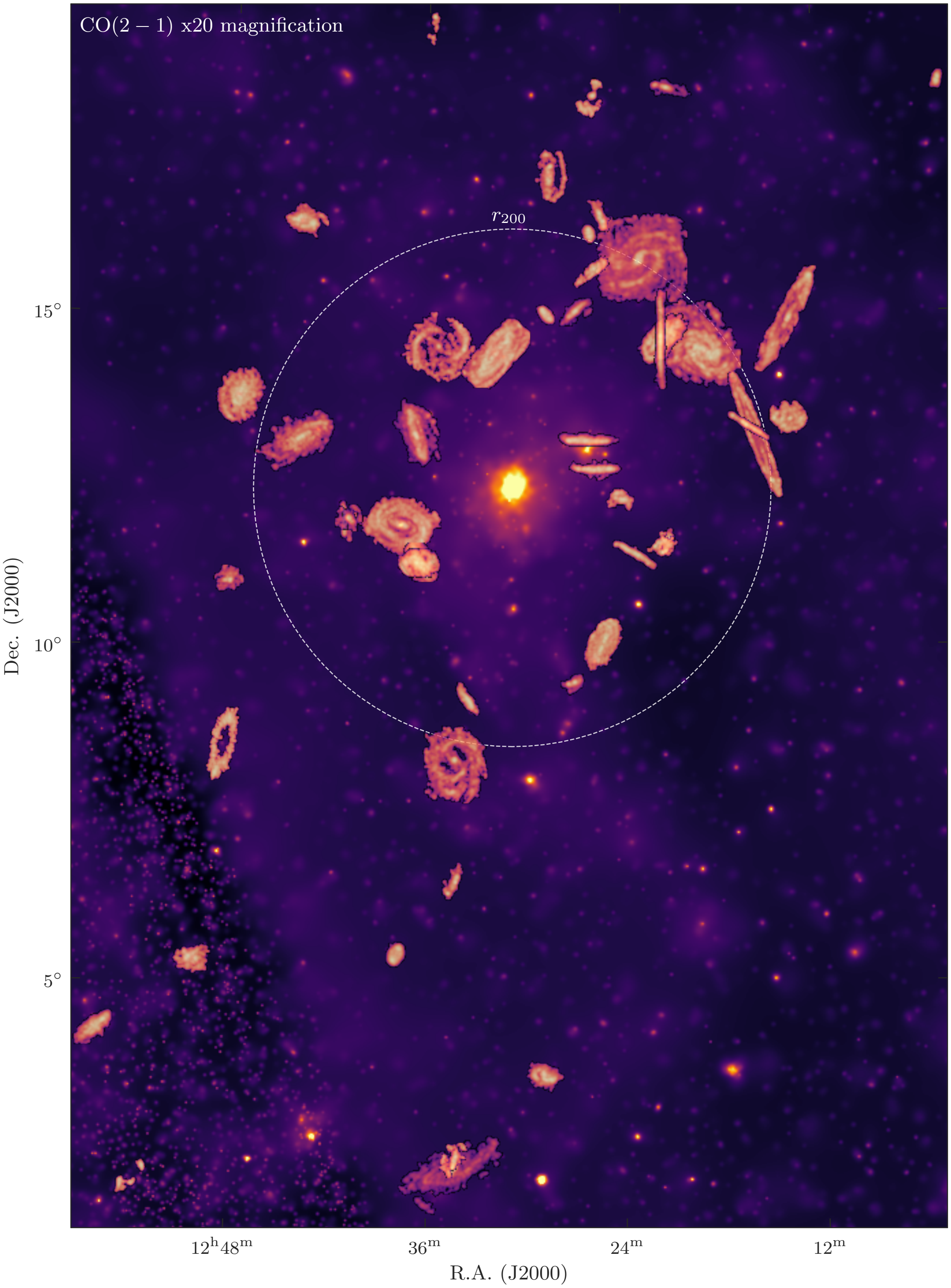

Figure 2. Background-subtracted, exposure-corrected ROSAT All Sky Survey mosaic of the Virgo Cluster (hard band: 0.4 − 2.4 keV). We overlay the VERTICO CO(2 − 1) peak temperature maps for the 49 detected galaxies, increased in angular size by a factor of 20 for illustration. CO(2 − 1) observations of three galaxies (NGC4254, NGC4321, NGC4501) do not cover the full extent of the CO disk and, as such, their peak temperature maps are rectangular in shape. The white dashed circle denotes the radius of the Virgo cluster, $r_{200} = 3.9°$ (∼ 1.08 Mpc; Urban et al. 2011).

et al. 2021b) with three modifications to adapt the pipeline for these ACA-only images (note that the PHANGS survey and pipeline papers, as well as delivered data products, use and describe Version 2.0 of this pipeline). First, we added a continuum subtraction step to the PHANGS-ALMA pipeline. For 26 galaxies where the delivered products from ALMA suggested the continuum was detected, we applied continuum subtraction in *uv* space to perform a first-order fit to the line-free channels across all spectral windows. Second, we removed the steps in building the single-scale clean mask where the mask was expanded in velocity space. This change was necessary to keep the mask from expanding out to include strong sidelobes present in some of the VERTICO data. Third, in addition to the maximum resolution cubes produced by the pipeline (median resolution = 8″), we also produced data cubes with a 9″ beam [CO$(2-1)$ only, and excluding NGC4321 where the maximum resolution is 10″] and a 15″ beam (all lines). As a guide, $1'' \approx 80$ pc at the distance of Virgo. For simplicity, these lower-resolution cubes were produced using the CASA task `imsmooth` rather than applying a *uv* taper at the initial imaging stage.

For VERTICO imaging, we use Briggs weighting (robust= 0.5; Briggs 1995) and set the target velocity resolution to be 10 km s^{-1} with the local standard of rest (LSR) as our velocity reference frame, using the radio definition of velocity. We defined the reference phase center to be the centroid pixel determined from a map of the two-dimensional primary beam response in a single velocity channel. This step was necessary as the phase centers specified in the observing stage were not always at the precise center of the resulting image mosaic. Using the observed offset phase center could produce a mildly to strongly asymmetric shape and sidelobe response of the point spread function (PSF). We first carried out a multi-scale clean down to S/N = 4, followed by a single-scale clean down to S/N = 1 in masked regions. All cubes were visually inspected for obvious problems or imaging errors. ALMA Band 6 observations have a $5-10\%$ flux calibration uncertainty[6].

For the Total Power data for galaxies in the VERTICO Cycle-7 sample, we started with the raw data delivered by ALMA and used version 1.0 of the PHANGS-ALMA Total Power pipeline (Herrera et al. 2020; Leroy et al. 2021b). The only modification we made to the pipeline was to remove the initial velocity binning, so that the Total Power data were processed at their native velocity resolution of ~ 3 km s^{-1}. We typically imaged a range of 1000 km s^{-1} around the mean velocity of the galaxy. We then fit and removed a first-order baseline using the highest and lowest 200 km s^{-1} of the cube. For five galaxies (IC3392, NGC4380, NGC4383, NGC4580, NGC4651), the baseline region was shifted to avoid an atmospheric ozone line. For two galaxies (NGC4302, NGC4698), the ozone line overlaps with the CO$(2-1)$ line at some velocities and so the Total Power fluxes for those galaxies are less reliable. All Total Power cubes were inspected to check for any problems in the data reduction. For the PHANGS-VERTICO galaxies, calibrated Total Power cubes were kindly provided to us by Adam Leroy on behalf of the PHANGS-ALMA team in private communication.

For all galaxies and lines for which Total Power data were available, the Total Power data were combined with the ACA data via feathering using the PHANGS-ALMA pipeline. This technique is described in full in section 6 of Leroy et al. (2021b). The final high-resolution data cubes were binned by a factor of two to produce ≥ 3 pixels across the beam. We also produced data cubes binned by factors of four (for the native and 9″ resolution images) and eight (for the 15″ resolution images).

As an example, Figure 3 shows the integrated intensity channel maps for NGC4380. Each channel is 10.6 km s^{-1} wide with the channel systemic velocity shown in the bottom right corner of each panel. The maps span the velocity range over which we detect CO$(2-1)$ emission. The color scale is fixed from channel to channel.

4. DERIVED DATA PRODUCTS

We calculate moment maps, position–velocity diagrams, and radial profiles for each galaxy from a masked signal cube. The masking process follows a revised version of the signal identification scheme described in Sun et al. (2018). This method uses a spatially and spectrally varying noise estimate (i.e., we estimate the noise at each pixel in every channel) computed from the signal cubes before primary beam correction and is described in detail in Section 7.2 of Leroy et al. (2021b). The original code is publicly available[7] and the steps are as follows:

1. Generate a core mask for spaxels with S/N ≥ 3.5 in at least three consecutive channels.

2. Generate a wing mask for spaxels with S/N ≥ 2 in at least two consecutive channels.

---

[6] See Chapter 10 in the ALMA Cycle 7 Technical Handbook https://almascience.nrao.edu/documents-and-tools/cycle7/alma-technical-handbook/

[7] https://github.com/astrojysun/Sun_Astro_Tools/tree/master/sun_astro_tools

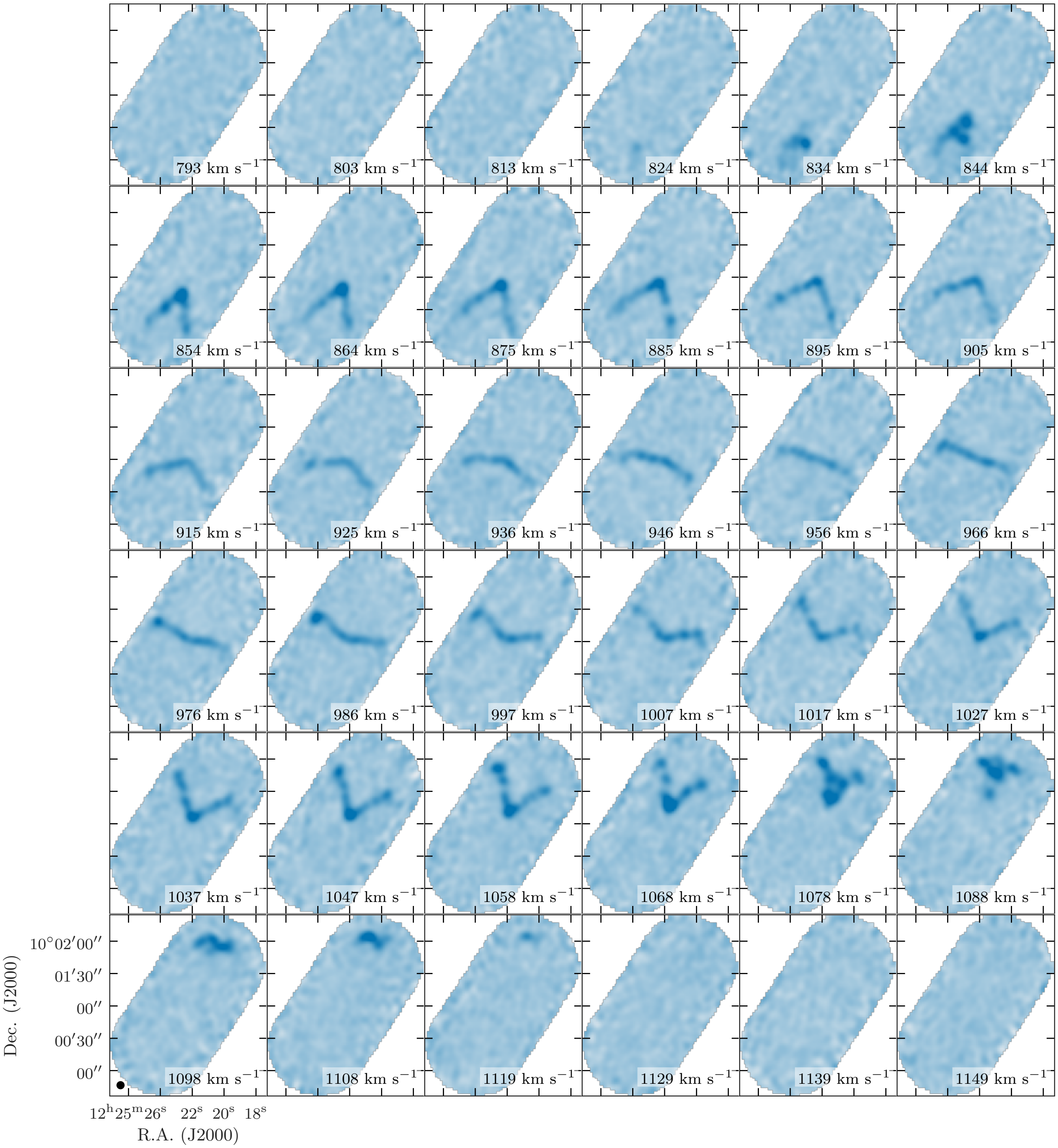

Figure 3. Channel maps for NGC4380. The circular beam size illustrated in the lower left panel is 7.5″, the channel width is 10.6 km s^{-1}, and the rms intensity in one channel is 3.5 mK. The systemic velocity of each channel is given in the lower right-hand corner. The color scale is fixed between channels.

3. Combine the core mask with the wing mask to define a signal mask that encapsulates all detected spaxels.
4. Prune spaxels from the signal mask if the projected area of connected neighbors on the sky is smaller than one beam.
5. Expand the signal mask along the spatial dimensions by a given number of pixels or a fraction of the beam size.
6. Expand the signal mask by two velocity channels.
7. Apply the final signal mask to produce a signal cube from which all moments are calculated.

We now describe the science-ready data products that are derived from these masked cubes.

4.1. *Moment Maps*

We compute the zeroth, first, second, and eighth-order two-dimensional moment maps from the CO$(2-1)$ spectral line cubes. In order, these are:

- Integrated intensity of the spectrum along the spectral axis in K km s^{-1}.
- Intensity weighted spectral coordinate in km s^{-1}, often referred to as the velocity field.
- Observed line width (σ_v, i.e., not corrected for broadening) along the spectral axis in km s^{-1}.
- Peak brightness temperature value of the spectrum in K.

Although not shown in this paper, we calculate statistical uncertainty maps for the pixel-by-pixel integrated intensity, velocity field, and observed line width maps. The uncertainty on the integrated intensity is

$$u_I = \sqrt{N}\sigma_T \Delta v \,, \tag{2}$$

where N is the number of channels included in the mask, σ_T the rms uncertainty across the integrated intensity map, and Δv is the velocity channel width. We then compute the uncertainty on the velocity field,

$$u_{\rm vel} = \frac{\Delta v_{\rm line}}{2\sqrt{3}} \frac{u_I}{I} \,, \tag{3}$$

where I is the integrated intensity and $\Delta v_{\rm line}$ the spectral line width over which $u_{\rm vel}$ is calculated. The uncertainty on the observed line width is given by

$$u_{\sigma_v} = \frac{u_I}{I} \frac{(\Delta v_{\rm line})^2}{8\sqrt{5}} \frac{1}{\sigma_v} \,, \tag{4}$$

where σ_v is the observed line width map. The derivation for these equations is provided in Wilson et al. (2021, in prep.).

Figure 4 illustrates the high quality of the VERTICO CO$(2-1)$ moment maps for NGC4380. An archetypal unbarred-spiral, we choose this galaxy to showcase the VERTICO as it appears to be relatively unperturbed by its environment and has a bright, extended CO$(2-1)$ gas disk. The left panel shows the SDSS *gri* composite image with molecular gas surface brightness contours at the 10th, 50th, and 90th percentiles. The integrated intensity, velocity field, peak temperature, and observed CO$(2-1)$ line width maps are provided clockwise from the top middle panel. We calculate NGC4380's r-band inclination to be 61°. Equivalent panel plots of the CO data products for the 49 detected VERTICO galaxies are **in the online version of Figure 4**.

The synthesized 7.5″ beam of the NGC4380 data corresponds to approximately 600 pc at the distance of Virgo (16.5 Mpc). On this scale, the VERTICO observations reveal the imprint of stellar structure in the molecular gas distribution of NGC4380 in glorious detail. The Northern and North-Eastern outskirts of the gas disk have a ridge of emission that is not found on the opposing side of the galaxy. We can also see a strong CO feature straddling the nucleus from the South East to the North West. Examining the central region in the peak temperature map shows there are two symmetrical peaks of CO emission such as those commonly found in the centers of barred galaxies (e.g., Kenney et al. 1992; Muraoka et al. 2016).

4.2. *Position–Velocity Diagrams*

We create major- and minor-axis position–velocity diagrams (PVD) from the CO$(2-1)$ signal cubes. The major-axis position angles are provided in Table 1 and were derived by fitting Kron ellipses to the background-subtracted, masked SDSS r-band images using the Photutils Python package (Bradley et al. 2020). All Kron ellipses pass visual inspection to ensure a robust fit before being used. The position–velocity slit width is set to one beam width for each galaxy.

Figure 5 shows both PVDs for NGC4380. The two x-axes denote the positional offset about the optical center of the galaxy (provided in Table 1) in physical and angular units. The major-axis PVD is shown in the upper panel and reveals the increase in high velocity emission at negative offsets compared to positive offsets. This asymmetry is also apparent in the Northern regions of the peak temperature map in Figure 4 and is discussed in Section 4.1. The asymmetry that shows higher brightness temperatures at positive relative velocity offsets in

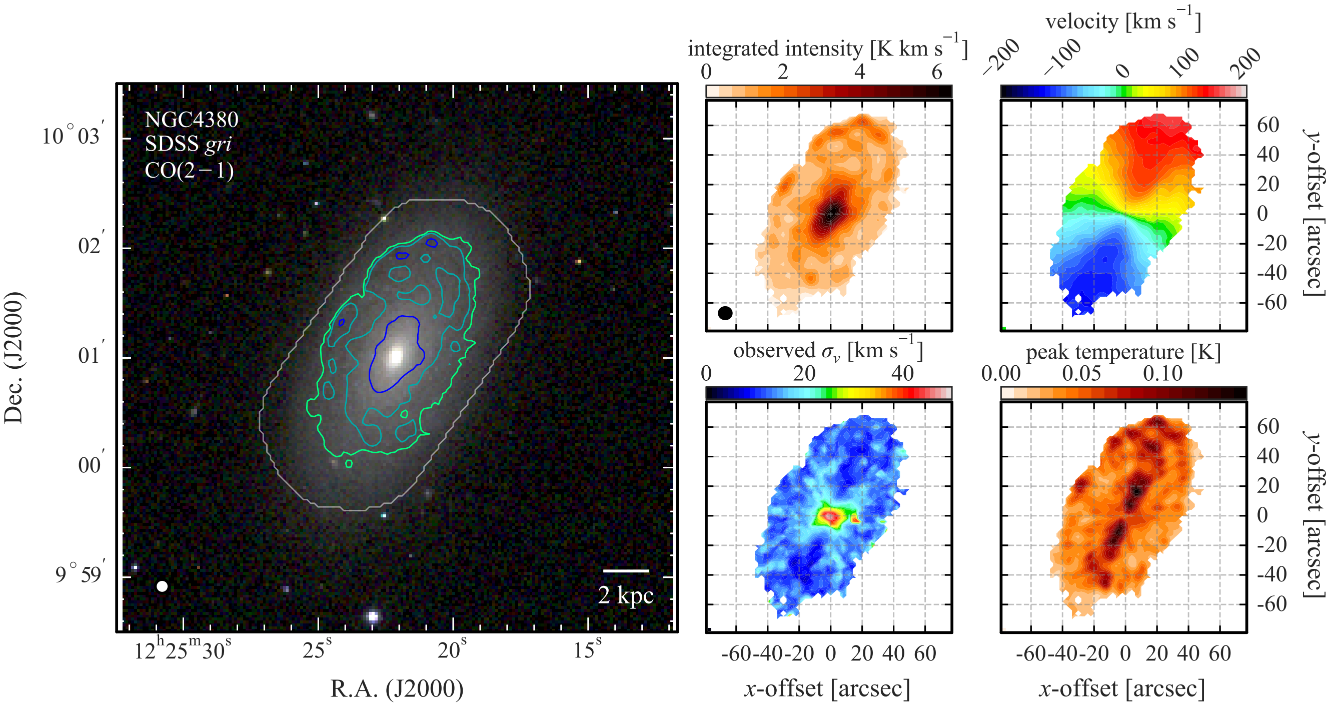

Figure 4. An example of the CO(2 − 1) data products available for each galaxy in the VERTICO survey. The left panel shows the SDSS *gri* composite image for NGC4380 with molecular gas surface brightness contours at the 10th, 50th, and 90th percentiles of the distribution. The field of view of the ACA observations is defined where the primary beam response drops to 50% and is illustrated by the gray line. The rounded synthesized beam is 7.5″ in diameter and illustrated in the bottom left corner. This beam corresponds to ∼600 pc at the distance of Virgo (16.5 Mpc). The VERTICO CO(2 − 1) data products available for each galaxy include maps of integrated intensity (upper center panel), the velocity field (upper right), observed line width, σ_v (lower center), and peak temperature (lower left). The x- and y-axes of each moment map shows the angular offset from the optical center listed in Table 1. *The complete Figure Set containing 49 panel plots for all VERTICO detected galaxies is available in the online journal.*

the minor-axis PVD (lower panel) highlights the concentration of emission along the North-East edge of the gas disk. More work is needed to determine whether the source of this asymmetry is secular (e.g., spiral arms, gas streaming motions) or environment-driven (e.g., starvation, gravitational and/or ICM interaction). Channel maps for NGC4380's unmasked CO(2 − 1) cube are shown in Figure 3.

4.3. *Global CO Fluxes*

The global CO line luminosity, $L_{\rm CO}$, and integrated flux, $S_{\rm CO}$, are calculated from global spectra derived from masked data cubes. In an effort to include fainter emission at the edges of each disk in the global estimate, we adopt a 2D masking process to calculate these global properties (adapted from the 3D method used to produce the moment maps described in Section 4.1, which we refer to as the Sun et al. 2018 method). The 2D masking process for making the spectra is as follows:

1. Create a 2D mask where pixels are masked if the conditions for masking described in Section 4.1 are met at that xy position in every channel.
2. Dilate this mask in the xy plane by the rounded beam size listed in Table 2.
3. Replicate the dilated mask in every channel and apply to the primary beam corrected, continuum subtracted CO data cubes.

The full Figure Set for spectra derived from these masked cubes for every galaxy are shown after the main text of the article. The integrated CO line properties and velocity widths at zero intensity over which the line fluxes are measured are provided in Table 2. We provide measurement uncertainties on the global CO line luminosities and fluxes. True uncertainties should also include the 5 − 10% ALMA band-6 calibration accuracy and distance uncertainties, added in quadrature, that are not accounted for in the quoted values. For the latter, the determination of reliable distance for cluster galaxies is non-trivial. However, the standard deviation of VERTICO galaxy distances taken from the z0MGS database (Leroy et al. 2019) is 1.65 Mpc, which consistent with the range of Virgo size estimates ($r_{200} \approx 1.05 - 1.55$ Mpc; Boselli et al. 2018). There are four marginal detections with S/N<4 (NGC4533, NGC4698, NGC4561 and NGC4772) and two non-detections (IC3418 and VCC1581) for which we provide 3σ upper limits.

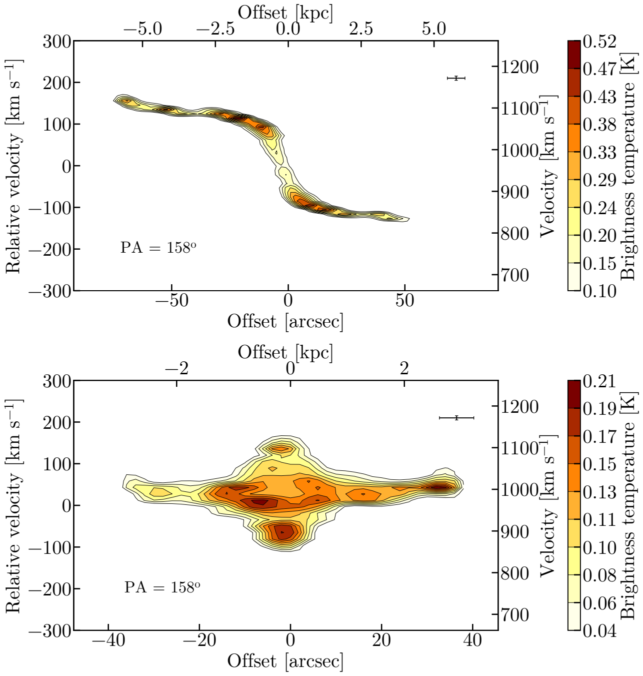

Figure 5. Position–velocity diagrams along the major (upper panel) and minor (lower panel) axes of NGC4380, extracted along the respective axes with a slit one beam in width. The bottom and top x-axes show the angular and physical offset from the galaxy center, respectively. The y-axis shows the relative offset from the systemic velocity listed in Table 1. The position angle used is 158° and the average uncertainty in each axis is illustrated in the top right corner. The channel width is 10 km s^{-1}.

Table 2. Global CO$(2-1)$ line properties for the 51 VERTICO galaxies.

Galaxy	S/N	$\theta_{\rm b}$ $''$	rms mJy	$v_{\rm lsr}$ $\rm km\,s^{-1}$	$\Delta v_{\rm line}$ $\rm km\,s^{-1}$	$S_{\rm CO}$ $\rm Jy\,km\,s^{-1}$	$\log L_{\rm CO}$ $\rm K\,km\,s^{-1}\,pc^2$	$\overline{I}_{\rm CO}$ $\rm K\,km\,s^{-1}$	$\log M_{\rm mol}$ $\rm M_\odot$
(1)	(2)	(3)	(4)	(5)	(6)	(7)	(8)	(9)	(10)
IC3392	28.3	8.4	134	1690	206	259 ± 9	7.63 ± 0.02	1.87 ± 0.07	8.37 ± 0.02
IC3418^a		8.1	101			<30.29	<6.70	<11.44	<7.44
NGC4064	23.3	9.0	32	954	225	285 ± 12	7.67 ± 0.02	2.48 ± 0.11	8.41 ± 0.02
NGC4189	38.9	7.5	202	2133	289	545 ± 14	7.95 ± 0.01	1.59 ± 0.04	8.69 ± 0.01
NGC4192	74.4	9.2	358	-143	518	1997 ± 27	8.52 ± 0.01	2.78 ± 0.04	9.26 ± 0.01
NGC4216	40.9	7.2	304	160	621	1009 ± 25	8.22 ± 0.01	1.37 ± 0.03	8.96 ± 0.01
NGC4222	12.5	8.4	26	230	255	128 ± 10	7.33 ± 0.03	0.58 ± 0.05	8.06 ± 0.03
NGC4254	185.0	8.6	331	2447	320	8369 ± 45	9.14 ± 0.00	4.64 ± 0.03	9.88 ± 0.00
NGC4293	48.8	7.6	328	936	297	810 ± 17	8.13 ± 0.01	3.80 ± 0.08	8.86 ± 0.01
NGC4294	6.4	8.2	29	376	173	62 ± 10	7.01 ± 0.07	0.37 ± 0.06	7.75 ± 0.07
NGC4298	82.7	7.5	191	1140	278	1336 ± 16	8.35 ± 0.01	2.50 ± 0.03	9.08 ± 0.01
NGC4299	5.2	8.3	117	239	112	42 ± 8	6.84 ± 0.08	0.19 ± 0.04	7.58 ± 0.08
NGC4302	67.2	7.7	313	1158	410	1375 ± 20	8.36 ± 0.01	3.39 ± 0.05	9.09 ± 0.01
NGC4321	187.9	10.2	433	1590	279	7635 ± 41	9.10 ± 0.00	3.45 ± 0.02	9.84 ± 0.00
NGC4330	16.4	7.7	32	1566	298	241 ± 15	7.60 ± 0.03	1.19 ± 0.07	8.34 ± 0.03
NGC4351	11.8	8.5	149	2324	124	79 ± 7	7.11 ± 0.04	0.37 ± 0.03	7.85 ± 0.04
NGC4380	35.3	7.5	249	990	307	432 ± 12	7.86 ± 0.01	0.90 ± 0.03	8.59 ± 0.01
NGC4383	22.9	8.1	184	1715	206	263 ± 11	7.64 ± 0.02	1.26 ± 0.05	8.37 ± 0.02
NGC4388	49.3	8.1	25	2501	486	859 ± 17	8.15 ± 0.01	2.86 ± 0.06	8.89 ± 0.01
NGC4394	12.0	8.7	24	929	215	105 ± 9	7.24 ± 0.04	0.44 ± 0.04	7.98 ± 0.04
NGC4396	10.0	7.8	217	-119	193	124 ± 12	7.32 ± 0.04	0.61 ± 0.06	8.05 ± 0.04
NGC4402	83.1	7.6	30	248	357	1402 ± 17	8.37 ± 0.01	5.00 ± 0.06	9.10 ± 0.01
NGC4405	18.3	7.7	33	1752	175	206 ± 11	7.53 ± 0.02	1.99 ± 0.11	8.27 ± 0.02
NGC4419	121.2	8.1	32	-172	447	1399 ± 12	8.37 ± 0.00	5.71 ± 0.05	9.10 ± 0.00
NGC4424	34.1	7.9	101	448	158	228 ± 7	7.58 ± 0.01	1.63 ± 0.05	8.31 ± 0.01
NGC4450	31.8	7.6	233	1960	340	523 ± 16	7.94 ± 0.01	1.14 ± 0.04	8.67 ± 0.01

Table 2 *continued*

Table 2 *(continued)*

Galaxy (1)	S/N (2)	$\theta_{\rm b}$ $''$ (3)	rms mJy (4)	$v_{\rm lsr}$ $\rm km\,s^{-1}$ (5)	$\Delta v_{\rm line}$ $\rm km\,s^{-1}$ (6)	$S_{\rm CO}$ $\rm Jy\,km\,s^{-1}$ (7)	log $L_{\rm CO}$ $\rm K\,km\,s^{-1}\,pc^2$ (8)	$\overline{I}_{\rm CO}$ $\rm K\,km\,s^{-1}$ (9)	log $M_{\rm mol}$ $\rm M_\odot$ (10)
NGC4457	63.6	7.8	238	905	297	1154 ± 18	8.28 ± 0.01	4.16 ± 0.07	9.02 ± 0.01
NGC4501	219.6	8.0	302	2277	589	5499 ± 25	8.96 ± 0.00	7.61 ± 0.03	9.69 ± 0.00
NGC4522	20.8	8.5	32	2351	217	223 ± 11	7.57 ± 0.02	1.13 ± 0.05	8.30 ± 0.02
NGC4532	18.3	7.1	151	2037	227	198 ± 11	7.52 ± 0.02	1.03 ± 0.06	8.25 ± 0.02
NGC4533	1.7	7.8	35	1698	103	10 ± 6	6.20 ± 0.26	0.04 ± 0.03	6.94 ± 0.26
NGC4535	85.4	8.2	680	1978	270	2862 ± 34	8.68 ± 0.01	2.27 ± 0.03	9.41 ± 0.01
NGC4536	88.4	8.6	452	1817	389	2465 ± 28	8.61 ± 0.01	1.90 ± 0.02	9.35 ± 0.01
NGC4548	58.7	7.6	354	509	336	1085 ± 18	8.26 ± 0.01	1.01 ± 0.02	8.99 ± 0.01
NGC4561	2.3	7.9	253	1433	92	23 ± 10	6.58 ± 0.19	0.14 ± 0.06	7.31 ± 0.19
NGC4567	91.7	7.5	21	2295	258	766 ± 8	8.10 ± 0.00	2.60 ± 0.03	8.84 ± 0.00
NGC4568	232.6	8.6	168	2279	382	2865 ± 12	8.68 ± 0.00	9.58 ± 0.04	9.41 ± 0.00
NGC4569	158.6	7.5	433	-222	492	4204 ± 27	8.85 ± 0.00	6.00 ± 0.04	9.58 ± 0.00
NGC4579	109.1	8.0	441	1517	458	2277 ± 21	8.58 ± 0.00	1.98 ± 0.02	9.31 ± 0.00
NGC4580	40.1	8.4	179	1041	215	396 ± 10	7.82 ± 0.01	2.13 ± 0.05	8.55 ± 0.01
NGC4606	25.0	7.6	21	1653	165	154 ± 6	7.41 ± 0.02	0.84 ± 0.03	8.14 ± 0.02
NGC4607	33.9	7.5	26	2283	299	420 ± 12	7.84 ± 0.01	2.11 ± 0.06	8.58 ± 0.01
NGC4651	51.0	7.9	165	805	368	640 ± 13	8.03 ± 0.01	1.94 ± 0.04	8.76 ± 0.01
NGC4654	90.3	7.5	468	1042	377	2348 ± 26	8.59 ± 0.00	2.54 ± 0.03	9.33 ± 0.00
NGC4689	62.2	7.6	293	1645	239	1175 ± 19	8.29 ± 0.01	1.65 ± 0.03	9.02 ± 0.01
NGC4694	20.8	7.1	105	1234	278	188 ± 9	7.49 ± 0.02	1.05 ± 0.05	8.23 ± 0.02
NGC4698	4.6	8.1	253	1023	451	97 ± 21	7.21 ± 0.10	0.29 ± 0.06	7.94 ± 0.10
NGC4713	23.2	8.4	184	652	204	265 ± 11	7.64 ± 0.02	0.80 ± 0.03	8.38 ± 0.02
NGC4772	1.6	7.5	31	1055	410	28 ± 17	6.66 ± 0.27	0.19 ± 0.11	7.40 ± 0.27
NGC4808	44.9	8.2	91	779	307	607 ± 14	8.00 ± 0.01	1.80 ± 0.04	8.74 ± 0.01
VCC1581[a]		8.7	25			<7.55	<6.11	<3.25	<6.84

Table 2 *continued*

Table 2 *(continued)*

Galaxy	S/N	θ_b	rms	v_lsr	Δv_line	S_CO	log L_CO	$\overline{I}_\mathrm{CO}$	log M_mol
		$''$	mJy	$\mathrm{km\,s^{-1}}$	$\mathrm{km\,s^{-1}}$	$\mathrm{Jy\,km\,s^{-1}}$	$\mathrm{K\,km\,s^{-1}\,pc^2}$	$\mathrm{K\,km\,s^{-1}}$	$\mathrm{M_\odot}$
(1)	(2)	(3)	(4)	(5)	(6)	(7)	(8)	(9)	(10)

NOTE—Columns are (1) galaxy identifier; (2) signal-to-noise of the integrated spectrum; (3) diameter of the circularized synthesized beam; (4) integrated spectrum rms in 10.6 km $\mathrm{s^{-1}}$ channels; (5) local standard of rest recession velocity of the line center, calculated as the midpoint of Δv_line; (6) velocity width of the line at zero intensity; (7) velocity integrated flux; (8) CO line luminosity given by Equation 5; (9) mean velocity integrated CO intensity; (10) logarithm of molecular gas mass given by Equation 7. This table is published in its entirety in machine-readable format. We do not include the typical band-6 calibration uncertainty of 5 – 10% (0.02 – 0.04 dex) in the flux measurement uncertainties. One may add this in quadrature to account for this.

[a] Values are 3σ upper limits calculated over an on-sky circle with radius=30$''$ (projected radius $\approx$ 2.4 kpc) and a line width of 100 km $\mathrm{s^{-1}}$. The positions and systemic velocities used are listed in Table 1

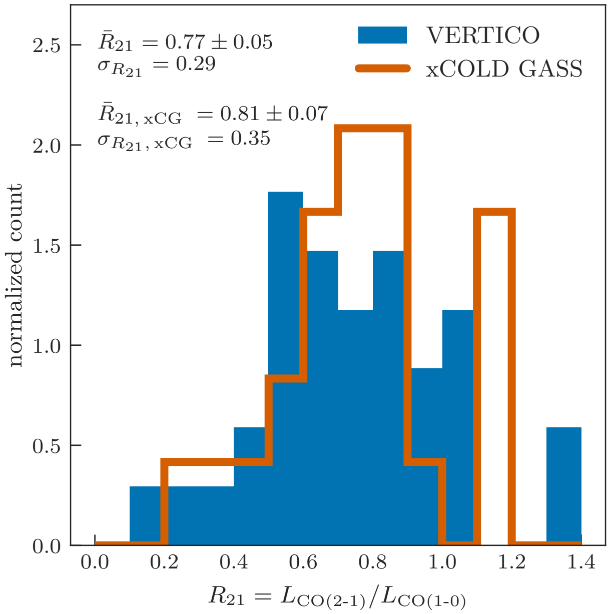

Figure 6. Normalised distribution of CO$(2-1)$/CO$(1-0)$ global line ratios for the 35 VERTICO galaxies (blue solid histogram) that have CO$(1-0)$ data presented in Boselli et al. (2014, table 11). The orange step histogram shows the 25 galaxies in xCOLD GASS with high-quality aperture-corrected IRAM 30-m CO$(1-0)$ and APEX CO$(2-1)$ data. The mean and standard deviation of each distribution are provided in the upper left corner.

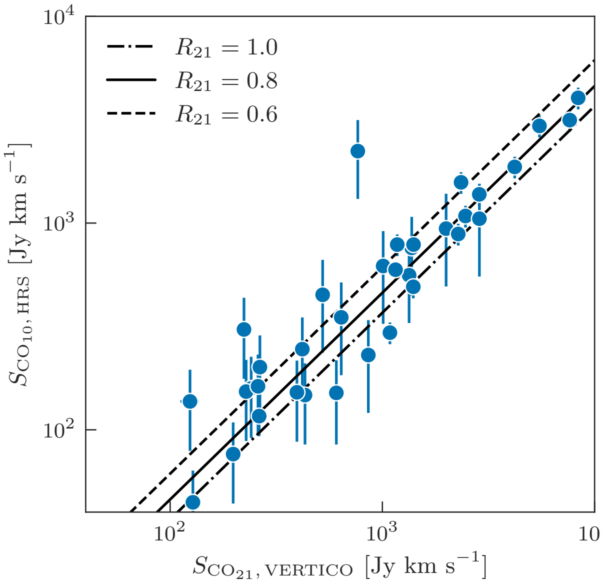

Figure 7. Correlation between observed CO$(1-0)$ and CO$(2-1)$ line flux for the 35 VERTICO galaxies that have high-quality CO$(1-0)$ data presented in Boselli et al. (2014, table 11;). The dashed, solid, and dot-dashed lines represent $R_{21} = 0.6$, 0.8, and 1 respectively. For VERTICO, the average R_{21} is 0.77 ± 0.05 while the median uncertainty on the CO$(2-1)$ line flux is 16 Jy km s^{-1} and thus within the marker size on the $x-$axis scale.

Following Solomon & Vanden Bout (2005), we calculate the CO line luminosity, L_{CO} in K km s^{-1} pc^2, expressed as the product of the velocity integrated source brightness temperature and the source area

$$L_{\mathrm{CO}} = 3.25 \times 10^7\, S_{\mathrm{CO}}\, \nu_{\mathrm{obs}}^{-2}\, D_L^2\,, \tag{5}$$

where S_{CO} is the velocity integrated flux in Jy km s^{-1}, ν_{obs} is the observed frequency in GHz, and D_L is the luminosity distance to the source in Mpc. For clarity, L_{CO} is L'_{CO} in equation 3 of Solomon & Vanden Bout (2005).

Figures 6 and 7 compare the CO$(1-0)$ and CO$(2-1)$ line luminosity ratio (R_{21}) and integrated flux densities for the 35 VERTICO galaxies that have CO$(1-0)$ data compiled and presented by Boselli et al. (2014, blue solid histogram) for the HRS. Establishing R_{21} across the sample is important for deriving molecular gas masses (e.g., Equation 7) and interpreting our results in the context of other studies. For this comparison, Boselli et al. (2014) fluxes are converted from T_R^* (observed antenna temperature corrected for atmospheric attenuation, radiative loss, and forward and rearward scattering and spillover efficiency) to T_A^* (observed antenna temperature corrected for atmospheric attenuation, radiative loss, and rearward scattering and spillover efficiency) temperature scales via the expression

$$T_A^* = \eta_{fss}\, T_R^*\,, \tag{6}$$

where η_{fss} is the forward scattering and spillover efficiency of the telescope (Kutner & Ulich 1981). Following Boselli et al. (2014), we adopt $\eta_{fss} = 0.68$ for the National Radio Astronomy Observatory Kitt Peak 12-m telescope.

Figure 6 shows the distribution of observed $R_{21} =$ CO$(2-1)$/CO$(1-0)$ line luminosity ratios for the VERTICO-HRS sample (blue histogram). We also show the observed R_{21} ratio for the 25 xCOLD GASS galaxies with APEX CO$(2-1)$ and high-quality IRAM-30m CO$(1-0)$ detections as presented in Saintonge et al. (2017, WCO_FLAG and FLAG_APEX = 1 in their catalog). We measure $\bar{R}_{21} = 0.77 \pm 0.05$ in VERTICO galaxies with a standard deviation of $\sigma = 0.3$, in agreement with the value of $\bar{R}_{21} = 0.79 \pm 0.03$ reported by Saintonge et al. (2017) and measured from their published data release, $\bar{R}_{21} = 0.81 \pm 0.07$, where their assumed metallicity-dependent $\alpha_{\mathrm{CO}} > 1$ M$_\odot$ pc^{-2} (K km s^{-1})$^{-1}$. The minor difference between the reported and measured xCOLD GASS R_{21} values is due to the exclusion of galaxies based on the quality of the APEX data in the published value (Saintonge, private communication). Based on our measured value and its agreement with the literature, we adopt a constant value of $R_{21} = 0.8$ throughout this work. We note that this is comparable to but slightly higher than reported values in other works (Leroy et al. 2013; den Brok et al. 2021; Yajima et al. 2021). Further characterization of R_{21} and its variation across the VERTICO sample will be the subject of future work.

Figure 7 plots the relation between the CO$(1-0)$ and CO$(2-1)$ integrated flux densities for the 35 VERTICO-HRS galaxies. For illustration, $R_{21} = 1$, 0.8, and 0.5, are denoted by the dot-dashed, solid, and dashed lines respectively. The outlier with the lowest R_{21} (above the main correlation) is NGC4567 which is in very close proximity to NGC4568. The original CO$(1-0)$ data for this galaxy are drawn from Five College Radio Astronomy Observatory observations ($45''$ beam size) published by Chung et al. (2009b). Determining whether physical or observational effects (e.g., source confusion) are responsible for NGC4567's low R_{21} value is beyond the scope of this paper.

4.4. *Global Molecular Gas Masses*

We convert CO luminosity to molecular gas mass, including the contribution from heavy elements, in units of solar mass using the relation

$$M_{\rm mol} = \frac{\alpha_{\rm CO}}{R_{21}} L_{\rm CO}\,, \tag{7}$$

where $\alpha_{\rm CO} = 4.35\ {\rm M_\odot\ pc^{-2}\ (K\ km\ s^{-1})^{-1}}$, the molecular gas mass-to-CO$(1-0)$ luminosity ratio calculated for the Milky Way disk by Bolatto et al. (2013), and $\mathrm{R}_{21} = 0.8$. Our $\alpha_{\rm CO}$ corresponds to a CO$(1-0)$-to-H$_2$ conversion factor of $X_{\rm CO} = 2\times10^{20}\ {\rm cm^{-2}\ (K\ km\ s^{-1})^{-1}}$ that is consistent with other surveys of CO emission in nearby galaxies (e.g., HERACLES – Leroy et al. 2009; JCMT-NGLS – Wilson et al. 2009; xCOLD GASS – Saintonge et al. 2011, 2017; EDGE-CALIFA – Bolatto et al. 2017).

All molecular gas masses quoted in this paper include the 36% contribution of helium (Kennicutt & Evans 2012; Bolatto et al. 2013). The true value of $\alpha_{\rm CO}$ can be up to a factor 5 lower in regions of increased average gas volume density such as in mergers and galaxy centers as has been shown in observations (e.g., Leroy et al. 2011; Smith et al. 2012; Sandstrom et al. 2013) and demonstrated with modeling (e.g., Shetty et al. 2011; Narayanan et al. 2011, 2012; Olsen et al. 2016). We leave a more detailed modeling and application of $\alpha_{\rm CO}$ to future work.

Figure 8 compares the stellar mass, sSFR, and molecular gas mass properties of VERTICO galaxies (blue) with the volume-limited xCOLD GASS sample (orange; Saintonge et al. 2011, 2017)[8]. As with xGASS, we apply the recommended weights published by Saintonge et al. (2017) to the xCOLD GASS data to achieve a volume-limited sample for $M_\star \geq 10^9\ {\rm M_\odot}$. We adjust the published xCOLD GASS molecular gas estimates to our assumed $\alpha_{\rm CO}$ in Equation 7. The upper left panel compares the distribution of xCOLD GASS and VERTICO in the stellar mass–sSFR plane, again highlighting VERTICO's selection of star-forming and quenching galaxies, rather than quiescent galaxies (*cf.* Figure 1). The left and right panels in the middle row show molecular gas fraction ($M_{\rm mol}/M_\star$) as a function of stellar mass and sSFR, respectively. While there are a small number of VERTICO galaxies with low molecular gas fractions, the majority of the sample is either normal or rich in molecular gas at fixed stellar mass and sSFR. The lower panels show the volume-limited stellar mass, sSFR, and molecular gas mass distributions. Interestingly, there is a significant fraction of xCOLD GASS galaxies that are more star-forming than VERTICO, however, this does not translate into an excess in the molecular gas mass distribution. Although more investigation is needed, this may at least be partially explained by the increased fraction of massive VERTICO galaxies in comparison to the xCOLD GASS sample (lower left panel).

4.5. *CO Radial Profiles*

We measure azimuthally averaged CO intensity radial profiles in elliptical annuli overlaid on the integrated intensity maps described in Section 4.1. Annuli are centered on the optical position and aligned with the major-axis position angle. Eccentricity is derived from the optical inclination of the galaxy provided in Table 1. To ensure the independence of each measurement, the annulus width along the minor axis is set to the synthesized beam size. The corresponding radii are defined as the mean galacto-centric radius of pixels in each annuli. The average intensity is calculated as the summed emission divided by the total area. This means that non-detections (i.e., masked pixels) within each annulus are included in this calculation as zero intensity. This approach is conservative, especially where galaxies have asymmetric or fragmented gas disks, and results in radial profiles that can be considered lower limits on the true average CO surface brightness, particularly in the outskirts. Future work will explore the impact of this method on the measured radial profiles and iso-density radii.

---

[8] http://www.star.ucl.ac.uk/xCOLDGASS/

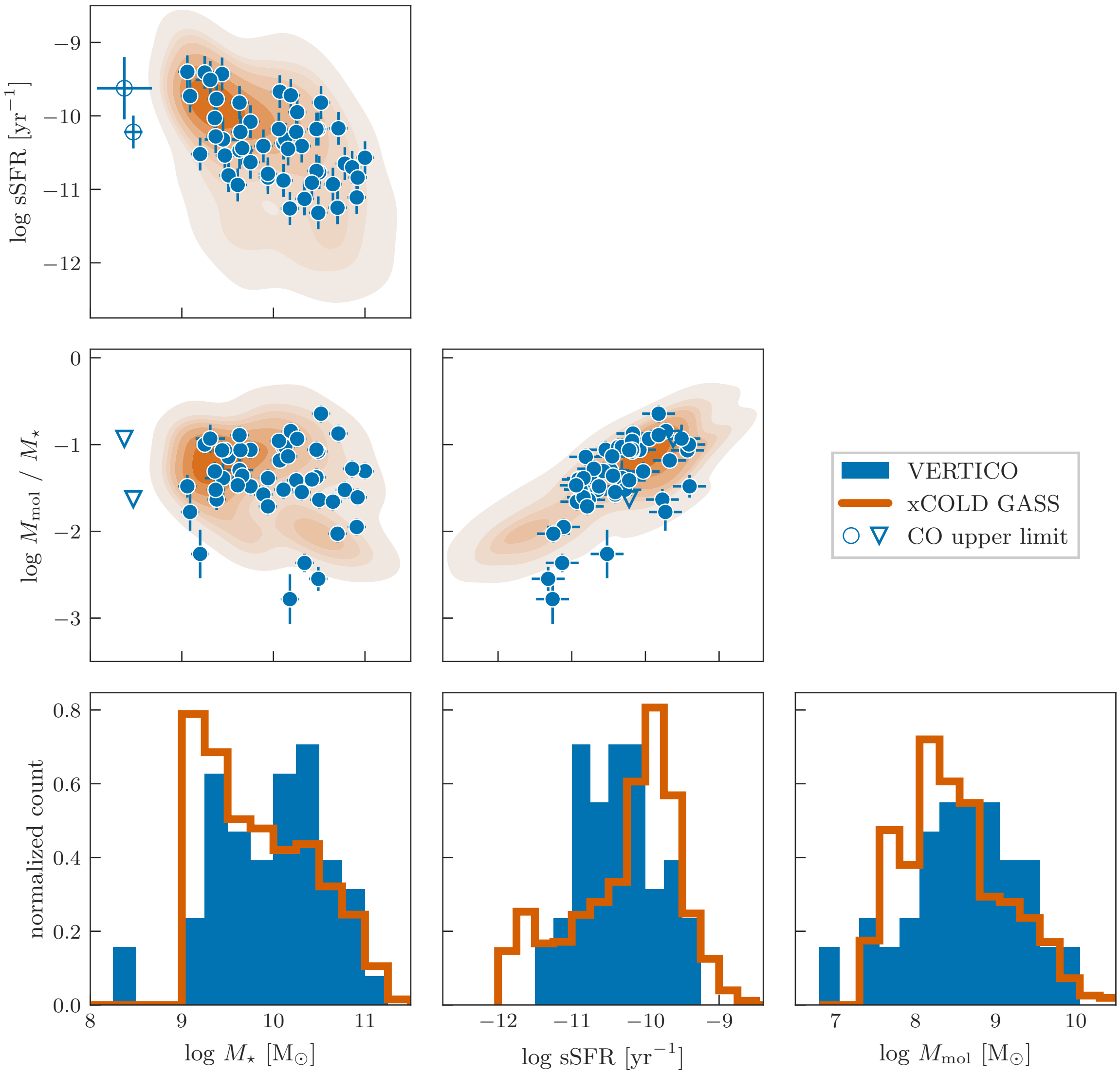

Figure 8. Global properties of the VERTICO sample (blue points and histograms) compared to the weighted xCOLD GASS catalog published by Saintonge et al. (2017, orange distributions). We include the 528 xCOLD GASS galaxies that have their recommended ('best') SFR estimate. We adjust all molecular gas estimates to our constant conversion factor and the 199 CO non-detections in xCOLD GASS are included as 3σ upper limits. Left to right starting at the upper left; sSFR vs. stellar mass, molecular gas fraction vs. stellar mass, molecular gas fraction vs. sSFR, the normalized stellar mass, sSFR, and molecular gas mass distributions. The three histogram panels share the same y-axis range. The two galaxies that are undetected in CO are shown with open markers and inverted triangles denote their upper limits.

For highly inclined galaxies this method does not work well as the axial ratio becomes too small causing highly eccentric annuli with the major axes extending beyond the galactic disk. Therefore, for galaxies with inclination $\geq 80^\circ$, we use a slice that is one beam thick aligned with the major axis. The integrated intensity as a function of radius is then calculated by averaging the emission in each slice.

Uncertainties on all the intensity profiles are calculated as,

$$u_{\rm rp} = \sigma(I_{\rm CO,\,pix})\,\sqrt{N_{\rm beam}}, \tag{8}$$

where $\sigma(I_{\rm CO,\,pix})$ is the standard deviation of integrated intensity in each pixel and $N_{\rm beam}$ is the number of beams within each annulus.

Figure 9 shows the mean surface brightness radial profiles of 49 VERTICO galaxies (IC3418 and VCC1581 are non-detections). The profiles are denoted by gray points and their uncertainties are shown by the gray shaded regions. Radial profiles in surface brightness units are not corrected for inclination.

Although quantitative analyses of the molecular gas distribution in VERTICO galaxies will be the subject of

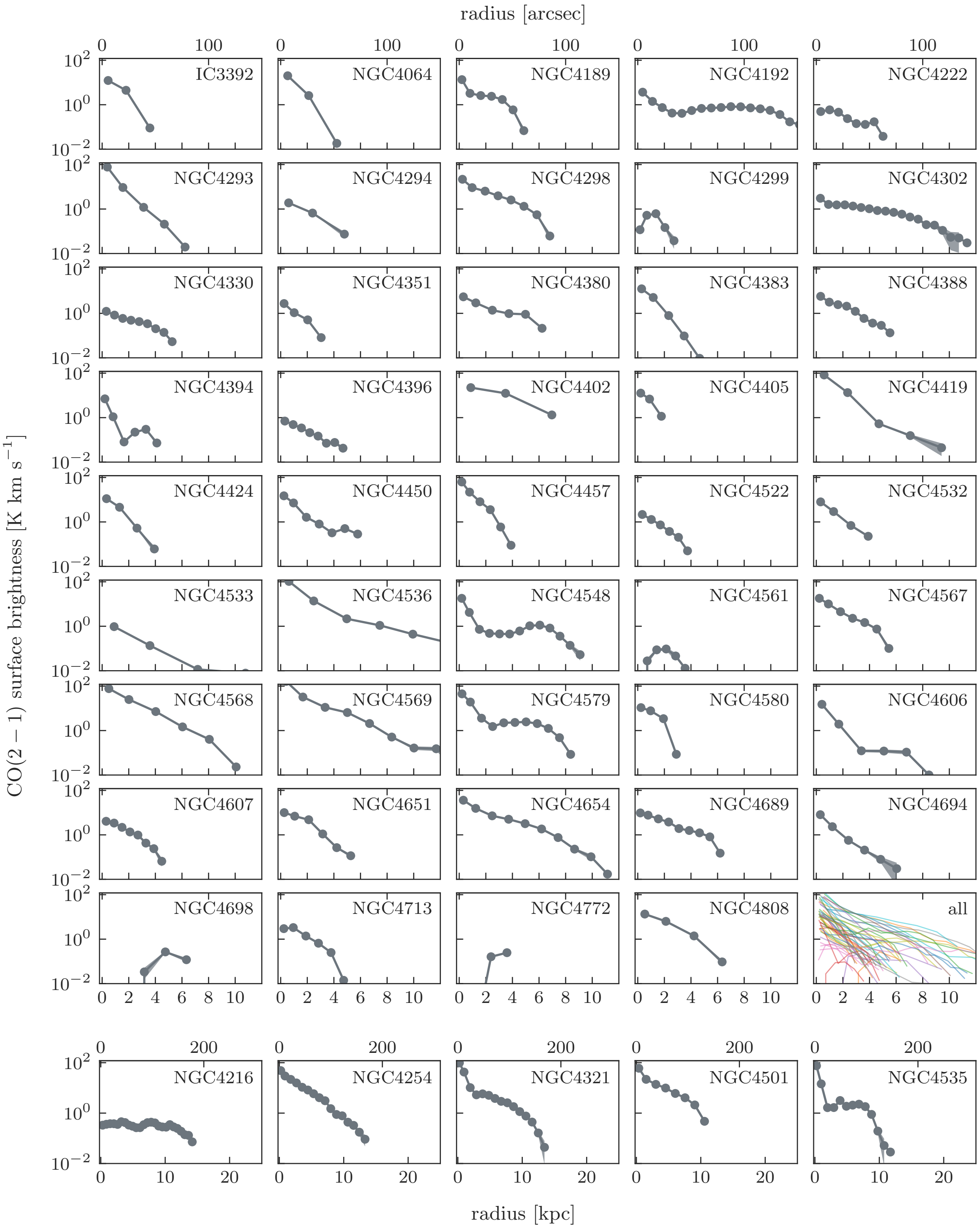

Figure 9. Azimuthally averaged surface brightness profiles as a function of galactocentric radius in kpc (bottom x-axis) and arcseconds (top). Radial profiles are denoted by the grey points while their uncertainties are illustrated by the shaded region. The five largest galaxies are shown in the last row with a different x-axis range. We show all the profiles in the last panel of the ninth row, highlighting the diversity of profile shapes. The surface brightness radial profiles are not corrected for inclination. Table 3 contains the 50% and 90% flux radii ($r_{50,\,\mathrm{mol}}$ and $r_{90,\,\mathrm{mol}}$, respectively) and inclination-corrected iso-density radii ($r_{5,\,\mathrm{mol}}$) for each galaxy, where possible.

upcoming work, here we comment briefly on the large range of gas disk morphologies exhibited by the CO surface brightness profiles. A significant number of profiles do not decrease steadily as a function of radius, showing bumps in the CO distribution at larger radii (e.g., NGC4189, NGC4450, NGC4535, NGC4548, NGC4579, NGC4808) or, perhaps most interestingly, signs of truncation at the outer edge of the disk (e.g., NGC4064, NGC4299, NGC4402, NGC4457, NGC4532, NGC4535, NGC4580, NGC4607). This variation contrasts with the findings from studies of nearby field galaxies where the CO radial profiles are typically exponential with a comparable scale length as the stellar disk (Regan et al. 2001; Helfer et al. 2003; Leroy et al. 2009; Schruba et al. 2011; Bigiel & Blitz 2012; Leroy et al. 2013; Bolatto et al. 2017) but is qualitatively closer to the observed surface brightness profiles of early-type galaxies, which do often show such enhancements and truncation (e.g., Davis et al. 2013). Given the observed diversity in the VERTICO galaxies' stellar morphologies and the efficacy of CO as a dynamical tracer, the variety of shapes seen in the inner regions of VERTICO radial profiles could be driven by stellar bars or other dynamical features such as bulges or arms. Chown et al. (2019) clearly show that barred spiral galaxies exhibit a large range of molecular gas radial profile shapes, molecular gas concentrations, and star formation histories in their inner regions. Furthermore, those authors find that the level of central star formation enhancement is correlated with gas concentration in barred galaxies. Related works show similar diversity in central molecular gas concentration (e.g., Sheth et al. 2005), star formation properties (e.g., Lin et al. 2017, 2020), and HI surface density (e.g., Wang et al. 2014). It is clear that the combination of gas morphology with the high angular resolution and sensitivity of these observations results in profiles that frequently depart from smoothly decreasing decline. We also note that we do not see a central hole in the CO surface brightness distribution for many galaxies, as is commonly found in other surveys (e.g., Bigiel & Blitz 2012). In contrast, the observed CO surface brightness distribution of VERTICO galaxies is closer to the typical shapes of Hα emission in Virgo Cluster galaxies found by Koopmann et al. (2001). In this work, the Hα disks – as a close tracer of star formation – exhibit a similar range concentration and morphology to the CO, including systems that show elevated emission in the circumnuclear regions and truncation of star formation in the outer optical disk. A large range in concentration is also reported by studies of UV disk morphology in nearby galaxies (e.g., Muñoz-Mateos et al. 2009). Improved characterization and modeling of the CO radial profiles is required to understand the observed trends and differences between VERTICO and field galaxy samples.

Table 3. Molecular gas disk radii estimates.

Galaxy	$r_{50,\,\mathrm{mol}}$ kpc	$r_{90,\,\mathrm{mol}}$ kpc	$r_{5,\,\mathrm{mol}}$ kpc
IC3392	1.16	2.32	2.41
NGC4064	1.06	2.18	2.08
NGC4189	1.27	3.23	3.57
NGC4192	5.10	9.70	
NGC4216	6.51	11.58	
NGC4222	1.55	4.01	
NGC4254	1.94	5.72	8.33
NGC4293	0.79	1.86	2.60
NGC4294	1.55	3.20	
NGC4298	1.45	3.94	4.69
NGC4299	1.15	1.85	
NGC4302	2.86	6.74	
NGC4321	1.03	5.95	9.74
NGC4330	1.65	3.76	
NGC4351	0.88	2.12	0.80
NGC4380	1.63	4.77	1.95
NGC4383	0.84	1.84	1.94
NGC4388	1.46	3.30	0.42
NGC4394	0.50	2.85	0.82
NGC4396	1.30	3.18	
NGC4402	2.69	5.21	5.63
NGC4405	0.69	1.35	1.74
NGC4419	1.24	2.70	3.69
NGC4424	0.92	1.94	1.97
NGC4450	0.85	2.78	2.04
NGC4457	0.65	1.84	2.87
NGC4501	2.20	6.54	8.97
NGC4522	1.08	2.46	
NGC4532	0.95	2.30	1.65
NGC4533	1.90	4.58	
NGC4535	0.74	6.39	8.29
NGC4536	1.33	3.62	4.31
NGC4548	0.78	6.31	1.29
NGC4561	1.91	2.87	
NGC4567	1.06	3.16	3.71
NGC4568	1.47	3.84	5.31
NGC4569	1.12	4.12	6.42

Table 3 *continued*

Table 3 *(continued)*

Galaxy	$r_{50,\,\mathrm{mol}}$	$r_{90,\,\mathrm{mol}}$	$r_{5,\,\mathrm{mol}}$
	kpc	kpc	kpc
NGC4579	0.85	5.15	6.75
NGC4580	0.98	2.01	2.50
NGC4606	0.87	2.13	1.53
NGC4607	1.19	2.75	
NGC4651	1.30	2.67	2.96
NGC4654	1.52	4.97	6.15
NGC4689	1.47	4.10	4.76
NGC4694	0.85	2.41	1.38
NGC4698	4.91	5.94	
NGC4713	1.17	2.72	1.98
NGC4772	2.84	3.45	
NGC4808	1.65	3.59	3.32

Note—Columns are (1) galaxy identifier; (2) radius containing 50% of the global CO$(2-1)$ flux; (3) radius containing 90% of the global CO$(2-1)$ flux; (4) inclination-corrected molecular gas iso-density radius at $\Sigma_{\mathrm{mol}}(r) = 5\ \mathrm{M_\odot\ pc^{-2}}$; At the distance of Virgo $1'' = 80$ pc. This table is published in its entirety in machine-readable format.

5. THE MOLECULAR GAS SIZE–MASS RELATION

The richness and quality of the VERTICO data enables many research avenues. As an initial demonstration of the survey's scientific power, we now focus on establishing the relationship between the size and mass of molecular gas disks in the VERTICO sample, and consider the effect of environment on this relation. The size–mass relation has been explored in detail for stellar and H I distributions in both theory and observation (e.g., Wang et al. 2016; Stevens et al. 2019; Trujillo et al. 2020; Sánchez Almeida 2020, and references therein). Stevens et al. (2019) and Sánchez Almeida (2020) respectively demonstrate for H I and stellar content that the tight correlation between galaxy radius—defined at a fixed surface density—and global mass is mathematically inevitable, given the limited range of physically plausible surface density profile shapes these components can have (e.g., saturated exponentials for H I, Sérsic stellar profiles). Indeed, Stevens et al. (2019) find that only a drastic change in H I disk morphology is able to cause significant deviation from the H I size–mass relation. Hereafter, the term 'size–mass relation' refers to the molecular gas size–mass relation unless explicitly stated otherwise.

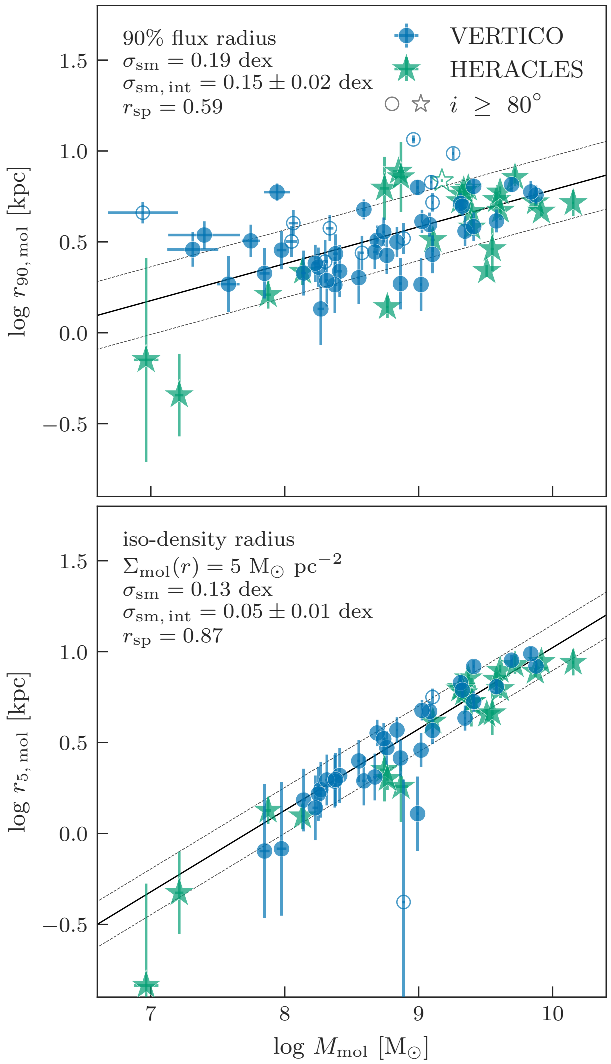

Figure 10. The molecular gas size–mass relation for 90% flux radii ($r_{90,\,\mathrm{mol}}$, upper panel) and inclination-corrected iso-density radii ($r_{5,\,\mathrm{mol}}$, lower panel). The former enclose 90% of the molecular gas flux (and thus mass for a fixed α_{CO}), while the latter are defined as the radius where $\Sigma_{\mathrm{mol}}(r) = 5\ \mathrm{M_\odot\ pc^{-2}}$. Galaxies from the VERTICO and HERACLES surveys are denoted by blue and green points, respectively. The rms scatter (σ_{sm}), intrinsic scatter accounting for errors ($\sigma_{\mathrm{sm,\,int}}$), and Spearman rank coefficient (r_{sp}) for the combined VERTICO-HERACLES relation are given in the upper left of each panel. The best-fitting relation for all galaxies is shown by the black solid line with $\pm 1\sigma_{\mathrm{sm}}$ denoted by the black dashed lines (see text for fit parameters). Galaxies with inclination $\geq 80°$ are denoted by open markers and not included in the fits to the data.

We use galaxies from the Heterodyne Receiver Array CO Line Extragalactic Survey (HERACLES; Leroy et al. 2009) as a convenient nearby field control sample ($2 < D\,/\,\mathrm{Mpc} < 25$), which spans a comparable range in galaxy stellar mass and sSFR ($10^{8.5} < \mathrm{M_\star}\,/\,\mathrm{M_\odot} < 10^{11}$

and $10^{-11.5} < \mathrm{sSFR}\,/\,\mathrm{yr}^{-1} < 10^{-9.2}$, respectively). As with VERTICO, the stellar mass and star formation rate estimates are drawn from the z0MGS database (Leroy et al. 2019). There are 48 HERACLES galaxies with public CO$(2-1)$ data cubes that have an angular resolution of 13″ in 5 km s^{-1} wide channels[9]. Excluding 18 non-detections and five galaxies that overlap with the VERTICO sample (NGC4579, NGC4569, NGC4536, NGC4321, NGC4254) leaves 25 galaxies for this comparison. Starting from the public cubes at their native 13″ angular resolution and 10 km s^{-1} channel width, we apply the same methodology used for the VERTICO data and described in Sections 4.3 and 4.4 to derive the molecular gas masses. The VERTICO masses and radii used in this section are presented in Table 2 and Table 3, respectively.

Figure 10 shows the combined VERTICO and HERACLES molecular gas size–mass relation for two measurements of galaxy size as measured from the radial profiles. The first, shown in the right panel, is the radius enclosing 90% of the CO flux, $r_{90,\,\mathrm{mol}}$. From here on, we use the term 'flux-percentage radius' to refer generally to radii calculated at a given percentage of flux. Since, in this work, we simply scale the CO emission by α_{CO} to get molecular gas surface density, this 90%-light radius is also the 90%-mass radius. The second is the iso-density radius, $r_{5,\,\mathrm{mol}}$ shown in the lower panel, defined at fixed molecular gas surface density, $\Sigma_{\mathrm{mol}}(r) = 5\ \mathrm{M}_\odot\ \mathrm{pc}^{-2}$, and calculated from the inclination-corrected surface density radial profiles. The uncertainties shown are the observation beam size listed in Table 2, converted into physical units. For highly inclined galaxies ($i \geq 80°$), we assume an inclination of 80° when calculating the inclination correction and exclude these from the fits described below. Unlike the flux-percentage radii, estimates of iso-density radii are not possible for every galaxy so only the 62 galaxies (38 VERTICO, 24 HERACLES) where surface density profiles reach $\Sigma_{\mathrm{mol}}(r) = 5\ \mathrm{M}_\odot\ \mathrm{pc}^{-2}$ are shown in the lower panel. The severity of the inclination correction for the highly inclined galaxies ($cos(80°) = 0.17$) means an $r_{5,\,\mathrm{mol}}$ measurement is not available.

Throughout this analysis, VERTICO and HERACLES galaxies are denoted by blue circles and green stars, respectively. We use the LtsFit Python package to fit each relation. The method, described in detail by Cappellari et al. (2013, Section 3.2), accounts for measurement uncertainties to determine the best-fit parameters and scatter. We turn off outlier detection for this work. Using this approach, we derive the best fit to the 90% flux-percentage radius size–mass relation (black solid lines) as,

$$\log\left(\frac{r_{90,\,\mathrm{mol}}}{\mathrm{kpc}}\right) = 0.54 + 0.20\left[\log\left(\frac{\mathrm{M_{mol}}}{\mathrm{M}_\odot}\right) - 8.83\right]. \tag{9}$$

Similarly, we fit the following relationship to the iso-density size–mass relation,

$$\log\left(\frac{r_{5,\,\mathrm{mol}}}{\mathrm{kpc}}\right) = 0.54 + 0.45\left[\log\left(\frac{\mathrm{M_{mol}}}{\mathrm{M}_\odot}\right) - 8.94\right]. \tag{10}$$

Uncertainties on the fit parameters are provided in Table 4. The rms scatter, σ_{sm}, intrinsic scatter accounting for errors, $\sigma_{\mathrm{sm,\,int}}$, and Spearman rank coefficent, r_{sp}, are printed in the upper left of each panel. The former is denoted by the black dashed lines.

We find that the flux-percentage size–mass relation has significantly larger rms and intrinsic scatter ($\sigma_{\mathrm{sm}} = 0.19$ dex and $\sigma_{\mathrm{sm,\,int}} = 0.16 \pm 0.02$ dex) than the iso-density size–mass relation ($\sigma_{\mathrm{sm}} = 0.13$ dex and $\sigma_{\mathrm{sm,\,int}} = 0.05 \pm 0.01$ dex). This result agrees both qualitatively and quantitatively with studies of stellar and H I disks that find iso-density radii reduce the scatter to $\lesssim 0.1$ dex in the respective size–mass relations compared with flux-percentage radii (Saintonge & Spekkens 2011; Cortese et al. 2012; Wang et al. 2016; Stevens et al. 2019; Trujillo et al. 2020; Sánchez Almeida 2020). The larger Spearman rank coefficent ($r_{sp} = 0.87$) highlights the stronger statistical connection between global molecular gas mass and iso-density radii rather than flux-percentage radii ($r_{sp} = 0.59$).

Figure 11 shows the comparison between these two size estimates for VERTICO and HERACLES galaxies. At fixed $r_{5,\,\mathrm{mol}}$, both VERTICO and HERACLES galaxies exhibit large range in $r_{90,\,\mathrm{mol}}$, and, while most galaxies tend to have consistently larger $r_{5,\,\mathrm{mol}}$ than $r_{90,\,\mathrm{mol}}$, this not the case for approximately 25% of the combined sample. The scatter in $r_{90,\,\mathrm{mol}}$ at fixed $r_{5,\,\mathrm{mol}}$ reflects the different degrees of concentration in CO disks across both samples.

We check the consistency of the size–mass relations between the VERTICO and HERACLES samples and, although we do not plot the fits, provide the best-fit parameters in Table 4. Where only the HERACLES sample is fit, we include the galaxies that overlap with VERTICO with their radii and masses measured from the public HERACLES data. This comparison demonstrates that the flux-percentage size–mass relation varies considerably between the VERTICO and HERACLES samples. On the other hand, the slope and scatter of the

---

[9] https://www.iram-institute.org/EN/content-page-242-7-158-240-242-0.html

Table 4. Molecular gas size–mass relation best fit parameters for the VERTICO, HERACLES, and combined samples.

Sample	y	a	b	pivot	$\sigma_{\rm sm}$	$\sigma_{\rm sm,\,int}$	N
Combined	$\log\left(\frac{r_{90,\,\rm mol}}{\rm kpc}\right)$	0.54±0.02	0.20±0.03	8.83	0.19	0.16±0.02	62
VERTICO		0.54±0.02	0.15±0.04	8.66	0.16	0.12±0.03	38
HERACLES		0.61±0.03	0.27±0.05	9.18	0.19	0.16±0.03	29
Combined	$\log\left(\frac{r_{5,\,\rm mol}}{\rm kpc}\right)$	0.55±0.01	0.45±0.02	8.94	0.13	0.05±0.01	56
VERTICO		0.52±0.02	0.46±0.03	8.83	0.12	0.04±0.02	33
HERACLES		0.64±0.02	0.45±0.03	9.20	0.13	0.05±0.02	28

Note—Columns are (1) the sample used to fit the molecular gas size–mass relation; (2) the definition of radius used; (3) – (5) the best fit parameters for $y = a + b(x - \text{pivot})$ where x is $\log M_\star/{\rm M}_\odot$; (6) the scatter about the fit, $\sigma_{\rm sm} = \sigma(\text{fit} - \text{radius})$; (7) intrinsic scatter around the linear relation accounting for uncertainties ($\sigma_{\rm sm,\,int}$ is called ϵ_y in equation 6 of Cappellari et al. 2013); and (8) the number of galaxies used in each fit.

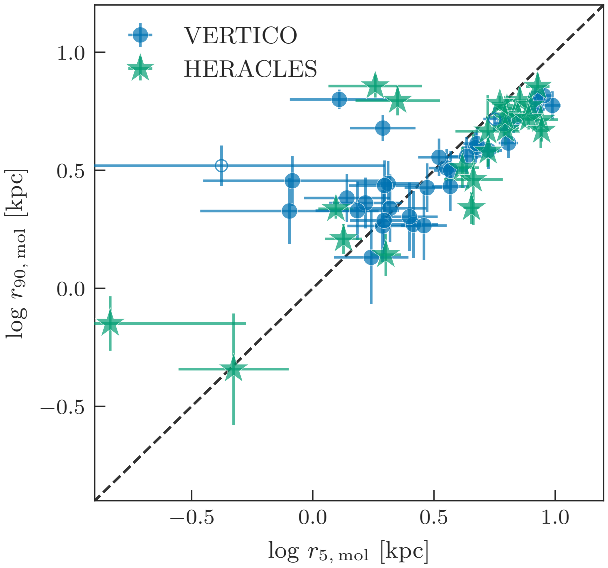

Figure 11. Iso-density radii ($r_{5,\,\rm mol}$) versus the 90% flux radii ($r_{90,\,\rm mol}$) for VERTICO (blue) and HERACLES (green) galaxies. The iso-density radii are determined at $\Sigma(r_{5,\,\rm mol}) = 5\ {\rm M}_\odot\ {\rm pc}^{-2}$ and have been corrected for inclination. Galaxies to the bottom right tend to have CO distributions that are less concentrated than those in the upper left.

iso-density size–mass relation are remarkably consistent for both VERTICO and HERACLES. Given that many of the VERTICO gas disks are clearly perturbed by environment, this suggest that the observed iso-density size–mass relation does not have an environmental dependence, a result that is consistent with the findings of the H I size–mass relation studies (Wang et al. 2016; Stevens et al. 2019). Indeed, this invariance implies that external mechanisms act to suppress or remove galaxy gas content, rather than simply rearranging the distribution of gas within the disk. If environmental processes were to alter how gas is distributed throughout the galaxy without depleting the total amount of gas within the disk, one would expect such effects to drive galaxies away from the size–mass relation (above or below) as gas mass is conserved and iso-density radius is altered. It is reasonable to expect this scenario to result in a correlation of the form and scatter of size–mass relation with environment which we do not see in the comparison between VERTICO and HERACLES. This paints a picture whereby, for VERTICO at least, any perturbation of the molecular gas distribution is also coupled with a change in total mass of the gas disk. Although we caution that a much more detailed exploration is required, the consistency and tightness in the size–mass relation defined using iso-density radii highlights the interesting possibility of using molecular gas mass as a predictor of gas disk size.

We now investigate the definitions of flux-percentage radius and iso-density radius that produce the least scatter and strongest correlation in the two size–mass relations. To this end, we repeat the analysis above for flux-percentage radii enclosing 50%, 60%, 70%, 80%, and 90% of the light, and iso-density radii in the range $\Sigma_{\rm mol}(r) = 1 - 20\ {\rm M}_\odot\ {\rm pc}^{-2}$, in increments of $1\ {\rm M}_\odot\ {\rm pc}^{-2}$. The left- and right-hand columns in Figure 12 show the resulting rms scatter ($\sigma_{\rm sm} = \sigma(\text{fit} - \text{radius})$, top row), intrinsic scatter ($\sigma_{\rm sm,\,int}$, second row), Spearman rank coefficient (third row), and slope (bottom row) of the VERTICO-HERACLES size–mass relation versus the flux percentage at which radii are defined and iso-density $\Sigma_{\rm mol}(r)$, respectively. The colors of the points in the

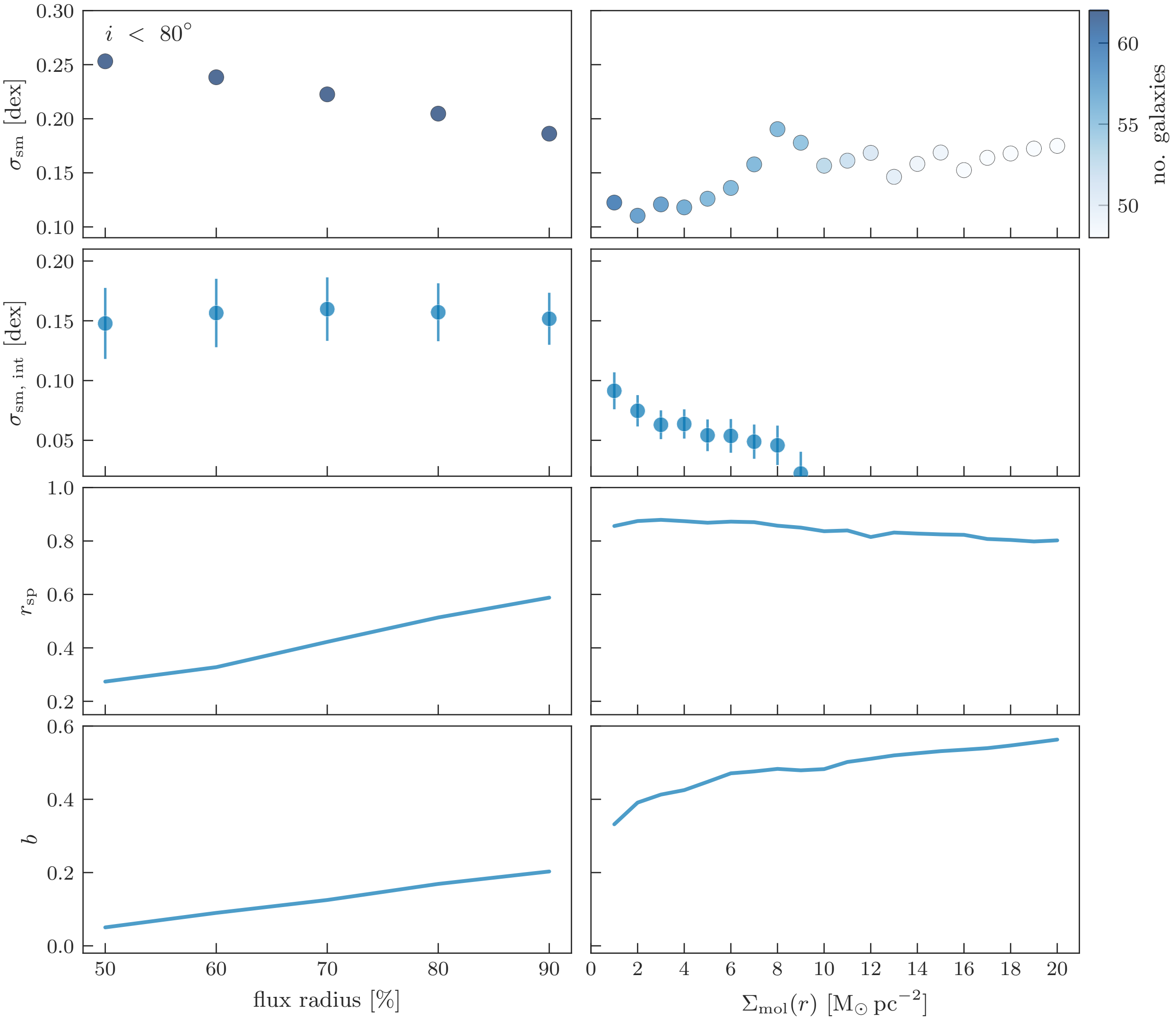

Figure 12. Scatter (top row), intrinsic scatter accounting for uncertainties (second row), Spearman rank coefficient (third row), and slope (bottom row) of the molecular gas size–mass relation as a function of flux-percentage radius percentage (left; i.e., radii are defined as enclosing a particular percentage of CO flux) and iso-density radius definition [right; i.e., radii are defined at mean molecular gas surface density, $\Sigma_{\rm mol}(r)$]. As with Figure 10, we exclude galaxies with inclinations $\geq 80^\circ$ from the fits.

upper panels denote the number of galaxies in the given size–mass relation.

The scatter in the flux-percentage radius size–mass relation decreases gradually as the percentage of flux enclosed by the radius increases. By contrast, the iso-density size–mass relation scatter increases with $\Sigma_{\rm mol}(r)$ above $\Sigma_{\rm mol}(r) \sim 10\ \rm M_\odot\ pc^{-2}$. We find the rms scatter is minimized at $\Sigma_{\rm mol}(r) \sim 5\ \rm M_\odot\ pc^{-2}$ while the intrinsic scatter is lowest in the range $\Sigma_{\rm mol}(r) \sim 5-10\ \rm M_\odot\ pc^{-2}$. Using iso-density radii results in a stronger correlation, as quantified by the Spearman rank coeffecient, than flux-percentage radii regardless of the exact definition. However, the Spearman rank coefficient of the flux-percentage radius size–mass relation increases with the percentage of enclosed flux. We also see a slight decrease in the correlation strength for iso-densities of $\Sigma_{\rm mol}(r) \gtrsim 10\ \rm M_\odot\ pc^{-2}$. The flux-percentage radius size–mass relation steadily steepens as the enclosed percentage of flux increases and, while the iso-density relation is always steeper, there is some variation its slope as a function of $\Sigma_{\rm mol}(r)$. The radius definitions where scatter and Spearman rank coefficient are minimized and maximized, respectively, motivate the choices of $r_{90,\,\rm mol}$ and $\Sigma_{\rm mol}(r) \sim 5\ \rm M_\odot\ pc^{-2}$ used in Figures 10 and 11.

Following the logic outlined in Stevens et al. (2019) and Sánchez Almeida (2020), it is expected that the iso-density size–mass relation should be consistently tighter than the flux-percentage radius relation because, broadly speaking, the surface density profiles decrease with radius. This means that for any two gas disks with the same total mass, their radial surface density profiles must intersect at a particular radius. Choosing a $\Sigma_{\rm mol}(r)$ that is close to the surface density at this crossing radius necessarily reduces the scatter.

The natural next step is to consider why the scatter in the molecular gas iso-density relation falls to the levels found in the stellar and H I size–mass relations (~ 0.1 dex; cf. Wang et al. 2016; Trujillo et al. 2020) at approximately $\Sigma_{\rm mol}(r) \sim 5$ M$_\odot$ pc^{-2}, increasing both above and below this value. While a full exploration of this issue is beyond the scope of this work, we note that the H I size–mass relation is both tight and consistent across samples because of the physical threshold in central H I surface densities of galaxies, above which gas becomes molecular (Stevens et al. 2019). No equivalent restriction on central surface density applies to molecular gas (or stellar densities). Not only is the ceiling for central molecular surface densities much higher than H I, but Figure 9 shows variable and non-monotonic surface brightness (and therefore surface density) profiles are common. Naïvely, one would expect that the higher the threshold surface density used to define the iso-density radius, the more susceptible to variation in the surface density profiles the relationship is, thus increasing the scatter.

Molecular gas density profiles tend to be less well described by monotonically decreasing functions of radius than H I or stellar profiles, particularly at high resolution and sensitivity (e.g., Figure 9), and exhibit a wide range in concentration (e.g., Figure 11). Despite this, the small scatter in the measured gas disk size at fixed total mass suggests that galaxies tend to move along the size–mass relation, rather than deviating from it. Of course, this poses the altogether more interesting question, what is driving the observed diversity in molecular gas radial profile shapes? Addressing this will be the subject of future work aimed at establishing a physically motivated definition for the size of molecular gas disks. However, it interesting that the optimal iso-density value of $\Sigma_{\rm mol}(r) = 5$ M$_\odot$ pc^{-2} is consistent with the total gas surface densities of ~ 10 M$_\odot$ pc^{-2} where gas disks are theoretically predicted to transition from being H I- to H$_2$-dominated with an atomic-to-molecular ratio of ~ 0.5 at solar metallicity (Krumholz et al. 2009).

This work assumes a constant CO conversion factor across the sample. While this is likely a reasonable approximation given the mild gradients in $\alpha_{\rm CO}$ as a function of radius observed in most galaxy disks (Sandstrom et al. 2013), it is important to consider how the prevalence of lower $\alpha_{\rm CO}$ values in the inner parts of galaxies as well as other variations in the conversion factor (e.g., metallicity-driven) could impact the form of our observed iso-density size–mass relation (Wolfire et al. 2010; Sandstrom et al. 2013; Heyer & Dame 2015; Accurso et al. 2017). Since $\alpha_{\rm CO}$ is accounted for in both axes, a global variation in the conversion factor – without a change in shape between the CO and molecular gas surface density profiles – would simply shift galaxies along the relation. However, radially varying $\alpha_{\rm CO}$, as seen in some galaxies by Sandstrom et al. (2013) is more difficult to properly understand without further work. That said, an interesting quality of the iso-density size–mass relation is its insensitivity to the significant variations in the gas surface density profiles seen in the VERTICO sample. In other words, despite the large differences in CO distribution throughout the VERTICO sample, almost all galaxies fall on the combined sample size–mass relation. This suggests that changes in the conversion factor as a function of radius would have to dramatically alter the gas surface density profiles for the effect to be noticeable in the size–mass relation.

Lastly, it is notable that the optimal $\Sigma_{\rm mol}(r)$ should be in such good agreement with the predicted transition density, given the distance, $\alpha_{\rm CO}$, and flux calibration uncertainties on our observations, in addition to less well quantified physical effects such as metallicity variations and environment.

6. SUMMARY

The VERTICO survey has mapped CO$(2-1)$ in 51 Virgo Cluster galaxies on sub-kpc scales. The primary motivation of this project is to understand the physical mechanisms that drive galaxy evolution in dense environments, and provide a diverse, homogeneous legacy dataset for studying galaxy evolution in our closest galaxy cluster.

The 36 targets observed in ALMA Cycle 7 are combined with archival CO$(2-1)$ data for 15 Virgo Cluster spirals to make the final VERTICO sample of 51 galaxies. Our final data cubes have a resolving beam of $\sim 7-10''$, corresponding to $\sim 0.6-0.8$ kpc at the distance of Virgo, and 10 km s^{-1} velocity resolution. We provide global CO line luminosities and convert these into total molecular gas masses. We calculate $\mathrm{R}_{21} = 0.8$ for the 35 galaxies with existing CO$(1-0)$ data, in general agreement with other surveys of nearby galaxies.

We present the integrated intensity, velocity field, observed line width, and peak temperature maps for each galaxy. VERTICO's sensitivity and depth ensures that these maps reveal the imprint of stellar structure (e.g., spiral arms, bars, bulges) and environmental processes (e.g., warps, tails, depletion) in the gas morphology and kinematics in great detail. We measure integrated CO intensity radial profiles, which show a large range in gas disk morphologies across the VERTICO sample. A significant number of the profiles do not decrease steadily as a function of radius, showing bumps in the CO distribution at larger radii or signs of truncation at the outer edge of the disk.

We investigate the scaling relation between the size and mass of the molecular gas distribution in VERTICO galaxies. This is compared to the same relation for the HERACLES survey of field galaxies. We find the iso-density size–mass relation has less scatter and a stronger correlation than the flux-percentage radius size–mass relation. In agreement with studies of H I disks, we suggest that the observed consistency of the iso-density size–mass relation between field and cluster galaxies suggests environment is not a driving factor in this relationship. We interpret this as evidence that the environmental processes which perturb the distribution of molecular gas in galaxies also affect the global gas mass. In this way, galaxies undergoing environmental transformation move along the size–mass relation rather than deviating from it. Finally, we investigate the effect that radius definition has on this correlation and determine the optimal molecular gas iso-density ($\Sigma_{\rm mol}(r) \sim 5{\rm M}_\odot$ pc^{-2}) and flux-percentage ($r_{90,\,{\rm mol}}$) radius definitions that produce the least scatter and strongest correlation.

Our intent with this work is to provide an overview of the VERTICO survey and highlight its potential as a resource for revealing the role environment plays in galaxy evolution. To this end, VERTICO will be used to study the fate of molecular gas in cluster galaxies and the physics of environment-driven processes that perturb the star formation cycle. It is our hope that VERTICO advances our understanding and provides a valuable legacy resource that serves the community for years to come.

ACKNOWLEDGMENTS

The majority of this work was conducted on the traditional territory of the Lekwungen peoples. We acknowledge and respect the Songhees, Esquimalt and WSÁNEĆ Nations whose historical relationships with the land continue to this day.

We thank the anonymous referee for a considered and constructive review that improved the manuscript.

This work was carried out as part of the VERTICO collaboration.

The authors wish to thank the members of the PHANGS-ALMA collaboration for their support and advice in reducing the VERTICO data. In particular, we thank Adam Leroy for graciously providing us with the PHANGS-ALMA ACA data and imaging pipeline in advance of publication.

TB acknowledges support from the National Research Council of Canada via the Plaskett Fellowship of the Dominion Astrophysical Observatory. CDW acknowledges support from the Natural Sciences and Engineering Research Council of Canada and the Canada Research Chairs program. TAD acknowledges support from STFC grant ST/S00033X/1. LP, JW, and KS acknowledge support from the Natural Science and Engineering Council of Canada. LC acknowledges support from the Australian Research Council's Discovery Project and Future Fellowship funding schemes (DP210100337, FT180100066). ARHS acknowledges receipt of the Jim Buckee Fellowship at ICRAR-UWA. IDR acknowledges support from the ERC Starting Grant Cluster Web 804208. KPO is funded by NASA under award No 80NSSC19K1651. V. Villanueva acknowledges support from the scholarship CONICYT PFCHA/ CONICYT-FULBRIGHT BIO 2016 - 56160020 and funding from NRAO Student Observing Support (SOS) - SOSPA7-014. Support for this work was also provided by the National Research Foundation of Korea (NRF) grant No. 2018R1D1A1B07048314. BL acknowledges support from the National Science Foundation of China (12073002, 11721303). YMB gratefully acknowledges funding from the Netherlands Organization for Scientific Research (NWO) through Veni grant number 639.041.751. CW acknowledges the support of the National Science Foundation award 1815251 (United States) held by Dr. Susan Kassin. Parts of this research were conducted by the Australian Research Council Centre of Excellence for All Sky Astrophysics in 3 Dimensions (ASTRO 3D), through project number CE170100013. MHH acknowledges support from the William and Caroline Herschel Postdoctoral Fellowship fund. CDPL has received funding from ASTRO 3D through project number CE170100013. PJE works on Whadjuk country and pays respect to the elders past, present and emerging of the Noongar people. CRC acknowledges support from STFC grant ST/R000840/1.

This paper makes use of the following ALMA data:
ADS/JAO.ALMA#2019.1.00763.L,
ADS/JAO.ALMA#2017.1.00886.L,
ADS/JAO.ALMA#2016.1.00912.S,
ADS/JAO.ALMA#2015.1.00956.S.
ALMA is a partnership of ESO (representing its member states), NSF (USA) and NINS (Japan), together with NRC (Canada), MOST and ASIAA (Taiwan), and KASI (Republic of Korea), in cooperation with the Re-

public of Chile. The Joint ALMA Observatory is operated by ESO, AUI/NRAO and NAOJ. The National Radio Astronomy Observatory is a facility of the National Science Foundation operated under cooperative agreement by Associated Universities, Inc.

In addition to the ALMA Science Archive, research made use of data and/or software provided by the following archives:

- NASA/IPAC Infrared Science Archive, which is funded by the National Aeronautics and Space Administration and operated by the California Institute of Technology
- NASA/IPAC Extragalactic Database (NED), which is operated by the Jet Propulsion Laboratory, California Institute of Technology, under contract with the National Aeronautics and Space Administration.
- The High Energy Astrophysics Science Archive Research Center (HEASARC), which is a service of the Astrophysics Science Division at NASA/GSFC.
- The HRS data was accessed through the Herschel Database in Marseille (HeDaM - http://hedam.lam.fr) operated by CeSAM and hosted by the Laboratoire d'Astrophysique de Marseille.

We acknowledge the use of the ARCADE (ALMA Reduction in the CANFAR Data Environment) science platform. ARCADE is a ALMA Cycle 7 development study with support from the National Radio Astronomy Observatory, the North American ALMA Science center, and the National Research center of Canada. Our work used the facilities of the Canadian Astronomy Data center, operated by the National Research Council of Canada with the support of the Canadian Space Agency, and the Canadian Advanced Network for Astronomy Research, a consortium that serves data-intensive storage, access, and processing needs of university groups and centers engaged in astronomy research (Gaudet et al. 2010).

This research has made use of data from the Herschel Reference Survey (HRS) project. HRS is a Herschel Key Programme utilizing Guaranteed Time from the SPIRE instrument team, ESAC scientists and a mission scientist.

Here we acknowledge the key software used in this work:

- Astropy, a community-developed core PYTHON package for Astronomy and affiliated packages (SPECTRAL-CUBE, REPROJECT, PHOTUTILS; Astropy Collaboration et al. 2013; Price-Whelan et al. 2018; Bradley et al. 2020).
- The CASA (Common Astronomy Software Applications) package, a suite of applications for the reduction and analysis of radio astronomical data with a PYTHON interface (McMullin et al. 2007).
- PHANGS-ALMA Imaging Pipeline, a library of programs that use CASA, Astropy, and affiliated packages (ANALYSISUTILS, SPECTRAL-CUBE, REPROJECT) to process data from the calibrated visibilities to science-ready data cubes (Leroy et al. 2021b).
- MATPLOTLIB, a plotting library for the PYTHON programming language and its numerical mathematics extension NUMPY (Hunter 2007; Virtanen et al. 2020).
- PANDAS, an open source, BSD-licensed library providing high-performance, easy-to-use data structures and data analysis tools for the PYTHON programming language (Wes McKinney 2010).
- CARTA: The Cube Analysis and Rendering Tool for Astronomy, an image visualization and analysis tool for radio astronomy data (Comrie et al. 2020).
- The Ancillary Data Button, a selection of PYTHON scripts for acquiring and standardising imaging data from a wide range of telescopes (Clark et al. 2018).
- RSMF (right-size my figures), a PYTHON library that provides a means to automatically adjust figure sizes and font sizes in MATPLOTLIB to fit those commonly used in scientific journals.
- The Chandra Interactive Analysis of Observations application package developed by the Chandra X-ray Center for analyzing X-ray data (Fruscione et al. 2006).

APPENDIX

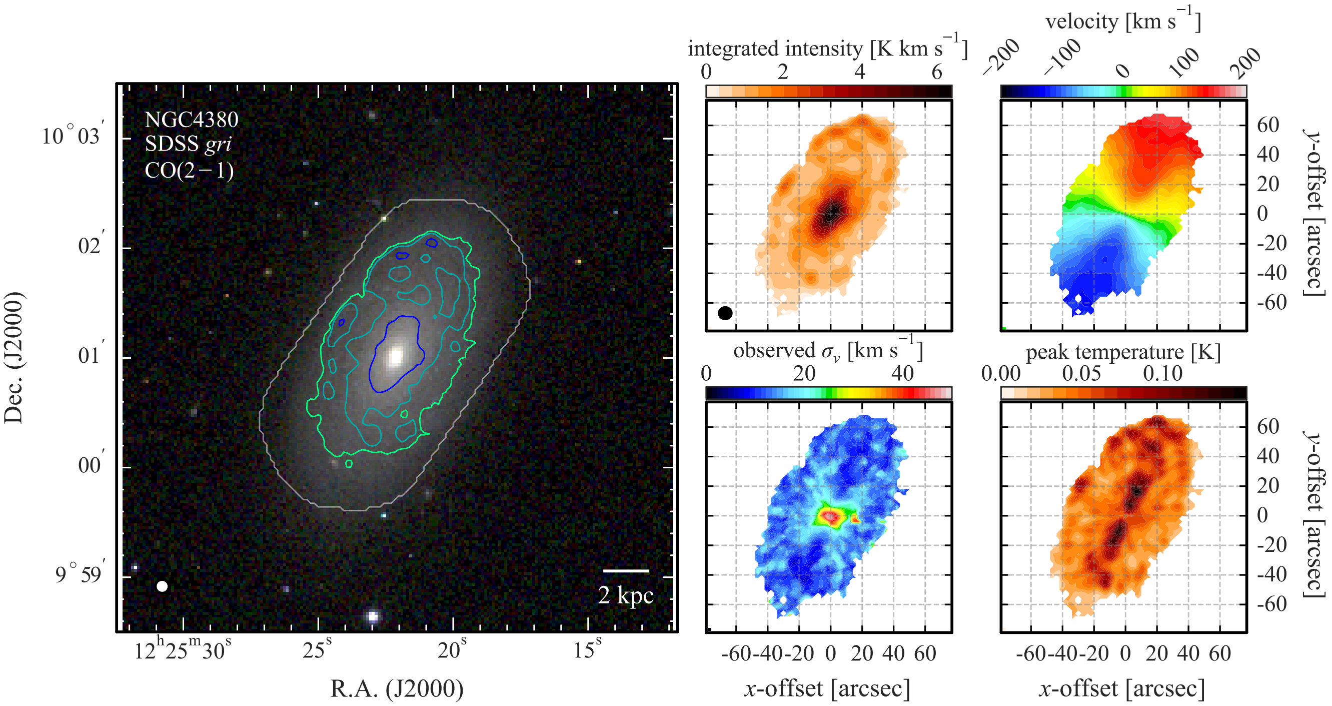

Figure 4.1. An example of the CO$(2-1)$ data products available for each galaxy in the VERTICO survey. The left panel shows the SDSS *gri* composite image for NGC4380 with molecular gas surface brightness contours at the 10th, 50th, and 90th percentiles of the distribution. The field of view of the ACA observations is defined where the primary beam response drops to 50% and is illustrated by the gray line. The rounded synthesized beam is $7.5''$ in diameter and illustrated in the bottom left corner. This beam corresponds to ∼600 pc at the distance of Virgo (16.5 Mpc). The VERTICO CO$(2-1)$ data products available for each galaxy include maps of integrated intensity (upper center panel), the velocity field (upper right), observed line width, σ_v (lower center), and peak temperature (lower left). The x- and y-axes of each moment map shows the angular offset from the optical center listed in Table 1.

A. VERTICO CO$(2-1)$ PANEL PLOTS

Fig. Set 4. CO$(2-1)$ data products available for each galaxy in the VERTICO survey

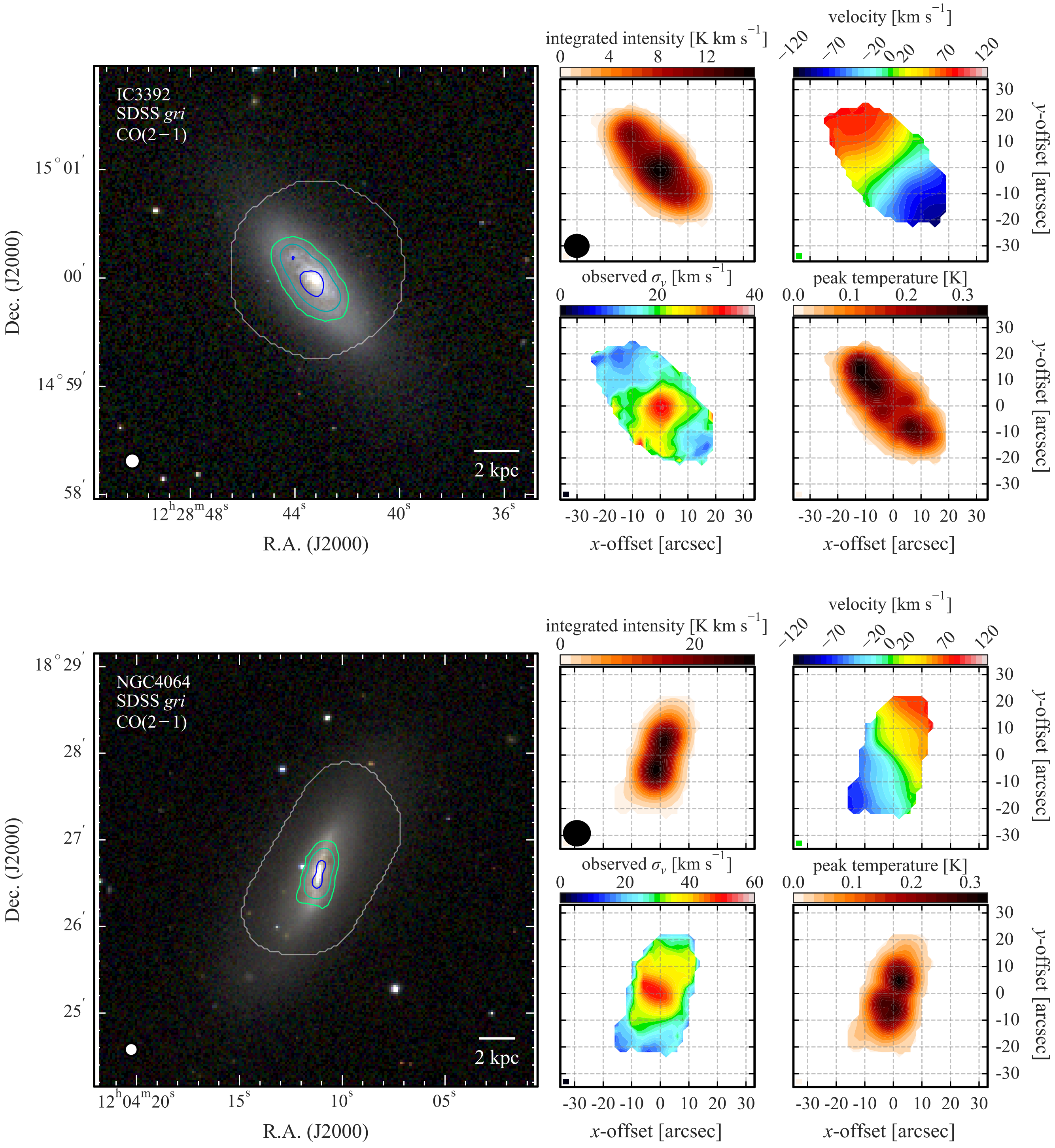

Figure 4.2. As in Figure 4.1.

B. EMISSION LINE SPECTRA

An example of the global CO(2 − 1) spectra derived from the masked data cubes described in 4.3 are shown in Figure 13. The complete Figure Set of ^{12}CO(2 − 1) spectra for all 51 VERTICO galaxies is available below.

Fig. Set 13. CO(2 − 1) spectra for each galaxy in the VERTICO survey

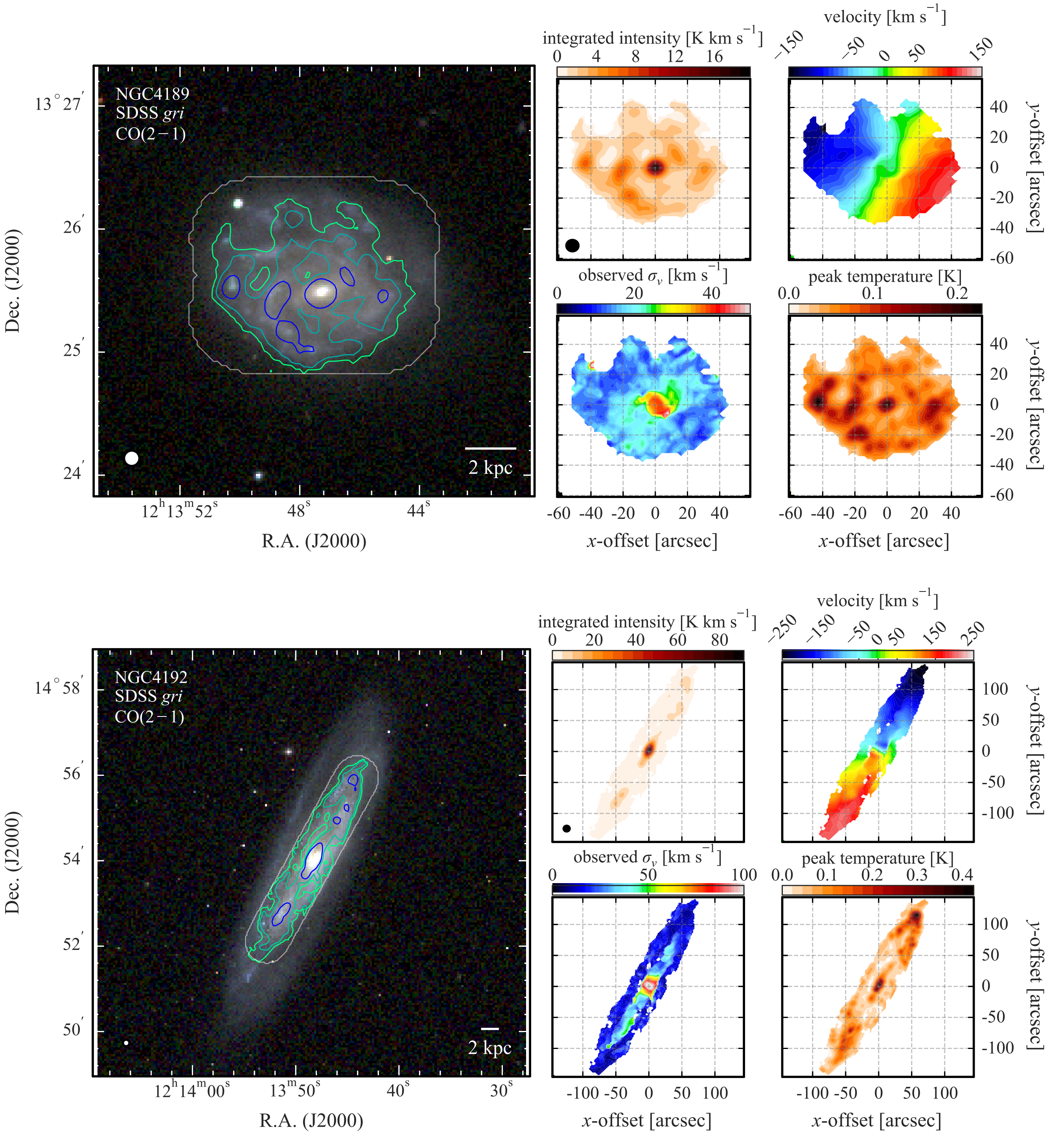

Figure 4.3. As in Figure 4.1.

REFERENCES

Accurso, G., Saintonge, A., Catinella, B., et al. 2017, MNRAS, 470, 4750, doi: 10.1093/mnras/stx1556

Alam, S., Albareti, F. D., Allende Prieto, C., et al. 2015, ApJS, 219, 12, doi: 10.1088/0067-0049/219/1/12

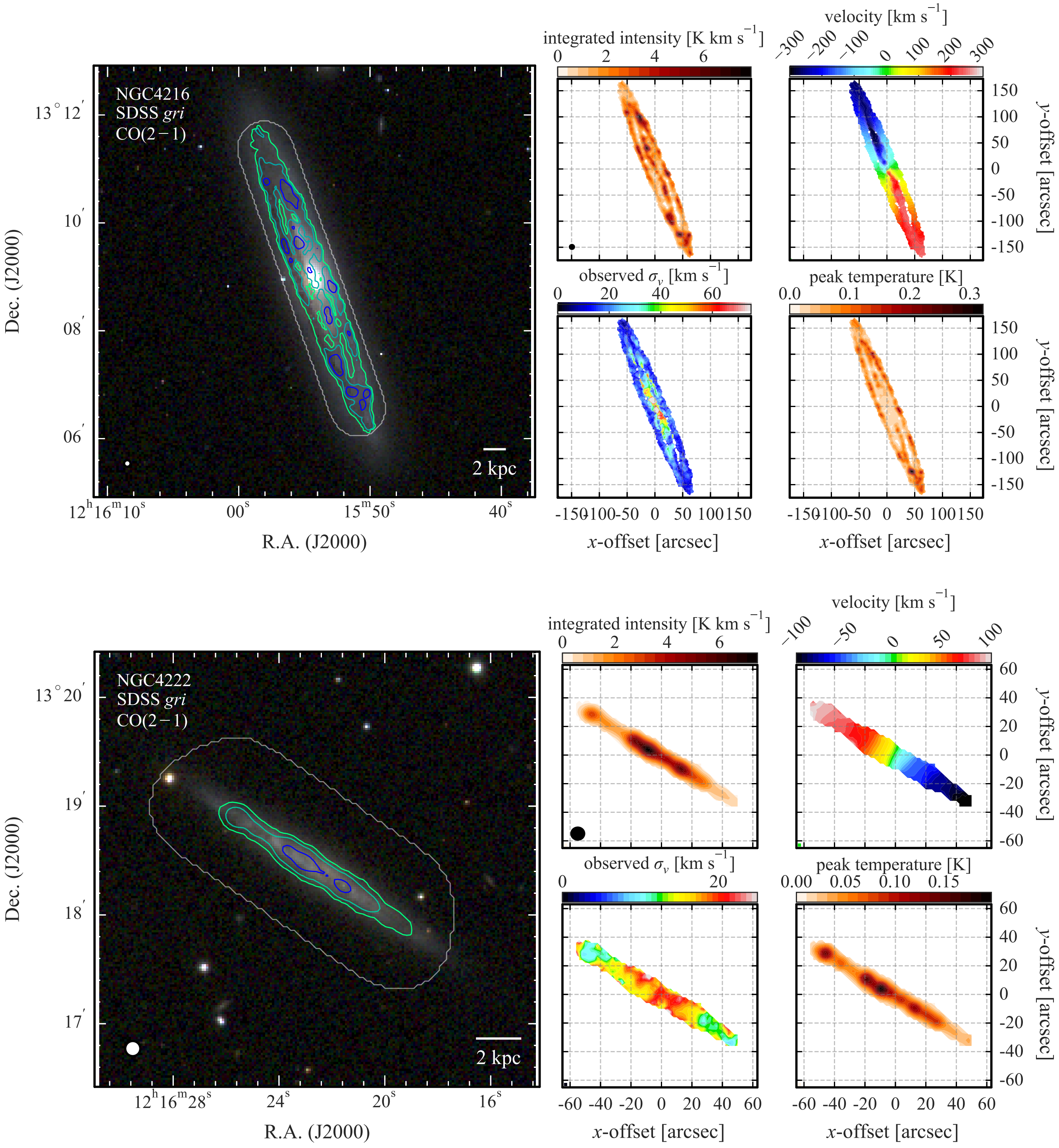

Figure 4.4. As in Figure 4.1.

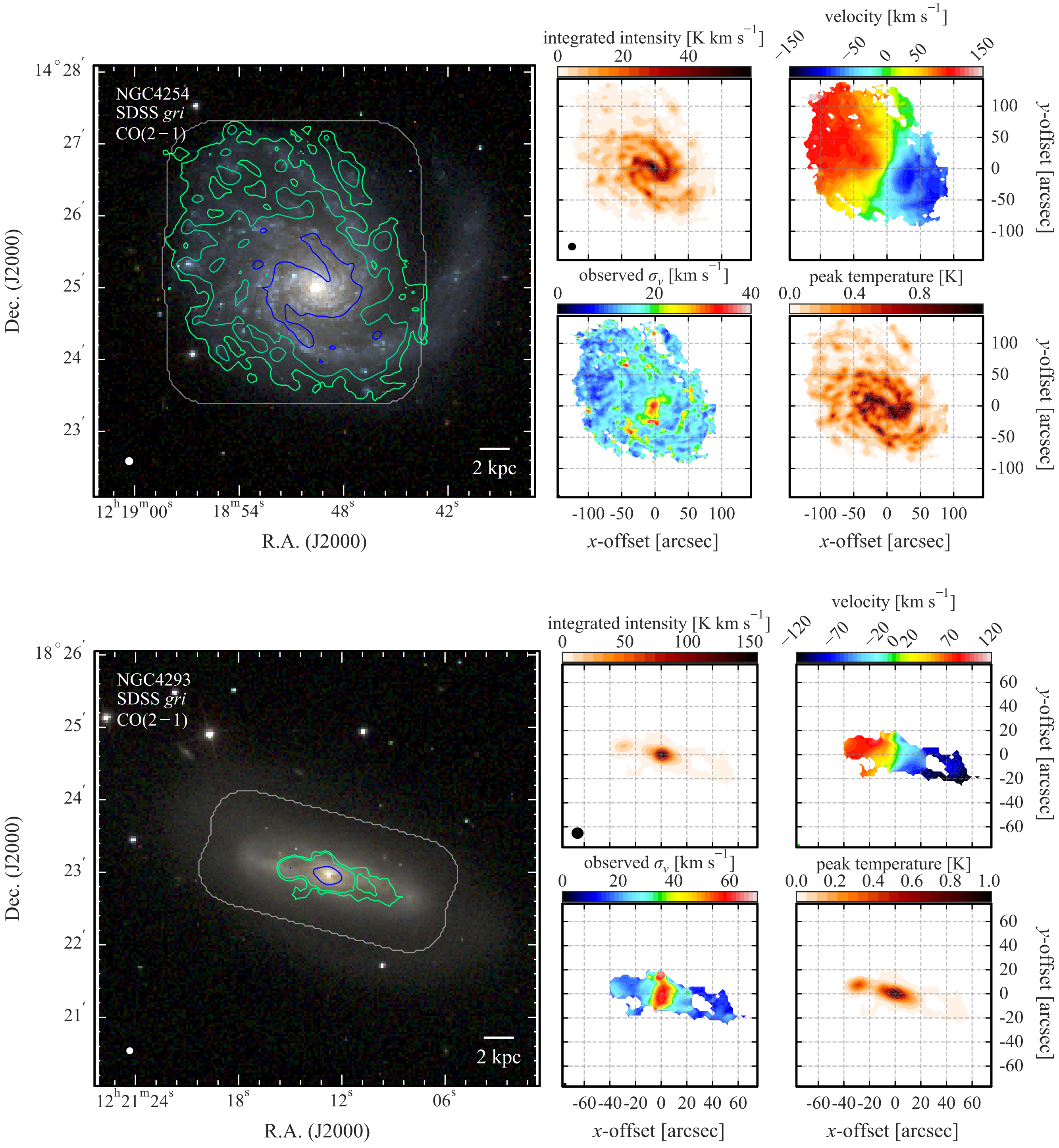

Figure 4.5. As in Figure 4.1. In the case of NGC4293, we caution against over-interpreting the skinny feature to the South-East of the main disk as this is likely related to the PSF pattern of the observations.

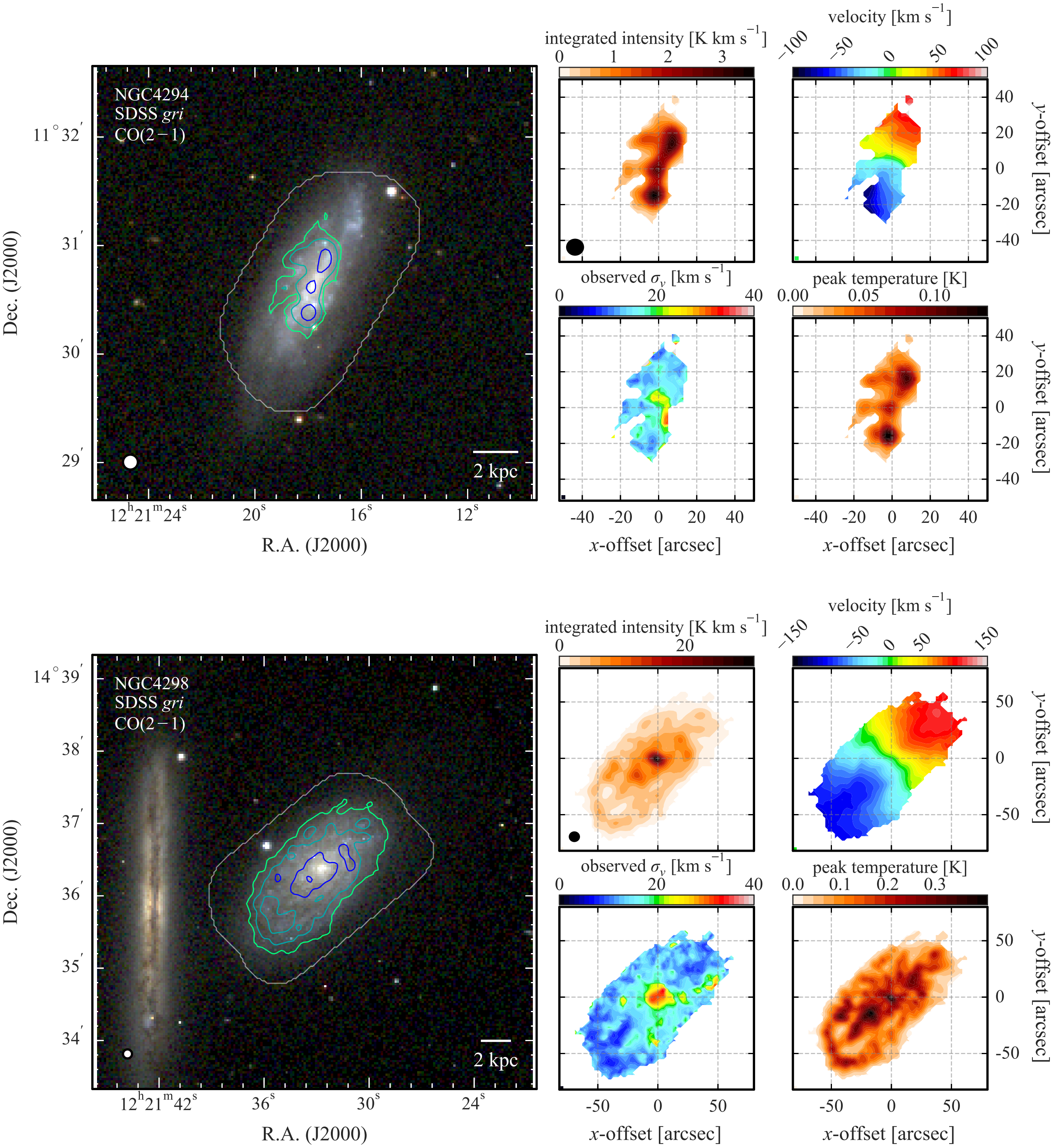

Figure 4.6. As in Figure 4.1.

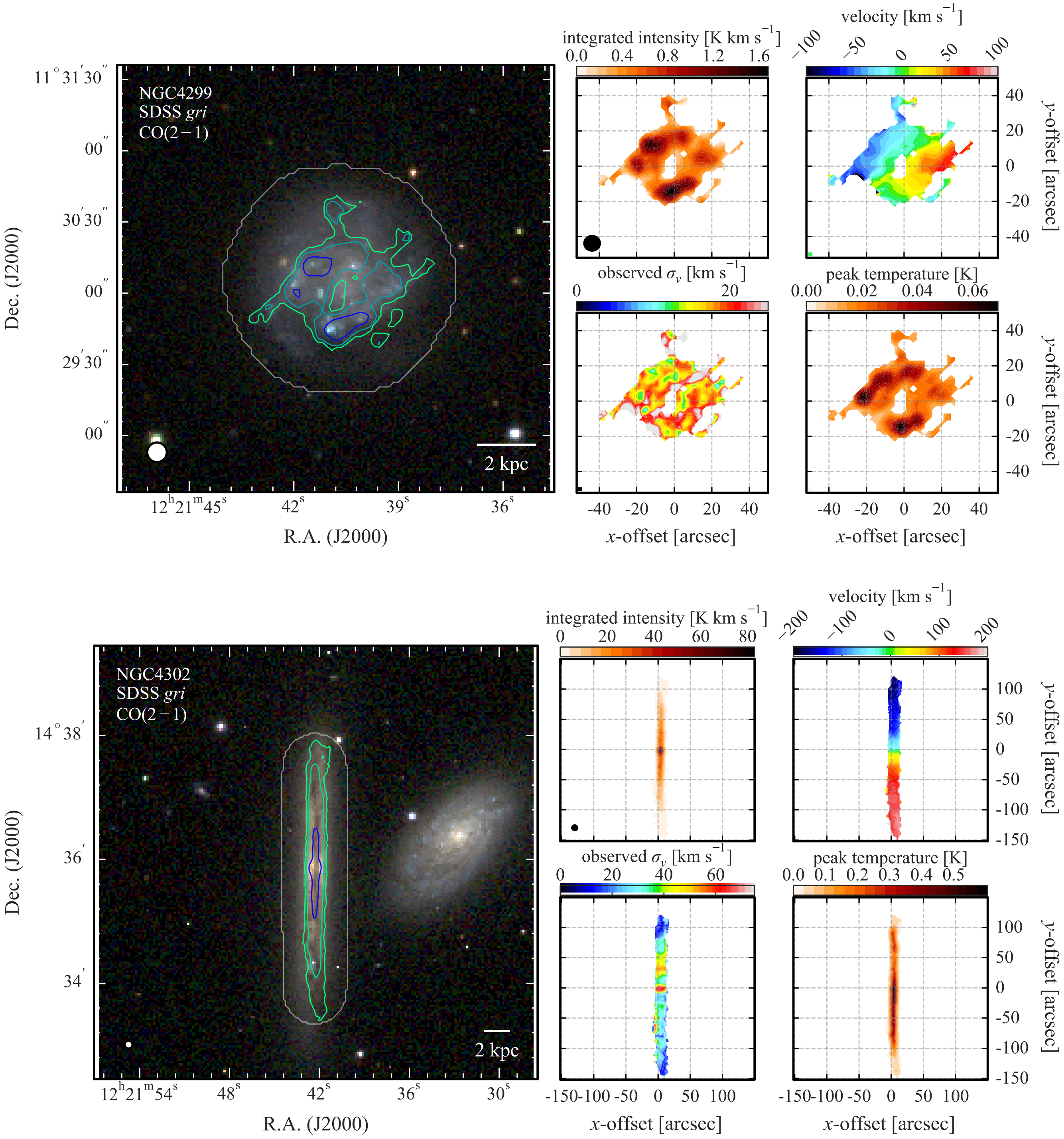

Figure 4.7. As in Figure 4.1.

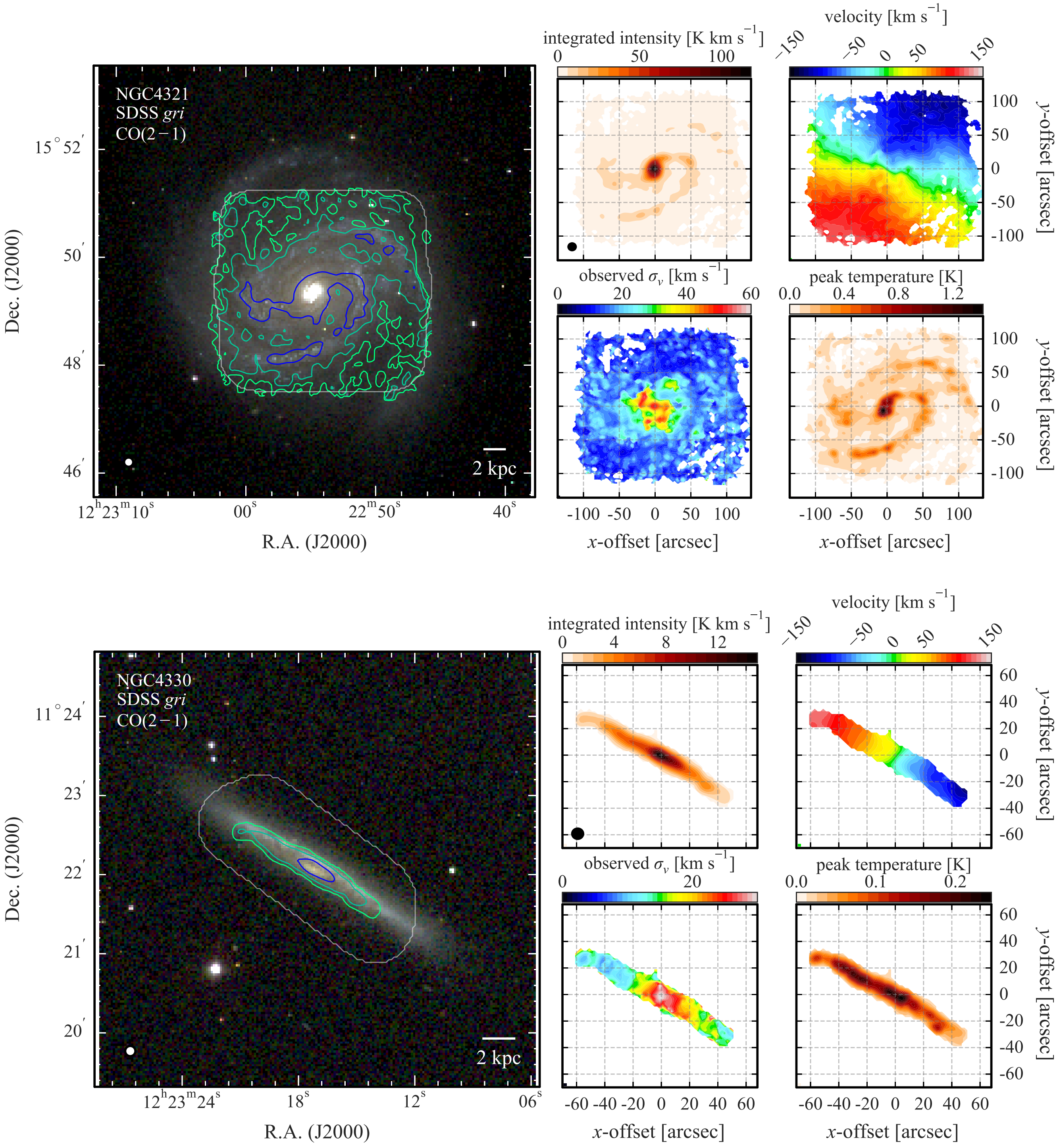

Figure 4.8. As in Figure 4.1.

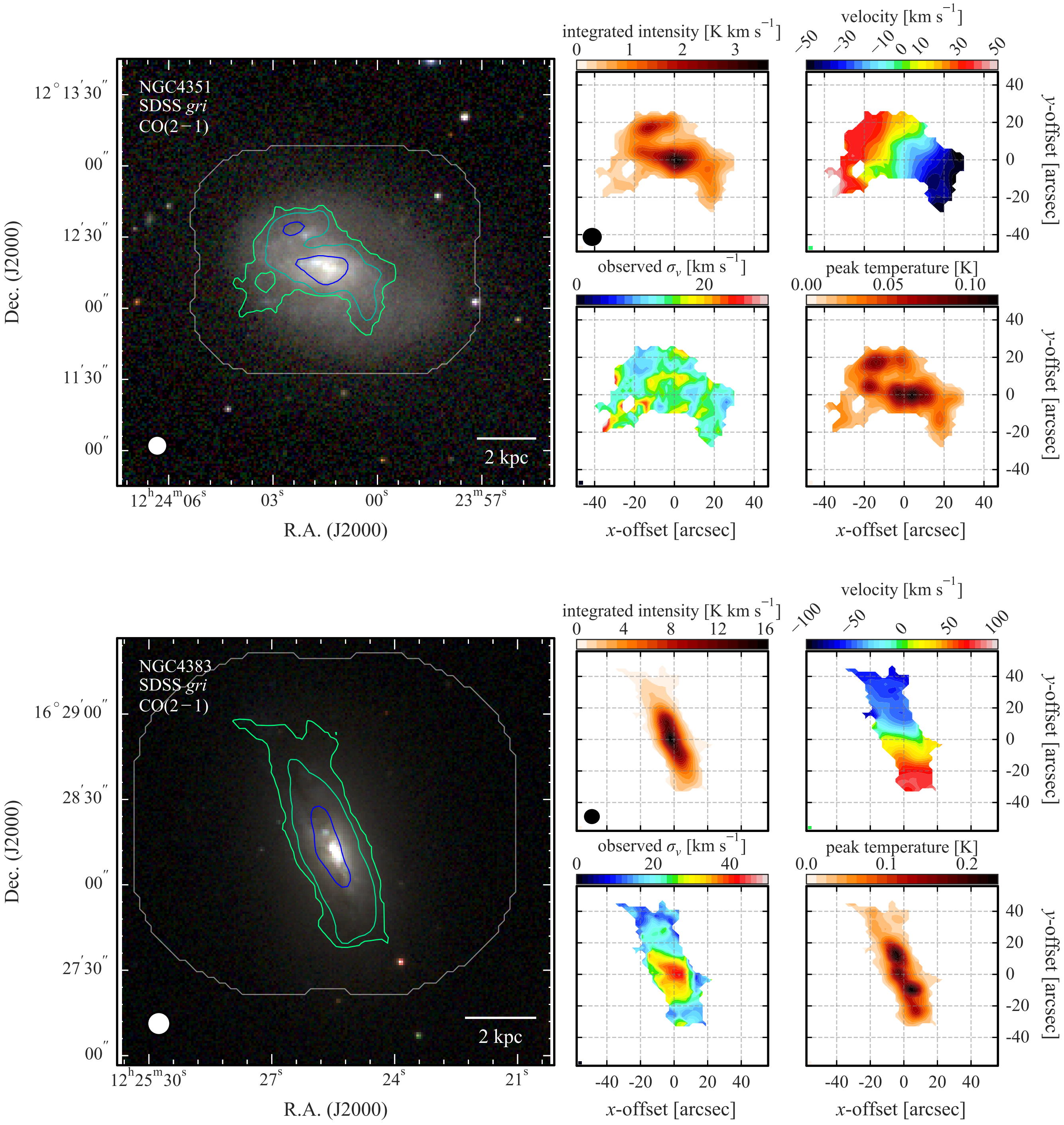

Figure 4.9. As in Figure 4.1.

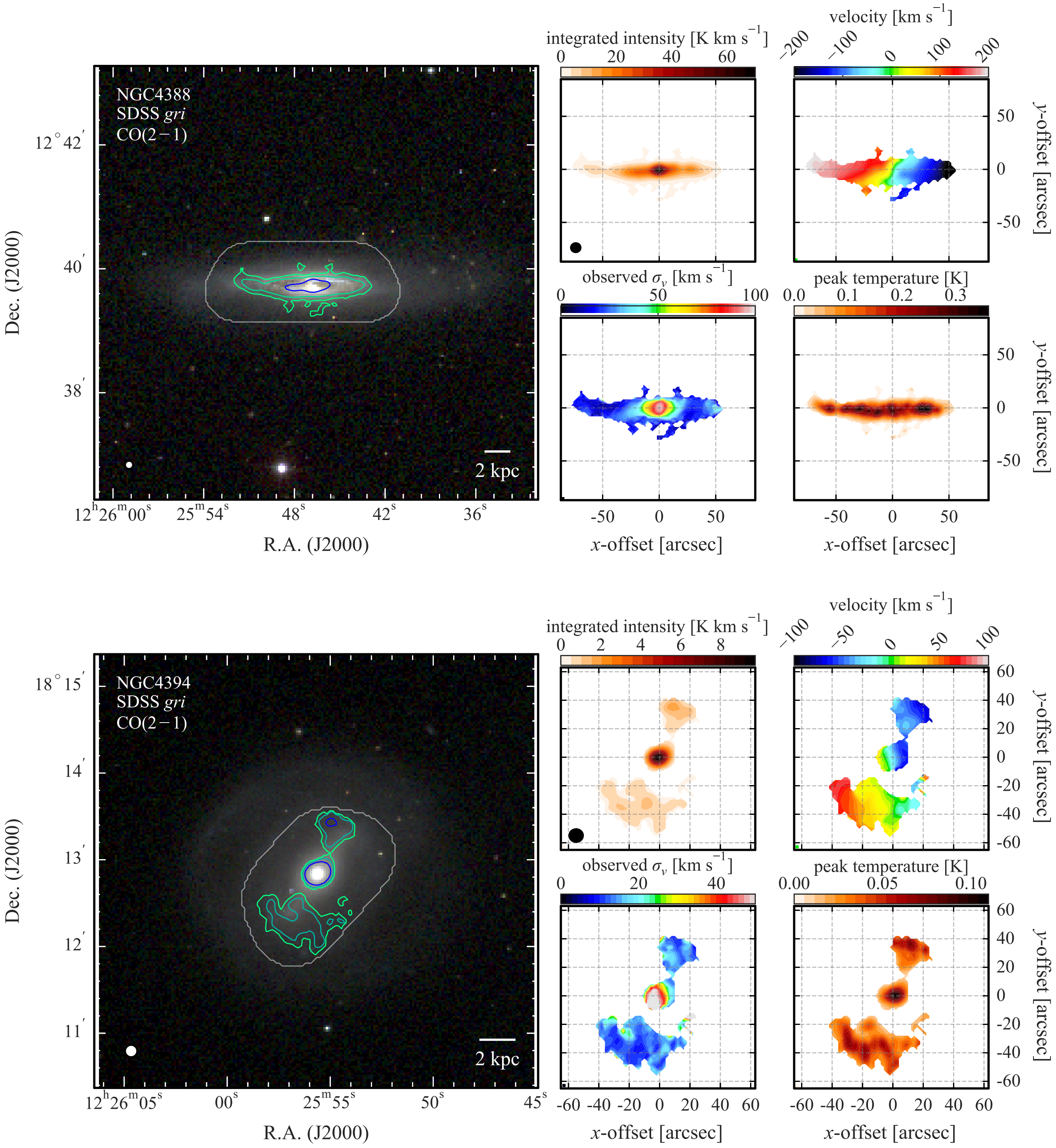

Figure 4.10. As in Figure 4.1.

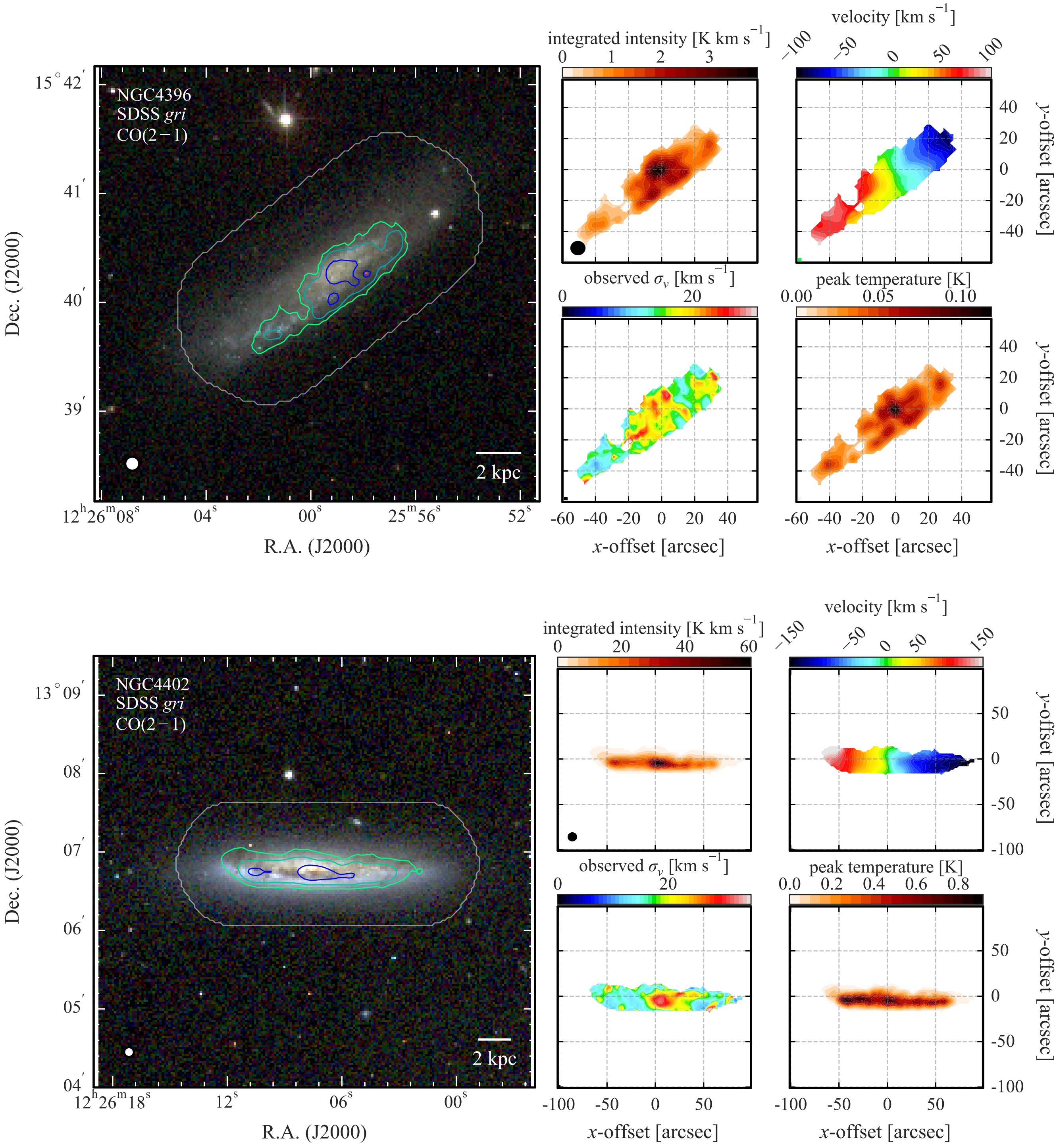

Figure 4.11. As in Figure 4.1.

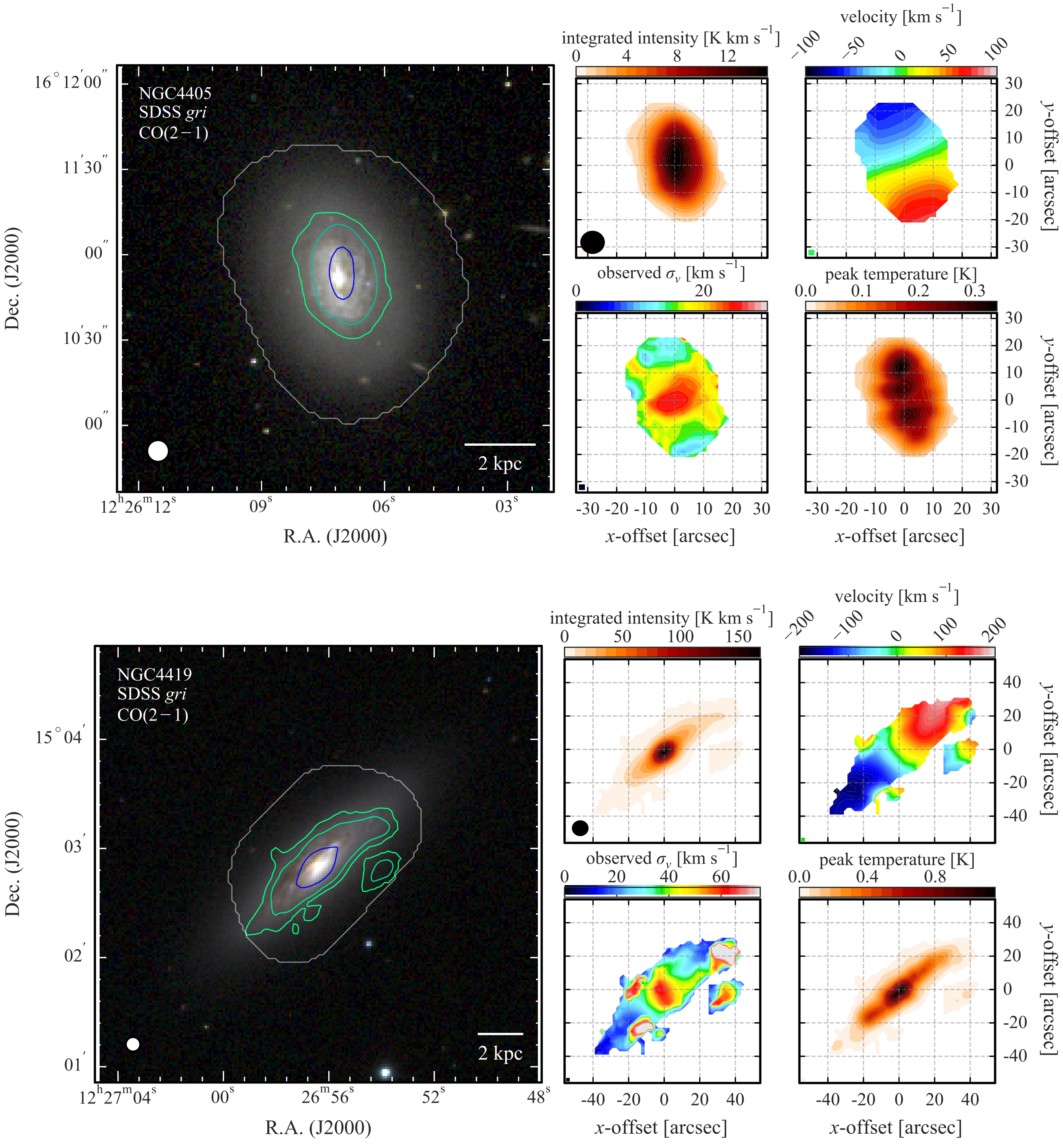

Figure 4.12. As in Figure 4.1.

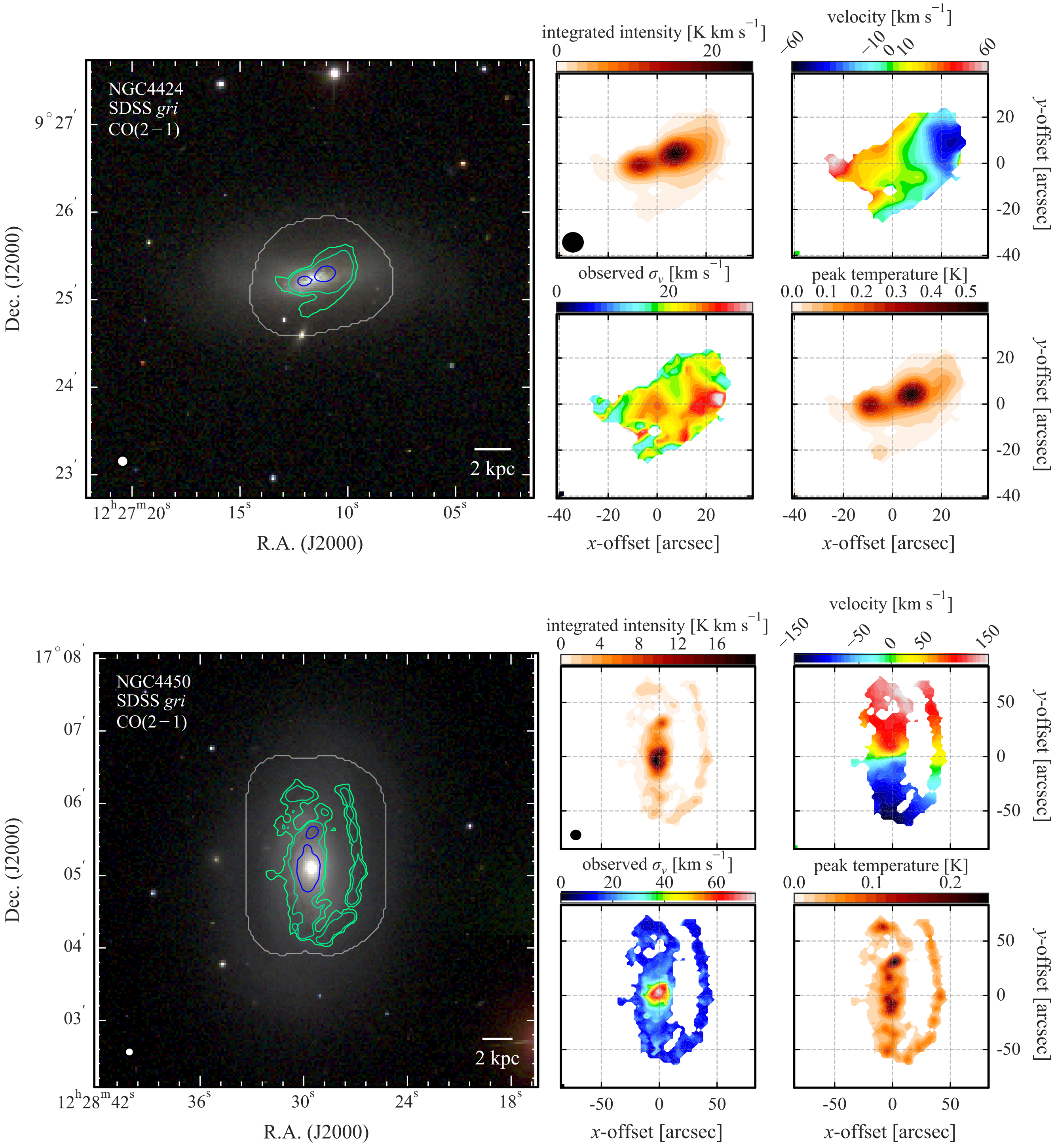

Figure 4.13. As in Figure 4.1.

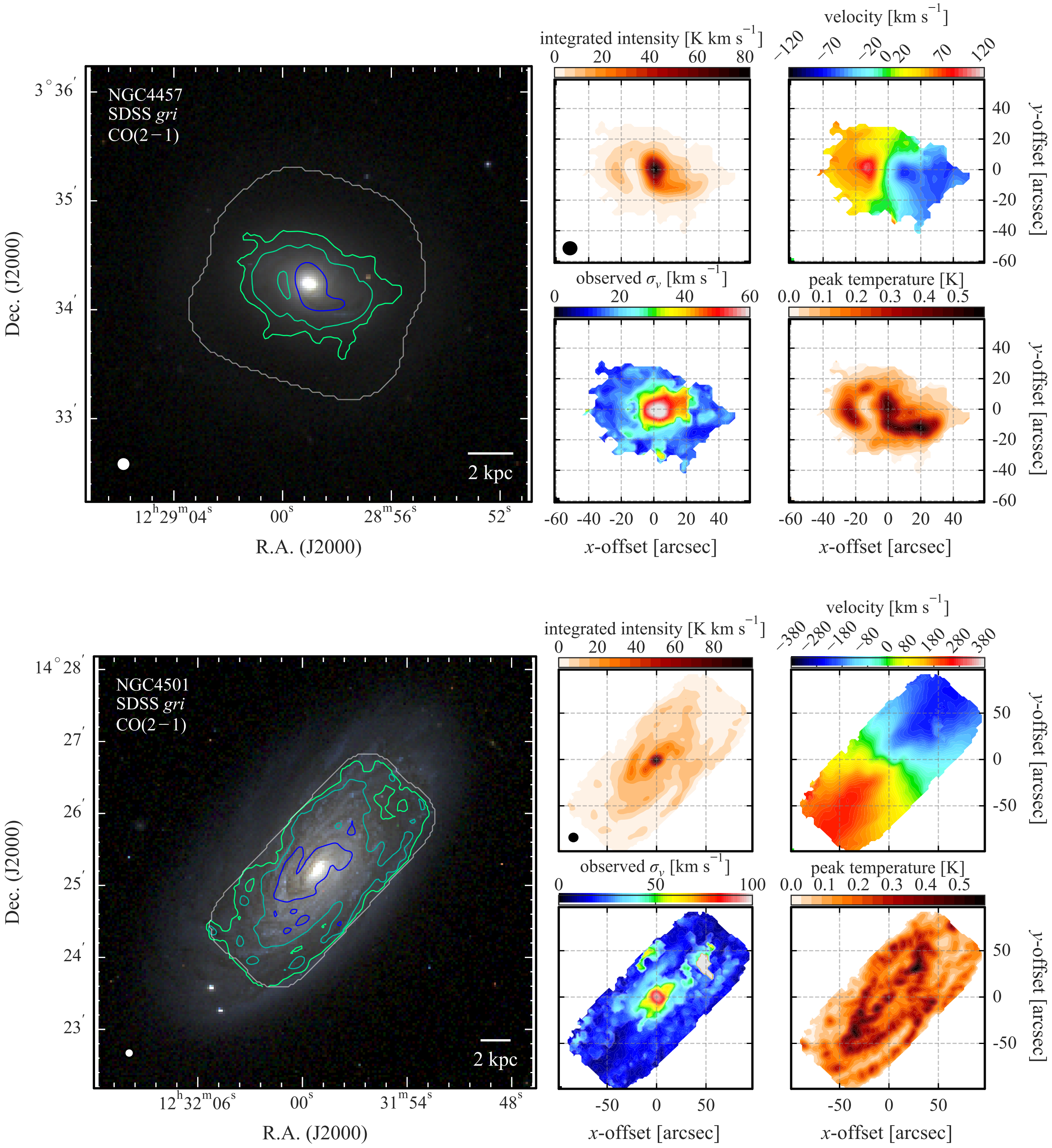

Figure 4.14. As in Figure 4.1.

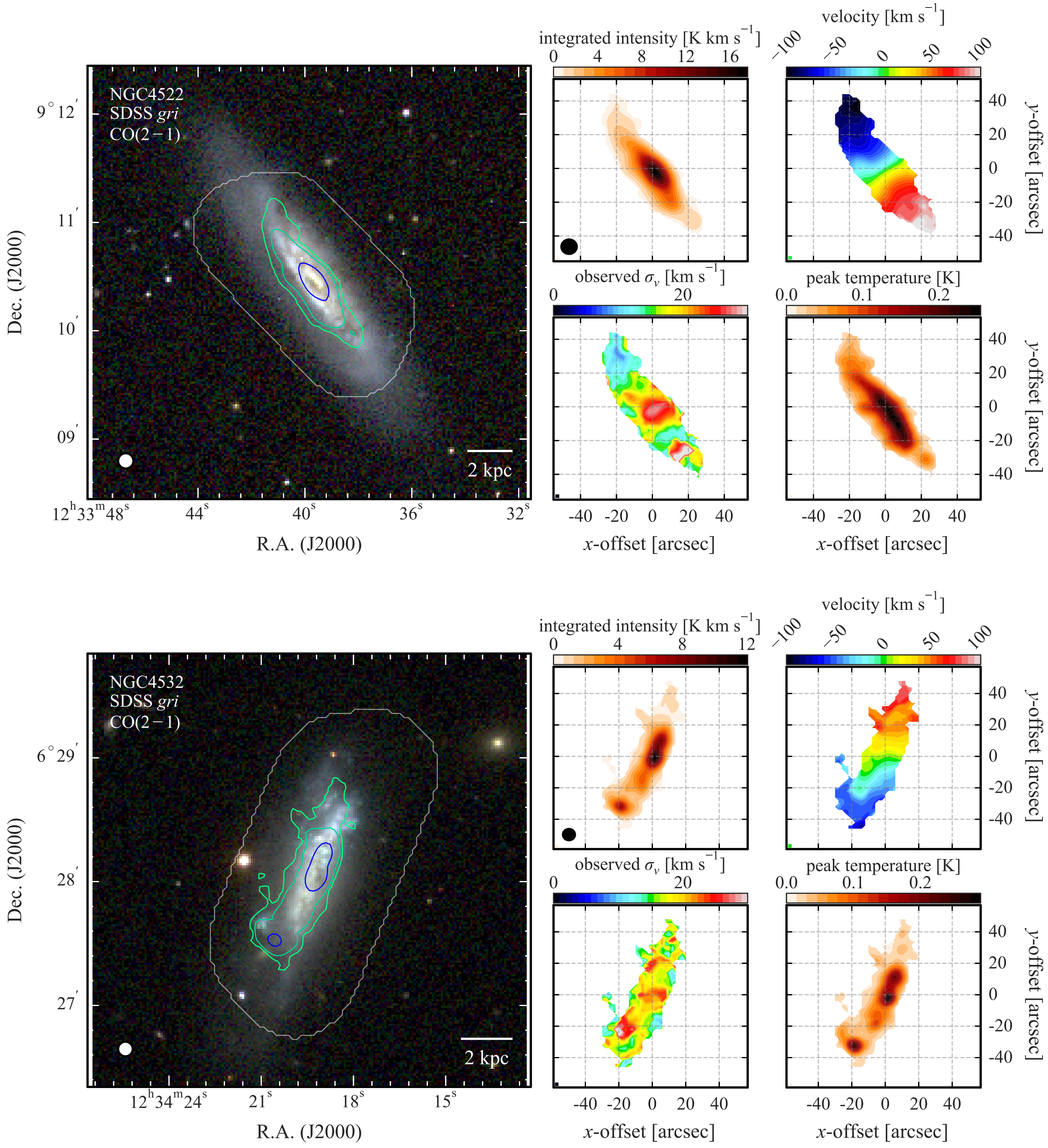

Figure 4.15. As in Figure 4.1.

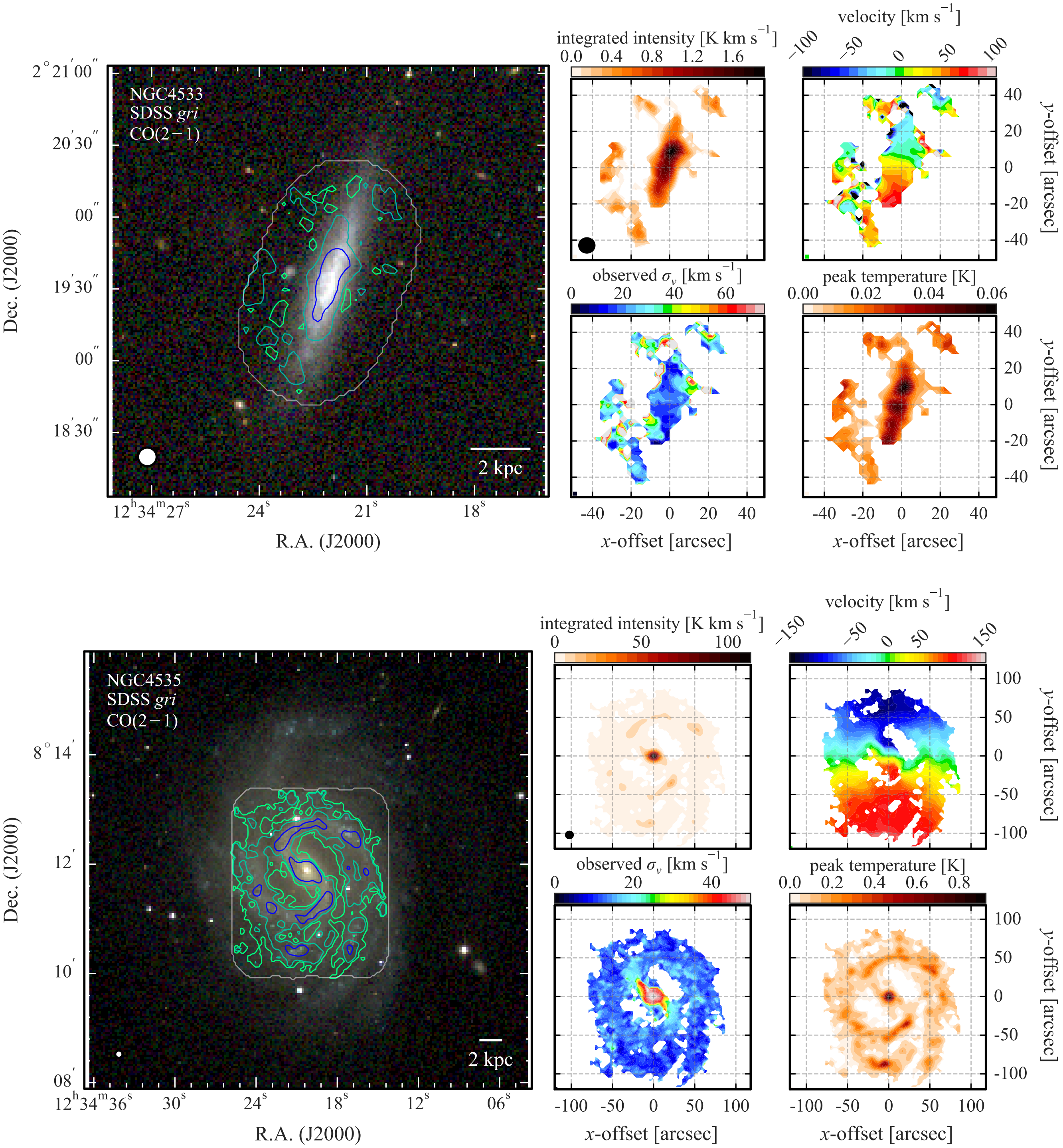

Figure 4.16. As in Figure 4.1.

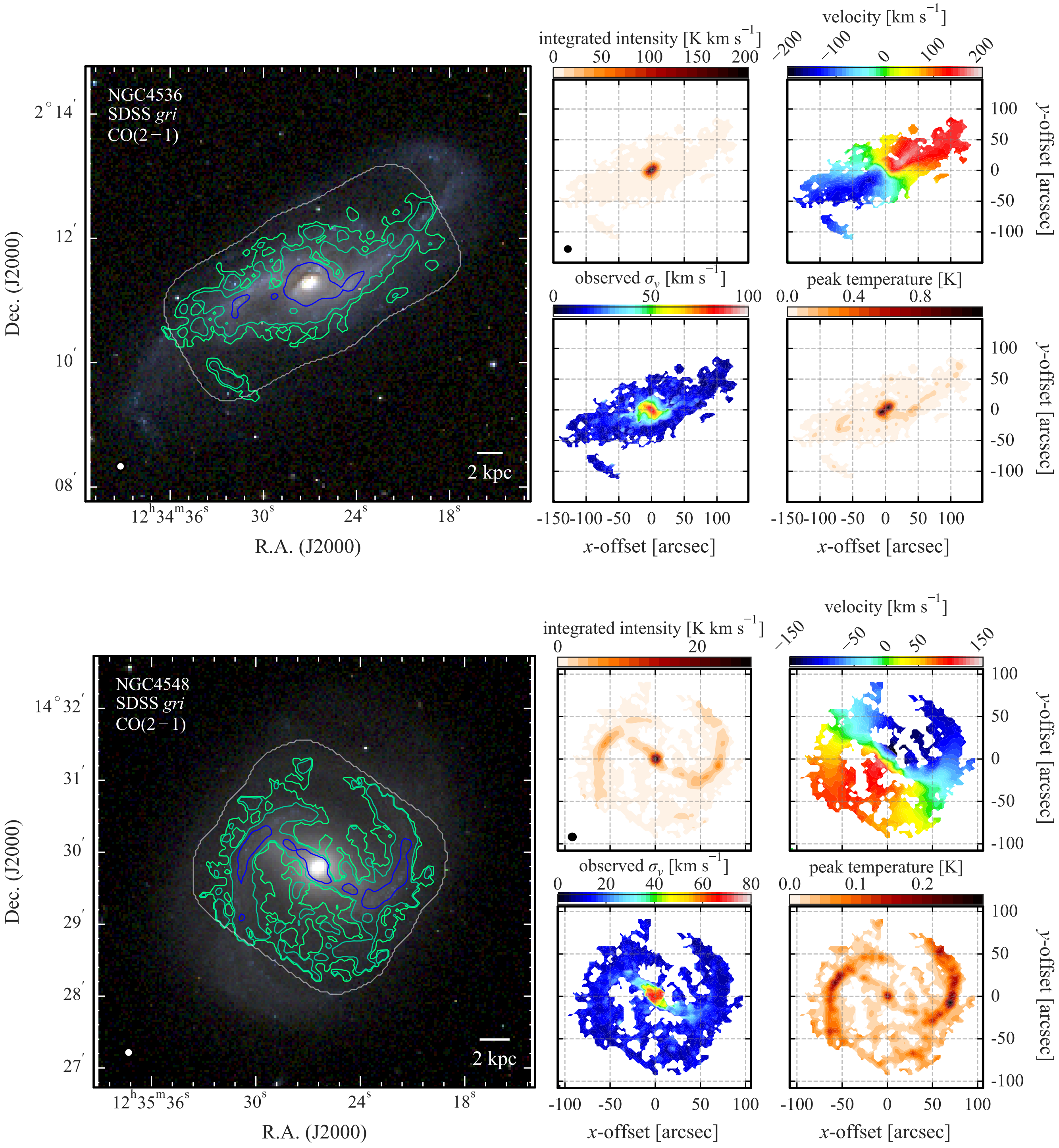

Figure 4.17. As in Figure 4.1.

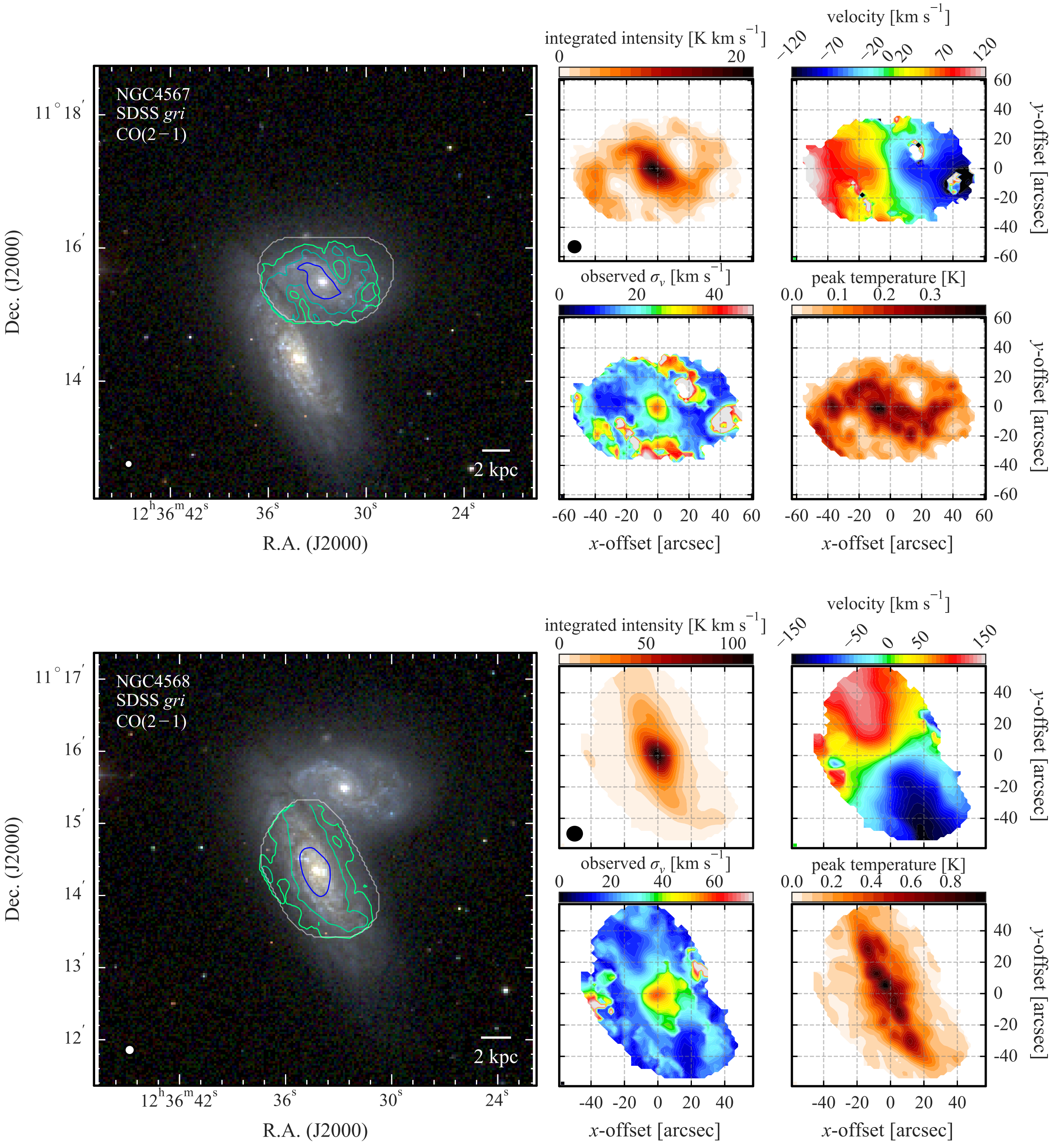

Figure 4.18. As in Figure 4.1.

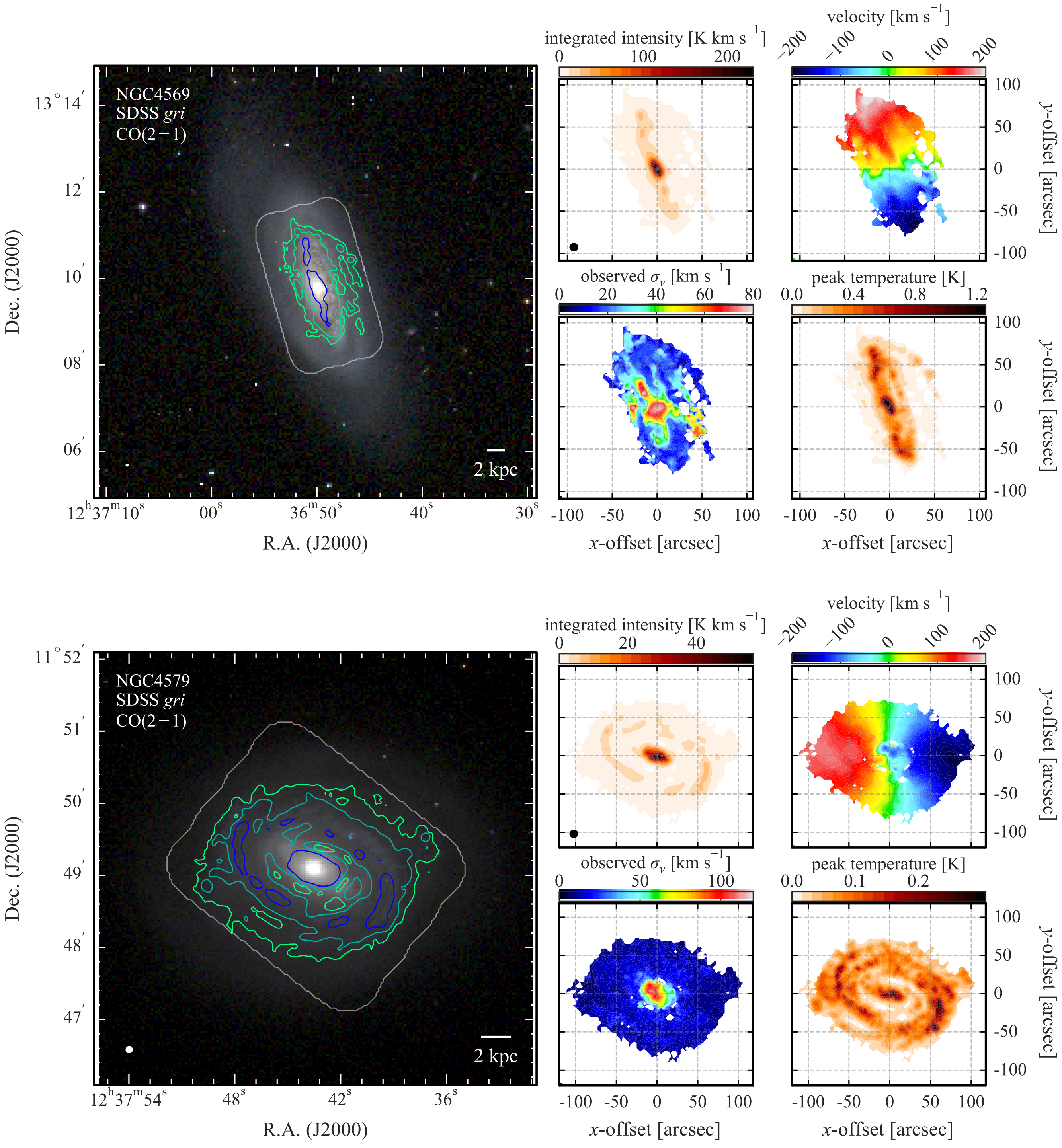

Figure 4.19. As in Figure 4.1.

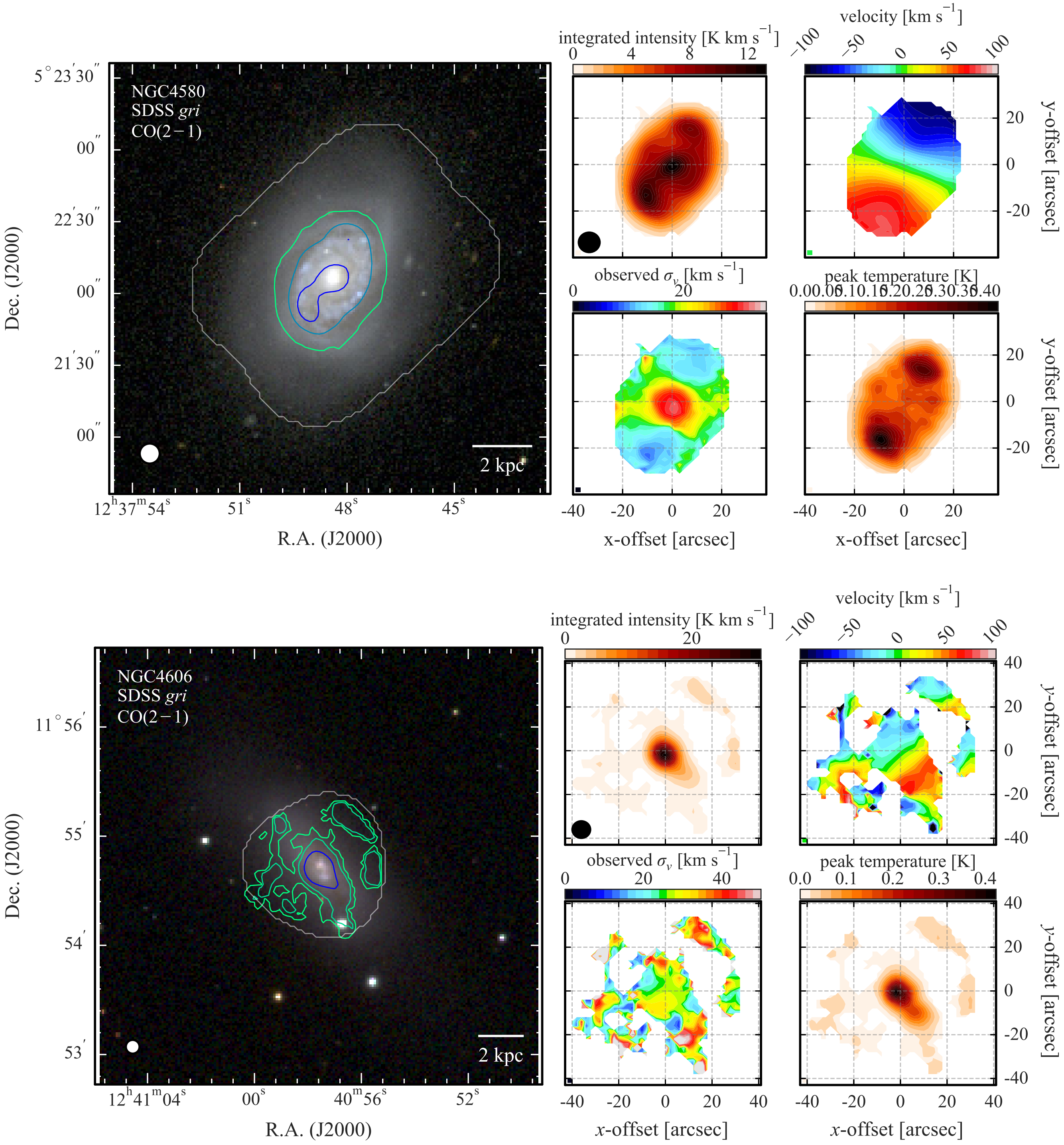

Figure 4.20. As in Figure 4.1.

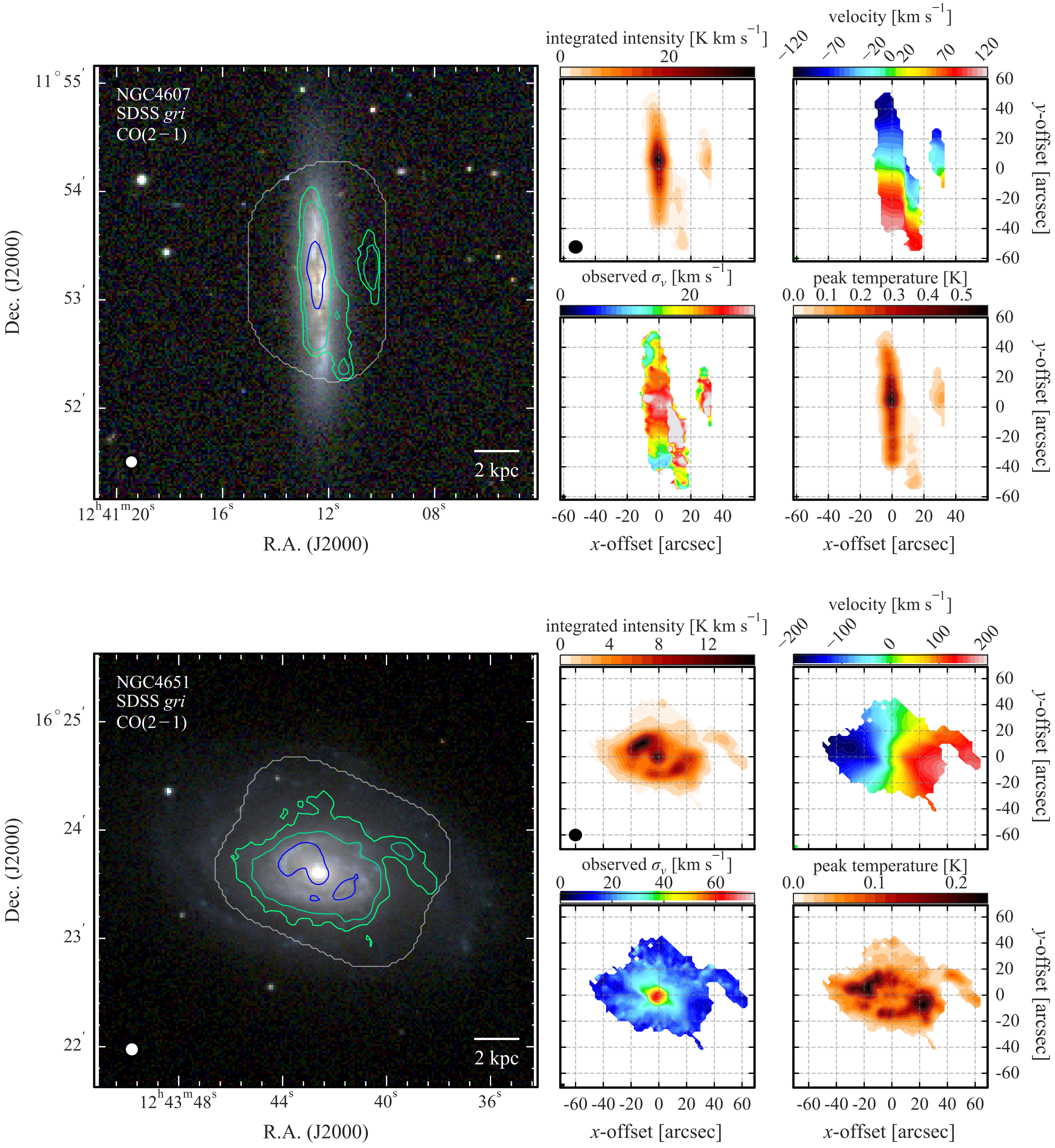

Figure 4.21. As in Figure 4.1. In the case of NGC4607, we caution against over-interpreting the extended features to the West of the main disk as this is likely related to the PSF pattern of the observations.

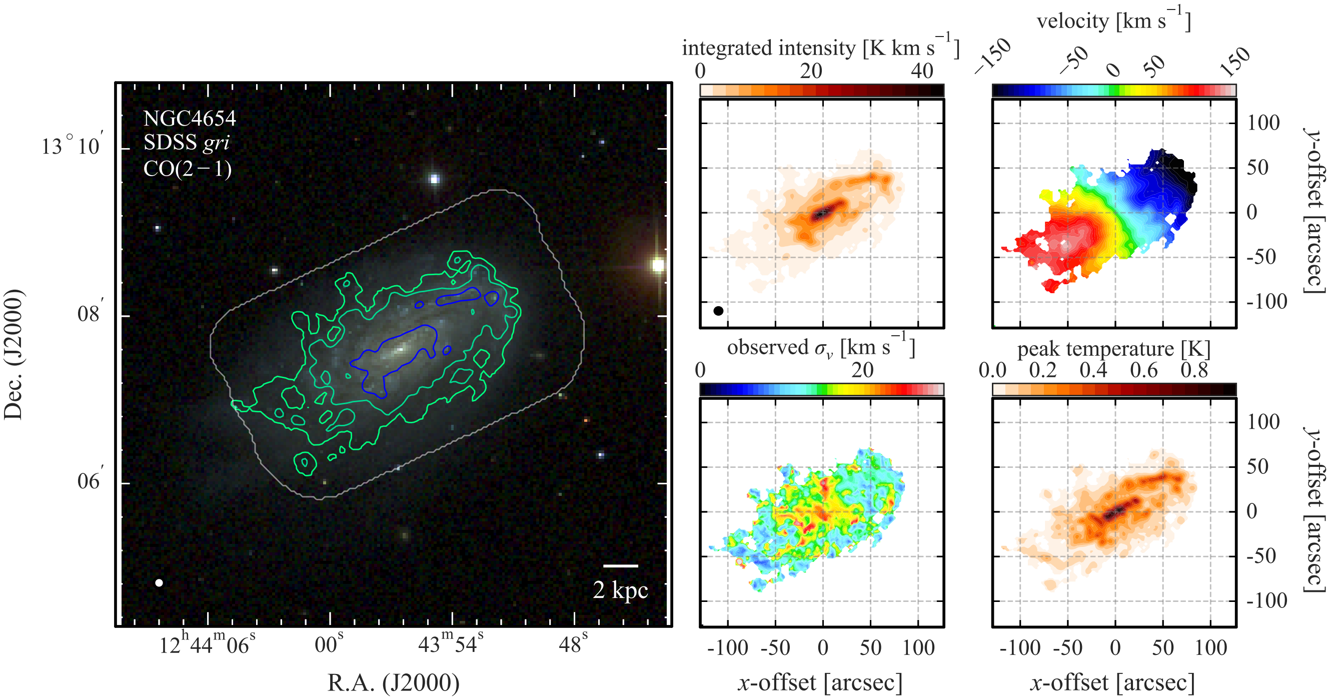

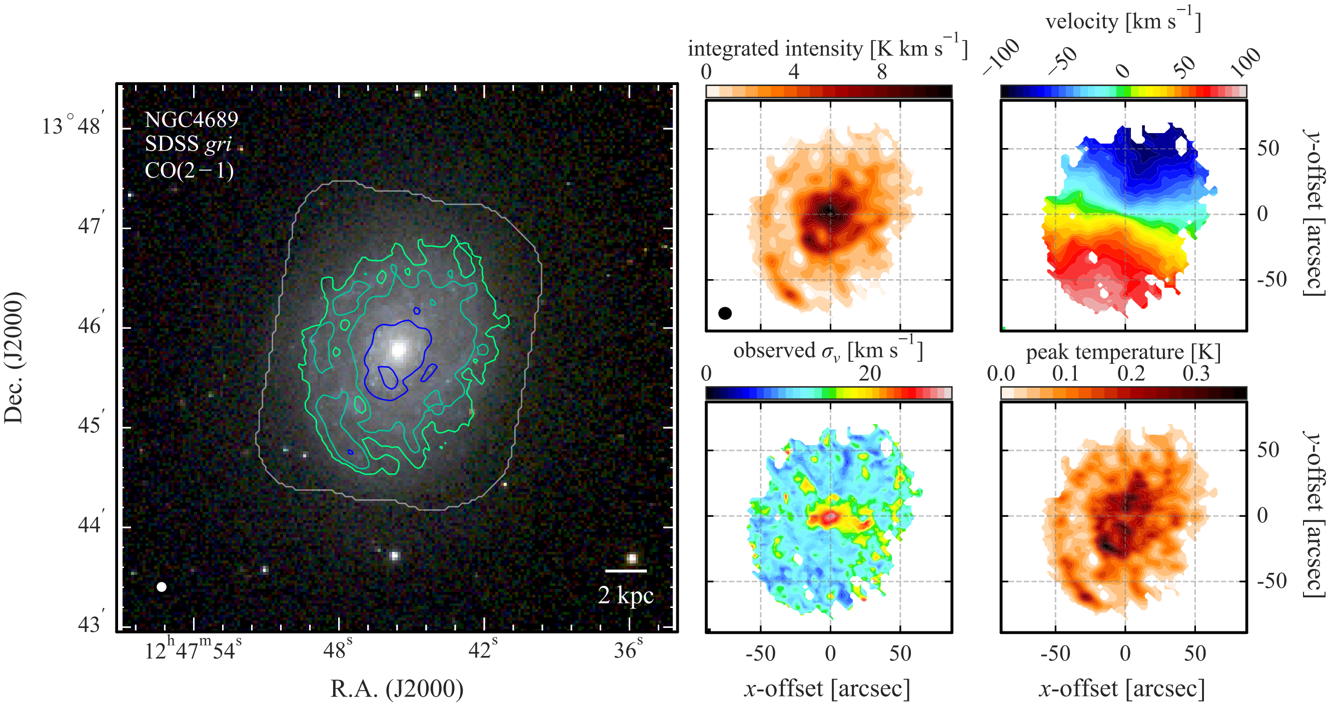

Figure 4.22. As in Figure 4.1.

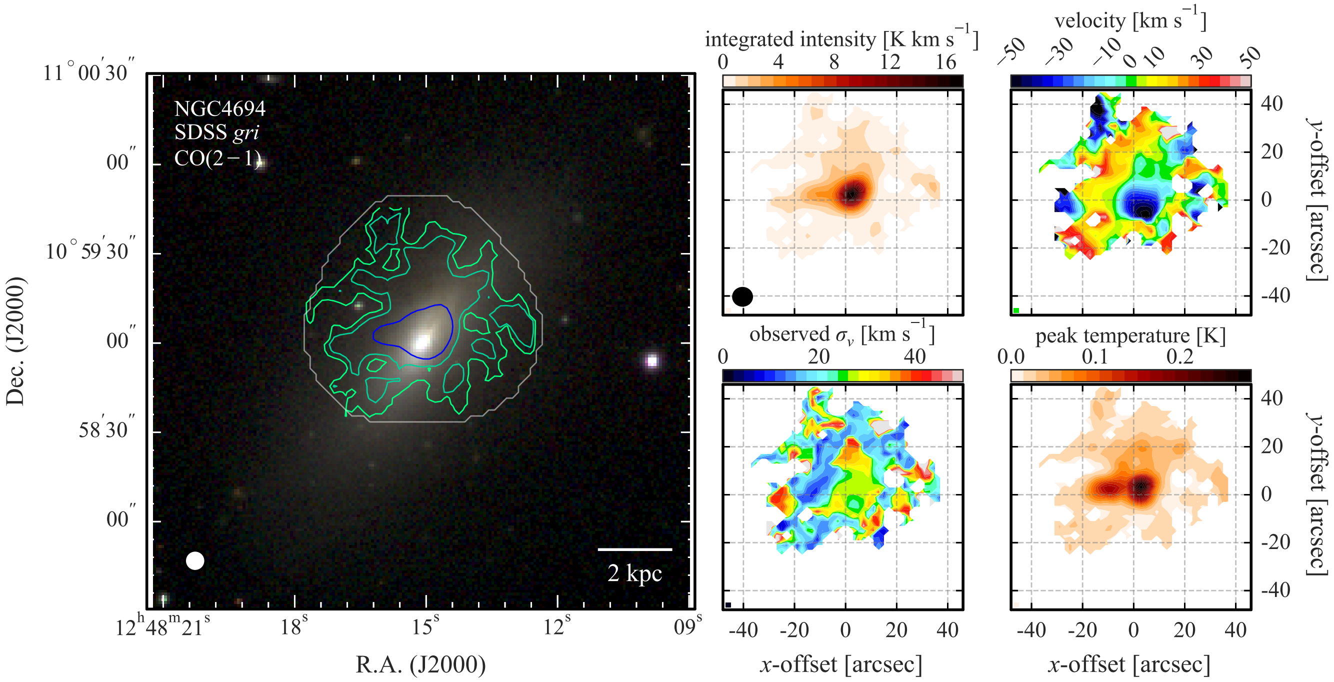

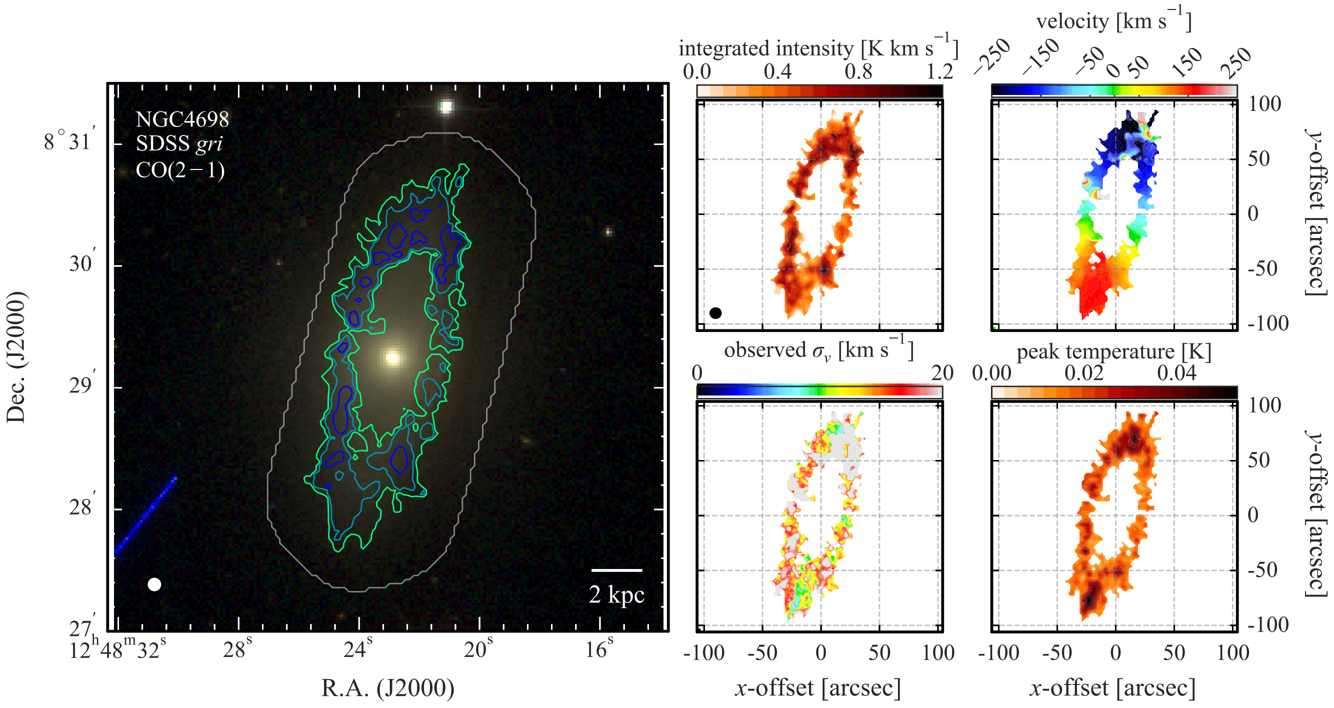

Figure 4.23. As in Figure 4.1.

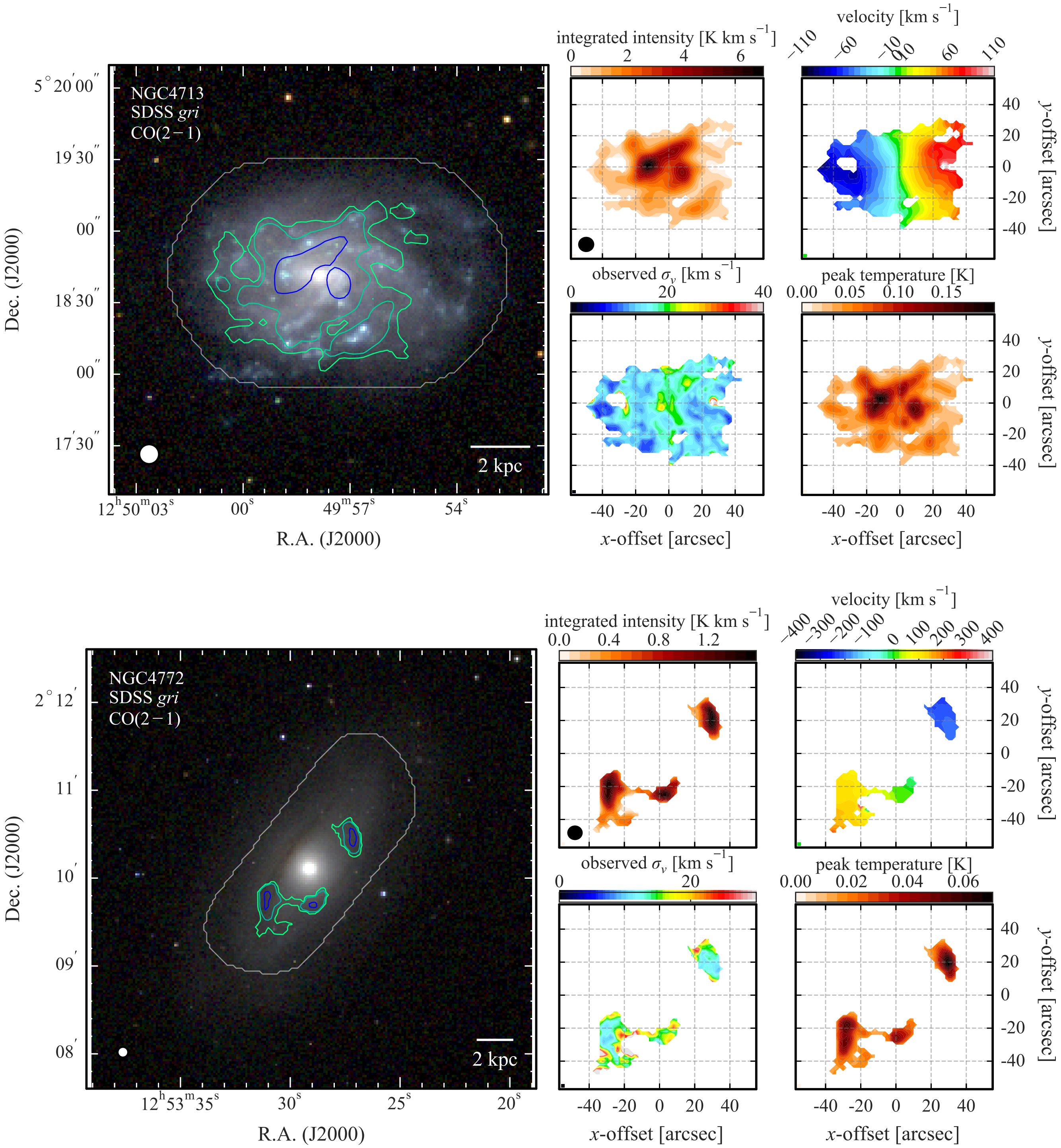

Figure 4.24. As in Figure 4.1.

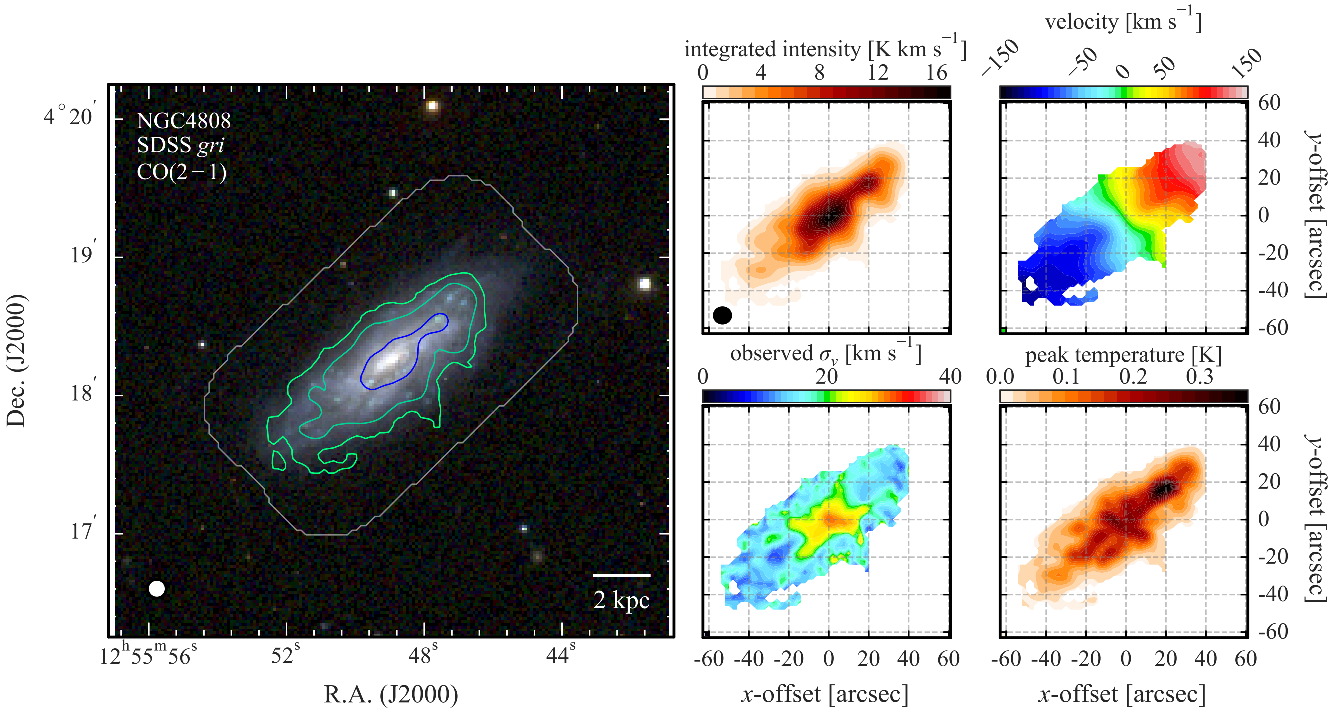

Figure 4.25. As in Figure 4.1.

Astropy Collaboration, Robitaille, T. P., Tollerud, E. J., et al. 2013, A&A, 558, A33, doi: 10.1051/0004-6361/201322068

Balogh, M. L., Morris, S. L., Yee, H. K. C., Carlberg, R. G., & Ellingson, E. 1999, ApJ, 527, 54, doi: 10.1086/308056

Balogh, M. L., Navarro, J. F., & Morris, S. L. 2000, ApJ, 540, 113, doi: 10.1086/309323

Balogh, M. L., Schade, D., Morris, S. L., et al. 1998, ApJL, 504, L75, doi: 10.1086/311576

Bekki, K., Couch, W. J., & Shioya, Y. 2002, ApJ, 577, 651, doi: 10.1086/342221

Bigiel, F., & Blitz, L. 2012, ApJ, 756, 183, doi: 10.1088/0004-637X/756/2/183

Böhringer, H., Briel, U. G., Schwarz, R. A., et al. 1994, Nature, 368, 828, doi: 10.1038/368828a0

Bolatto, A. D., Wolfire, M., & Leroy, A. K. 2013, ARA&A, 51, 207, doi: 10.1146/annurev-astro-082812-140944

Bolatto, A. D., Wong, T., Utomo, D., et al. 2017, ApJ, 846, 159, doi: 10.3847/1538-4357/aa86aa

Boselli, A., Cortese, L., & Boquien, M. 2014, A&A, 564, A65, doi: 10.1051/0004-6361/201322311

Boselli, A., & Gavazzi, G. 2006, PASP, 118, 517, doi: 10.1086/500691

Boselli, A., Gavazzi, G., Lequeux, J., et al. 1997, A&A, 327, 522

Boselli, A., Lequeux, J., & Gavazzi, G. 2002, A&A, 384, 33, doi: 10.1051/0004-6361:20011747

Boselli, A., Eales, S., Cortese, L., et al. 2010, PASP, 122, 261, doi: 10.1086/651535

Boselli, A., Boissier, S., Heinis, S., et al. 2011, A&A, 528, A107, doi: 10.1051/0004-6361/201016389

Boselli, A., Fossati, M., Ferrarese, L., et al. 2018, A&A, 614, A56, doi: 10.1051/0004-6361/201732407

Bradley, L., Sipőcz, B., Robitaille, T., et al. 2020, astropy/photutils: 1.0.0, 1.0.0, Zenodo, doi: 10.5281/zenodo.4044744

Briggs, D. S. 1995, in Bulletin of the American Astronomical Society, Vol. 27, American Astronomical Society Meeting Abstracts, 1444

Brown, T., Catinella, B., Cortese, L., et al. 2017, MNRAS, 466, 1275, doi: 10.1093/mnras/stw2991

Cappellari, M., Scott, N., Alatalo, K., et al. 2013, MNRAS, 432, 1709, doi: 10.1093/mnras/stt562

Catinella, B., Saintonge, A., Janowiecki, S., et al. 2018, MNRAS, 476, 875, doi: 10.1093/mnras/sty089

Chabrier, G. 2003, PASP, 115, 763, doi: 10.1086/376392

Chamaraux, P., Balkowski, C., & Gerard, E. 1980, A&A, 83, 38

Chown, R., Li, C., Athanassoula, E., et al. 2019, MNRAS, 484, 5192, doi: 10.1093/mnras/stz349

Chung, A., van Gorkom, J. H., Kenney, J. D. P., Crowl, H., & Vollmer, B. 2009a, AJ, 138, 1741, doi: 10.1088/0004-6256/138/6/1741

Chung, E. J., Rhee, M.-H., Kim, H., et al. 2009b, ApJS, 184, 199, doi: 10.1088/0067-0049/184/2/199

Chung, E. J., Yun, M. S., Verheijen, M. A. W., & Chung, A. 2017, ApJ, 843, 50, doi: 10.3847/1538-4357/aa756b

Ciesla, L., Boselli, A., Smith, M. W. L., et al. 2012, A&A, 543, A161, doi: 10.1051/0004-6361/201219216

Clark, C. J. R., Verstocken, S., Bianchi, S., et al. 2018, A&A, 609, A37, doi: 10.1051/0004-6361/201731419

Comrie, A., Wang, K.-S., Ford, P., et al. 2020, CARTA: The Cube Analysis and Rendering Tool for Astronomy, 1.3.0, Zenodo, doi: 10.5281/zenodo.3746095

Corbelli, E., Bianchi, S., Cortese, L., et al. 2012, A&A, 542, A32, doi: 10.1051/0004-6361/201117329

Cortese, L., Catinella, B., Boissier, S., Boselli, A., & Heinis, S. 2011, MNRAS, 415, 1797, doi: 10.1111/j.1365-2966.2011.18822.x

Cortese, L., Catinella, B., & Smith, R. 2021, arXiv e-prints, arXiv:2104.02193. https://arxiv.org/abs/2104.02193

Cortese, L., Boissier, S., Boselli, A., et al. 2012, A&A, 544, A101, doi: 10.1051/0004-6361/201219312

Cowie, L. L., & Songaila, A. 1977, Nature, 266, 501, doi: 10.1038/266501a0

Cramer, W. J., Kenney, J. D. P., Cortes, J. R., et al. 2020, ApJ, 901, 95, doi: 10.3847/1538-4357/abaf54

Cramer, W. J., Kenney, J. D. P., Sun, M., et al. 2019, ApJ, 870, 63, doi: 10.3847/1538-4357/aaefff

Davies, J. I., Baes, M., Bendo, G. J., et al. 2010, A&A, 518, L48, doi: 10.1051/0004-6361/201014571

Davies, R. D., & Lewis, B. M. 1973, MNRAS, 165, 231, doi: 10.1093/mnras/165.2.231

Davis, T. A., Alatalo, K., Bureau, M., et al. 2013, MNRAS, 429, 534, doi: 10.1093/mnras/sts353

den Brok, J. S., Chatzigiannakis, D., Bigiel, F., et al. 2021, MNRAS, 504, 3221, doi: 10.1093/mnras/stab859

Ebeling, H., Stephenson, L. N., & Edge, A. C. 2014, ApJL, 781, L40, doi: 10.1088/2041-8205/781/2/L40

Ebeling, H., White, D. A., & Rangarajan, F. V. N. 2006, MNRAS, 368, 65, doi: 10.1111/j.1365-2966.2006.10135.x

Elbaz, D., Daddi, E., Le Borgne, D., et al. 2007, A&A, 468, 33, doi: 10.1051/0004-6361:20077525

Ferrarese, L., Côté, P., Cuillandre, J.-C., et al. 2012, ApJS, 200, 4, doi: 10.1088/0067-0049/200/1/4

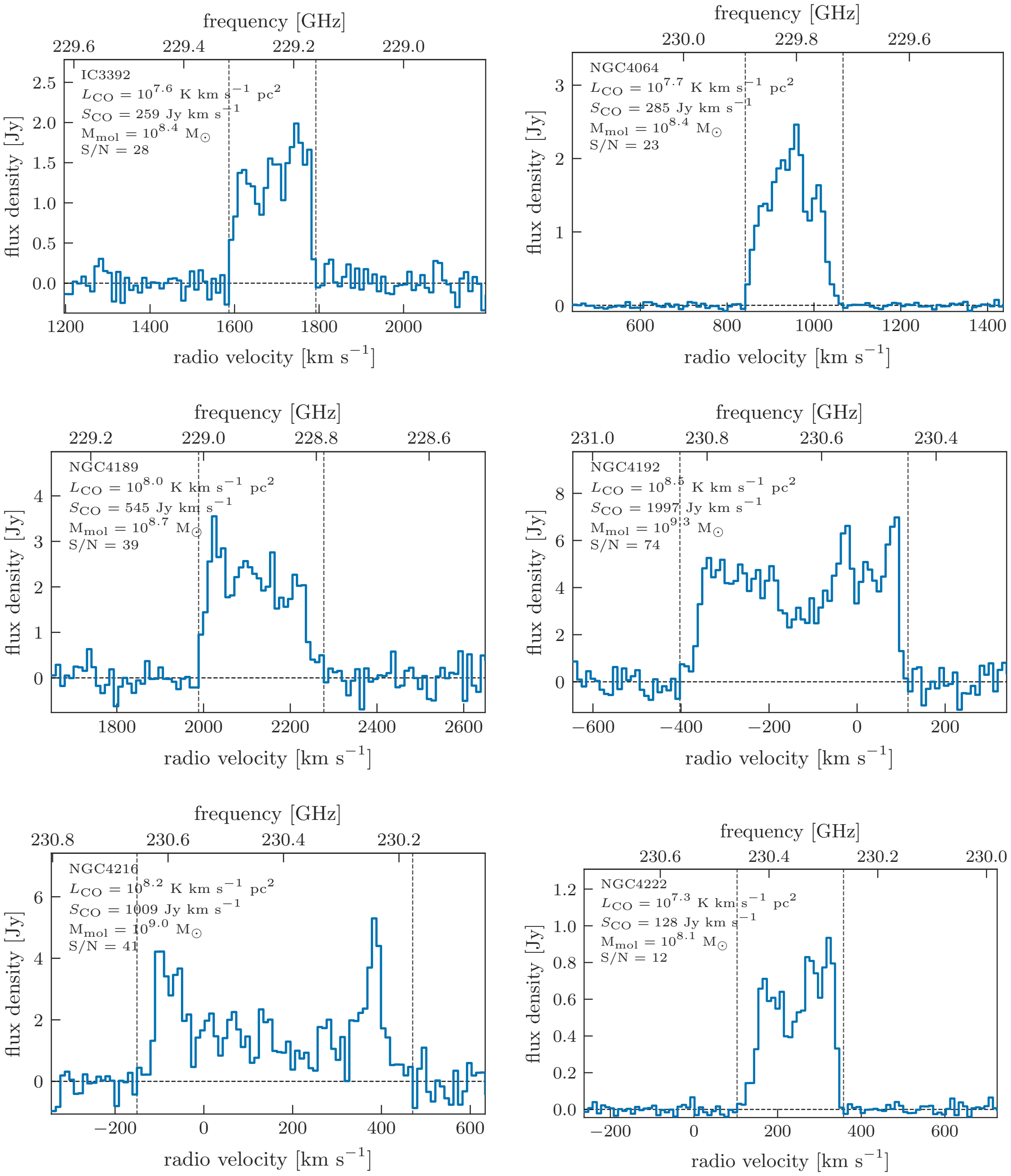

Figure 13. ^{12}CO$(2-1)$ spectra at 10.6 km s^{-1} resolution. The velocity limits used to estimate the velocity width and flux density for each galaxy are shown by the dashed vertical lines. The galaxy name, integrated CO line luminosity (Eqn. 5), integrated flux density, molecular gas mass (Eqn. 7), and signal-to-noise of the spectrum are shown in the upper left corner of each panel. *The complete Figure Set containing 51* ^{12}*CO*$(2-1)$ *spectra for all VERTICO galaxies is available in below.*

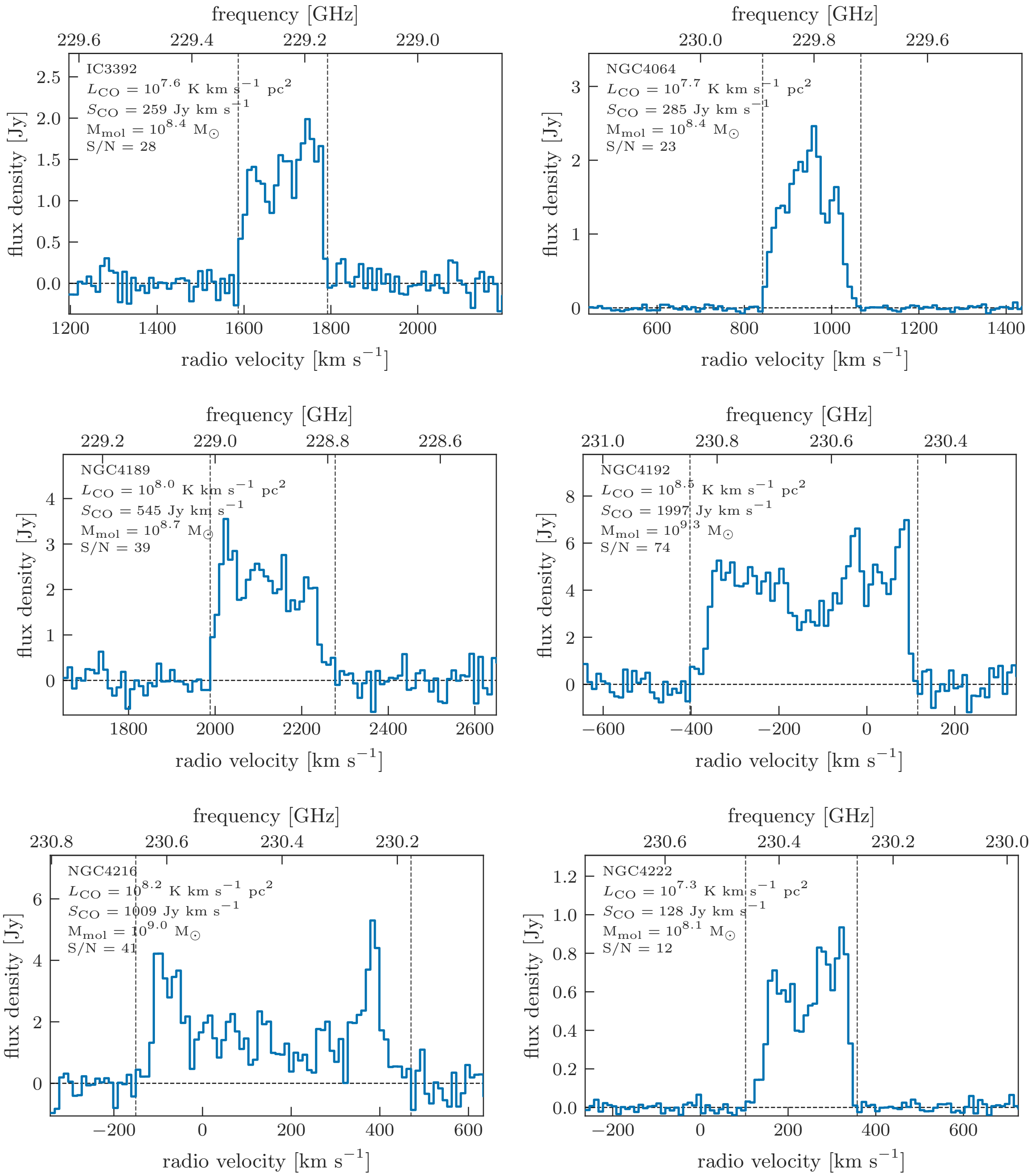

Figure 13.1. As in Figure 13.1.

Fruscione, A., McDowell, J. C., Allen, G. E., et al. 2006, in Society of Photo-Optical Instrumentation Engineers (SPIE) Conference Series, Vol. 6270, Society of Photo-Optical Instrumentation Engineers (SPIE) Conference Series, ed. D. R. Silva & R. E. Doxsey, 62701V, doi: 10.1117/12.671760

Fujita, Y. 1998, ApJ, 509, 587, doi: 10.1086/306518

Fumagalli, M., Fossati, M., Hau, G. K. T., et al. 2014, MNRAS, 445, 4335, doi: 10.1093/mnras/stu2092

Fumagalli, M., Gavazzi, G., Scaramella, R., & Franzetti, P. 2011, A&A, 528, A46, doi: 10.1051/0004-6361/201015463

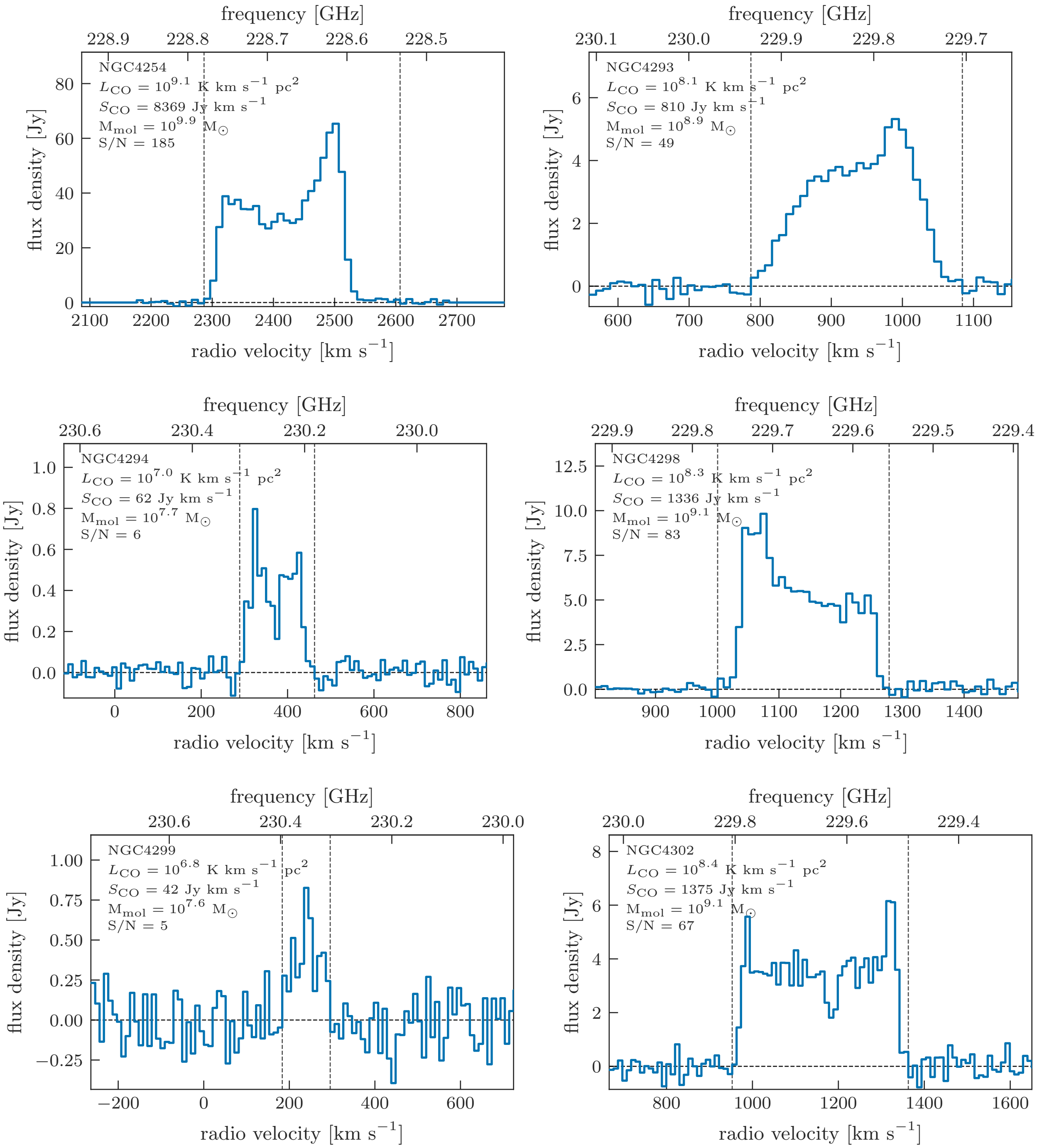

Figure 13.2. As Figure 13.1.

Gaudet, S., Hill, N., Armstrong, P., et al. 2010, in Society of Photo-Optical Instrumentation Engineers (SPIE) Conference Series, Vol. 7740, Software and Cyberinfrastructure for Astronomy, ed. N. M. Radziwill & A. Bridger, 77401I, doi: 10.1117/12.858026

Gavazzi, G., Boselli, A., Scodeggio, M., Pierini, D., & Belsole, E. 1999, MNRAS, 304, 595, doi: 10.1046/j.1365-8711.1999.02350.x

Gavazzi, G., Giovanelli, R., Haynes, M. P., et al. 2008, A&A, 482, 43, doi: 10.1051/0004-6361:200809382

Giovanelli, R., & Haynes, M. P. 1985, ApJ, 292, 404, doi: 10.1086/163170

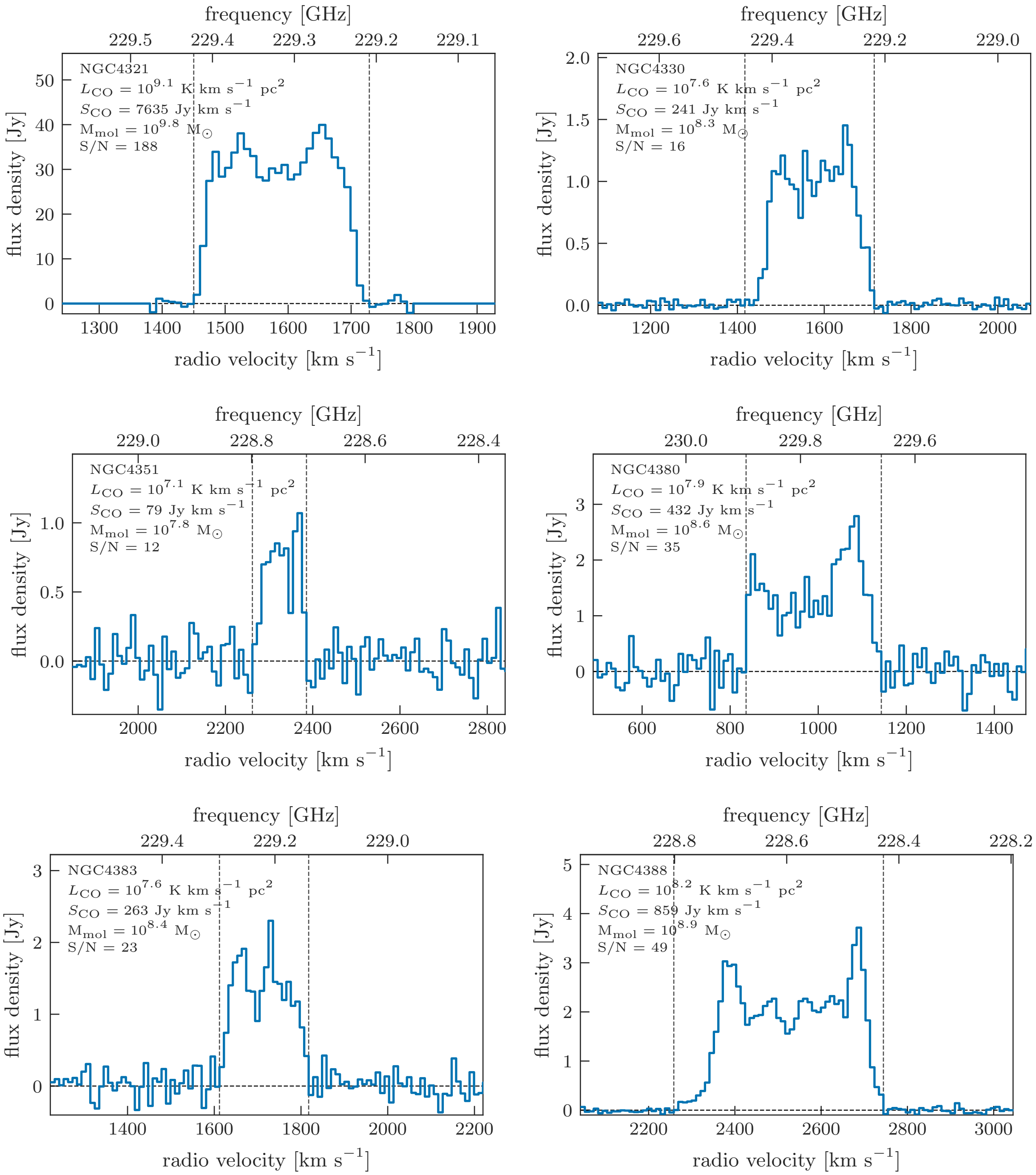

Figure 13.3. As Figure 13.1.

Girardi, M., Giuricin, G., Mardirossian, F., Mezzetti, M., & Boschin, W. 1998, ApJ, 505, 74, doi: 10.1086/306157

Gómez, P. L., Nichol, R. C., Miller, C. J., et al. 2003, ApJ, 584, 210, doi: 10.1086/345593

Gunn, J. E., & Gott, J. Richard, I. 1972, ApJ, 176, 1, doi: 10.1086/151605

Haynes, M. P., Giovanelli, R., & Chincarini, G. L. 1984, ARA&A, 22, 445, doi: 10.1146/annurev.aa.22.090184.002305

Healy, J., Blyth, S.-L., Verheijen, M. A. W., et al. 2020, arXiv e-prints, arXiv:2011.06285. https://arxiv.org/abs/2011.06285

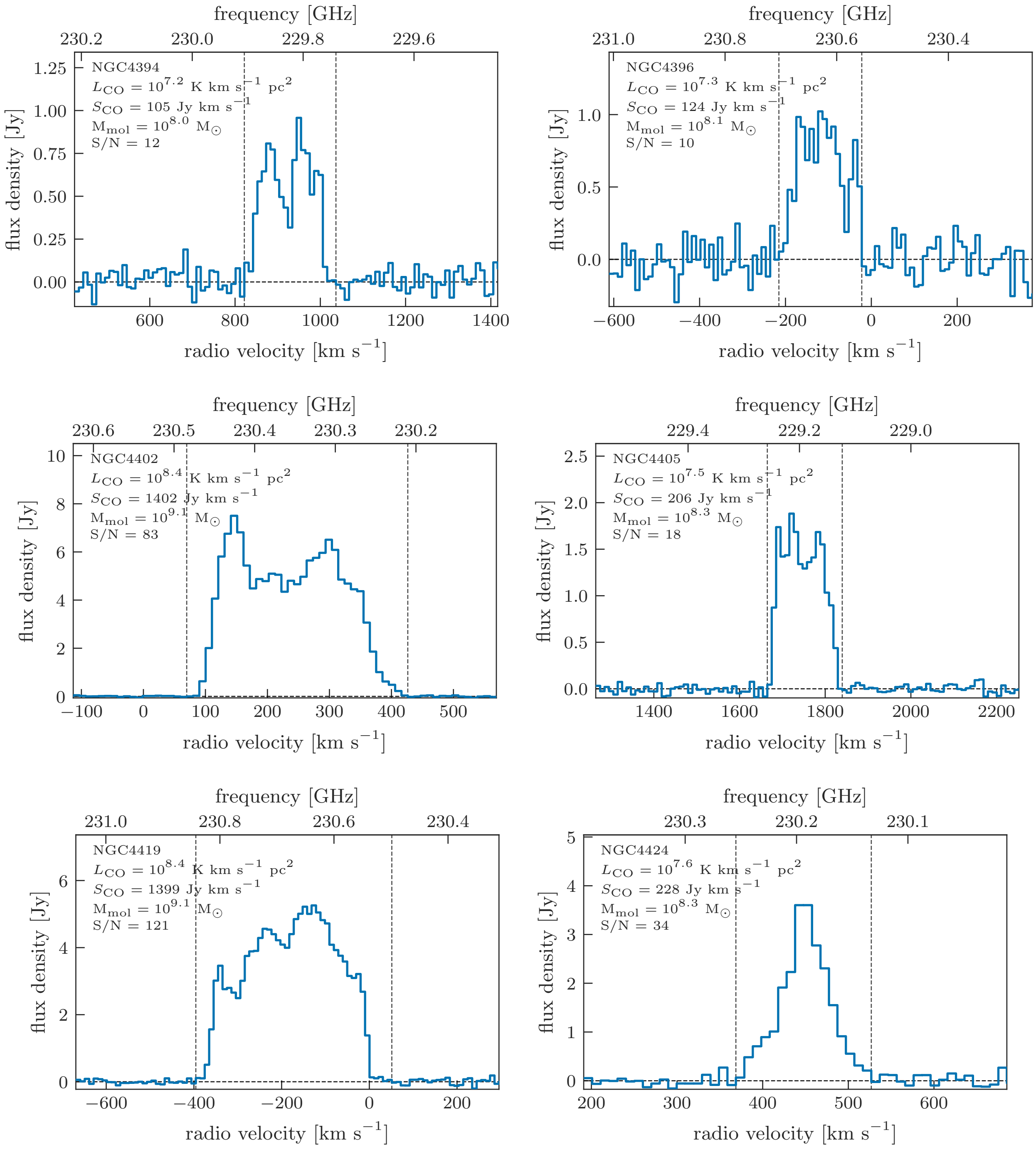

Figure 13.4. As Figure 13.1.

Helfer, T. T., Thornley, M. D., Regan, M. W., et al. 2003, ApJS, 145, 259, doi: 10.1086/346076

Herrera, C. N., Pety, J., Hughes, A., et al. 2020, A&A, 634, A121, doi: 10.1051/0004-6361/201936060

Hester, J. A. 2006, ApJ, 647, 910, doi: 10.1086/505614

Heyer, M., & Dame, T. M. 2015, ARA&A, 53, 583, doi: 10.1146/annurev-astro-082214-122324

Hughes, T. M., & Cortese, L. 2009, MNRAS, 396, L41, doi: 10.1111/j.1745-3933.2009.00658.x

Hunter, J. D. 2007, Computing in Science & Engineering, 9, 90, doi: 10.1109/MCSE.2007.55

Iono, D., Yun, M. S., & Ho, P. T. P. 2005, ApJS, 158, 1, doi: 10.1086/429093

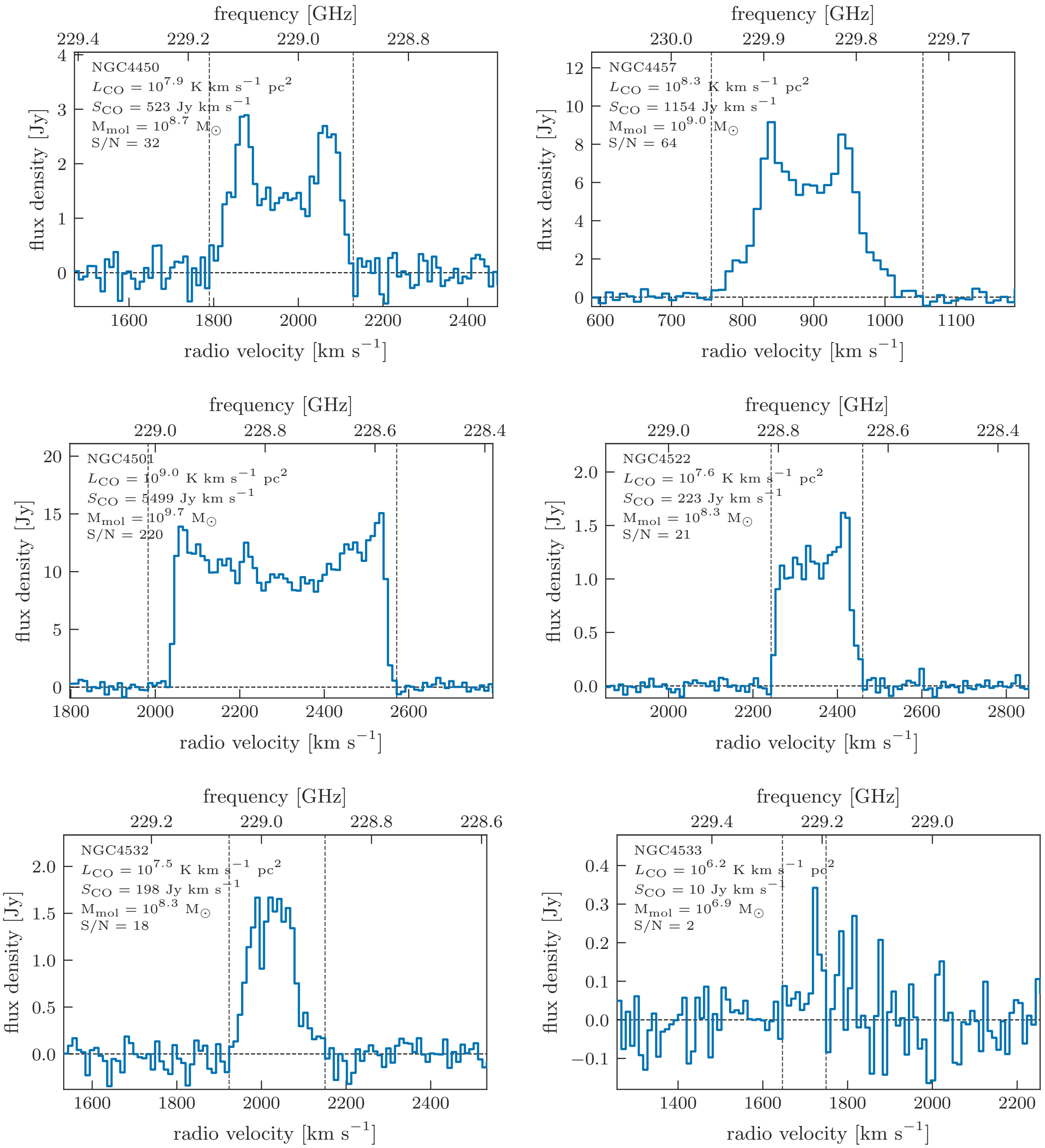

Figure 13.5. As Figure 13.1.

Jáchym, P., Kenney, J. D. P., Ržuička, A., et al. 2013, A&A, 556, A99, doi: 10.1051/0004-6361/201220495

Jáchym, P., Kenney, J. D. P., Sun, M., et al. 2019, ApJ, 883, 145, doi: 10.3847/1538-4357/ab3e6c

Jaffé, Y. L., Verheijen, M. A. W., Haines, C. P., et al. 2016, MNRAS, 461, 1202, doi: 10.1093/mnras/stw984

Kaiser, N. 1986, MNRAS, 222, 323, doi: 10.1093/mnras/222.2.323

Kaneko, H., Kuno, N., & Saitoh, T. R. 2018, ApJL, 860, L14, doi: 10.3847/2041-8213/aac895

Karachentsev, I. D., Tully, R. B., Wu, P.-F., Shaya, E. J., & Dolphin, A. E. 2014, ApJ, 782, 4, doi: 10.1088/0004-637X/782/1/4

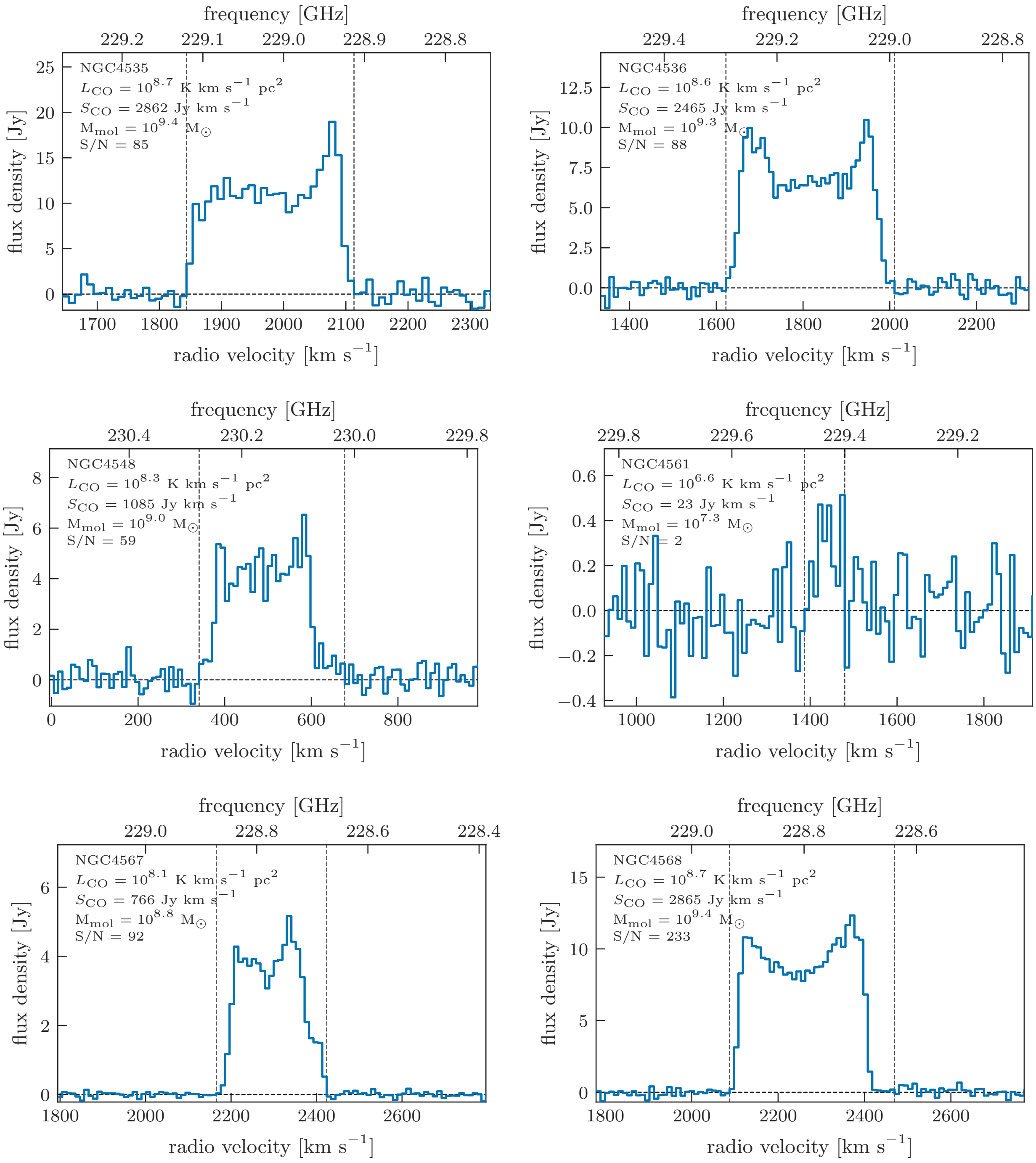

Figure 13.6. As Figure 13.1.

Kenney, J. D., & Young, J. S. 1986, ApJL, 301, L13, doi: 10.1086/184614

Kenney, J. D. P., Wilson, C. D., Scoville, N. Z., Devereux, N. A., & Young, J. S. 1992, ApJL, 395, L79, doi: 10.1086/186492

Kenney, J. D. P., & Young, J. S. 1989, ApJ, 344, 171, doi: 10.1086/167787

Kennicutt, R. C., & Evans, N. J. 2012, ARA&A, 50, 531, doi: 10.1146/annurev-astro-081811-125610

Kim, S., Rey, S.-C., Jerjen, H., et al. 2014, ApJS, 215, 22, doi: 10.1088/0067-0049/215/2/22

Koopmann, R. A., & Kenney, J. D. P. 2004, ApJ, 613, 866, doi: 10.1086/423191

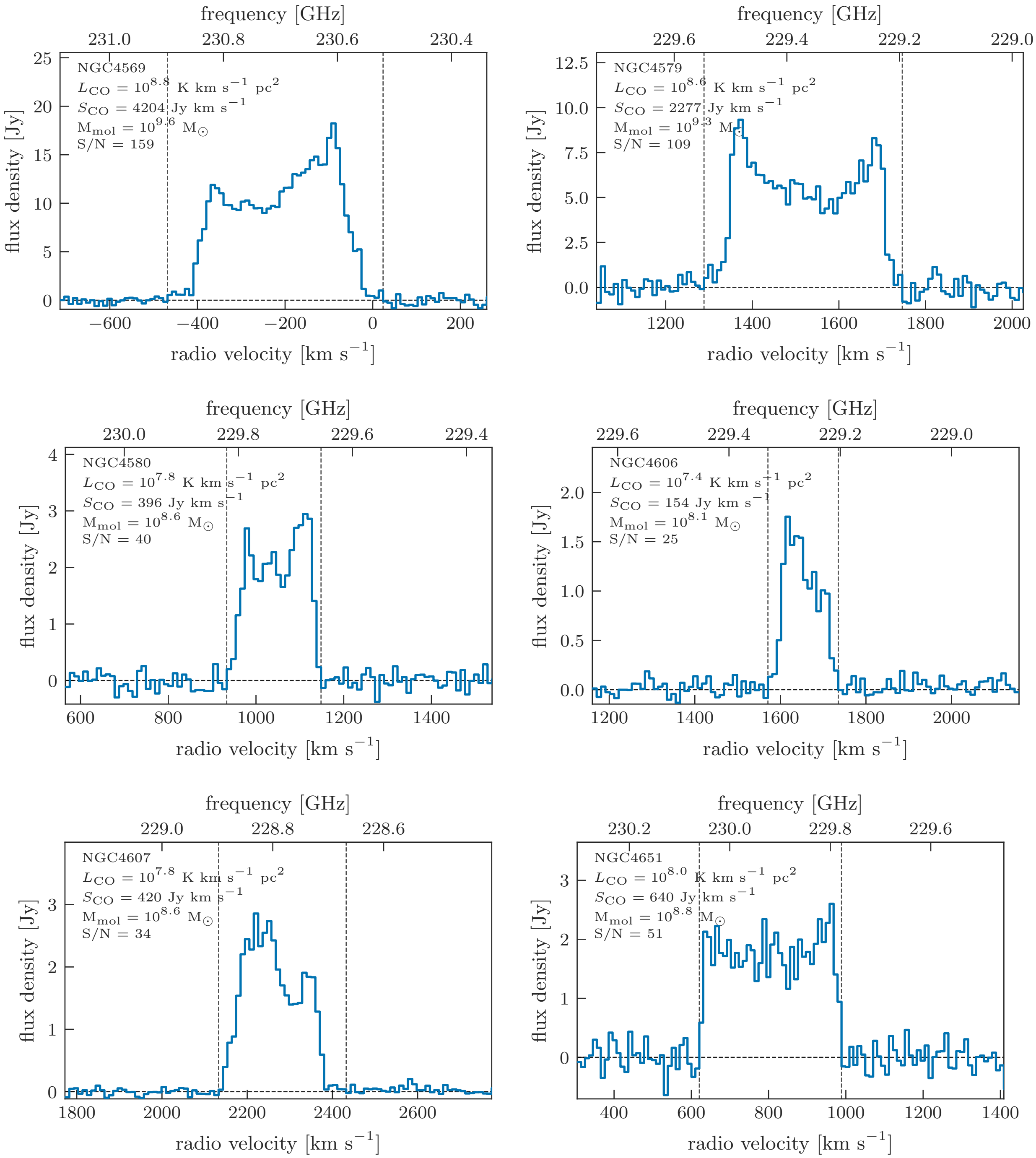

Figure 13.7. As Figure 13.1.

Koopmann, R. A., Kenney, J. D. P., & Young, J. 2001, ApJS, 135, 125, doi: 10.1086/323532

Koyama, S., Koyama, Y., Yamashita, T., et al. 2017, ApJ, 847, 137, doi: 10.3847/1538-4357/aa8a6c

Kroupa, P. 2001, MNRAS, 322, 231, doi: 10.1046/j.1365-8711.2001.04022.x

Krumholz, M. R., McKee, C. F., & Tumlinson, J. 2009, ApJ, 693, 216, doi: 10.1088/0004-637X/693/1/216

Kutner, M. L., & Ulich, B. L. 1981, ApJ, 250, 341, doi: 10.1086/159380

Larson, R. B., Tinsley, B. M., & Caldwell, C. N. 1980, ApJ, 237, 692, doi: 10.1086/157917

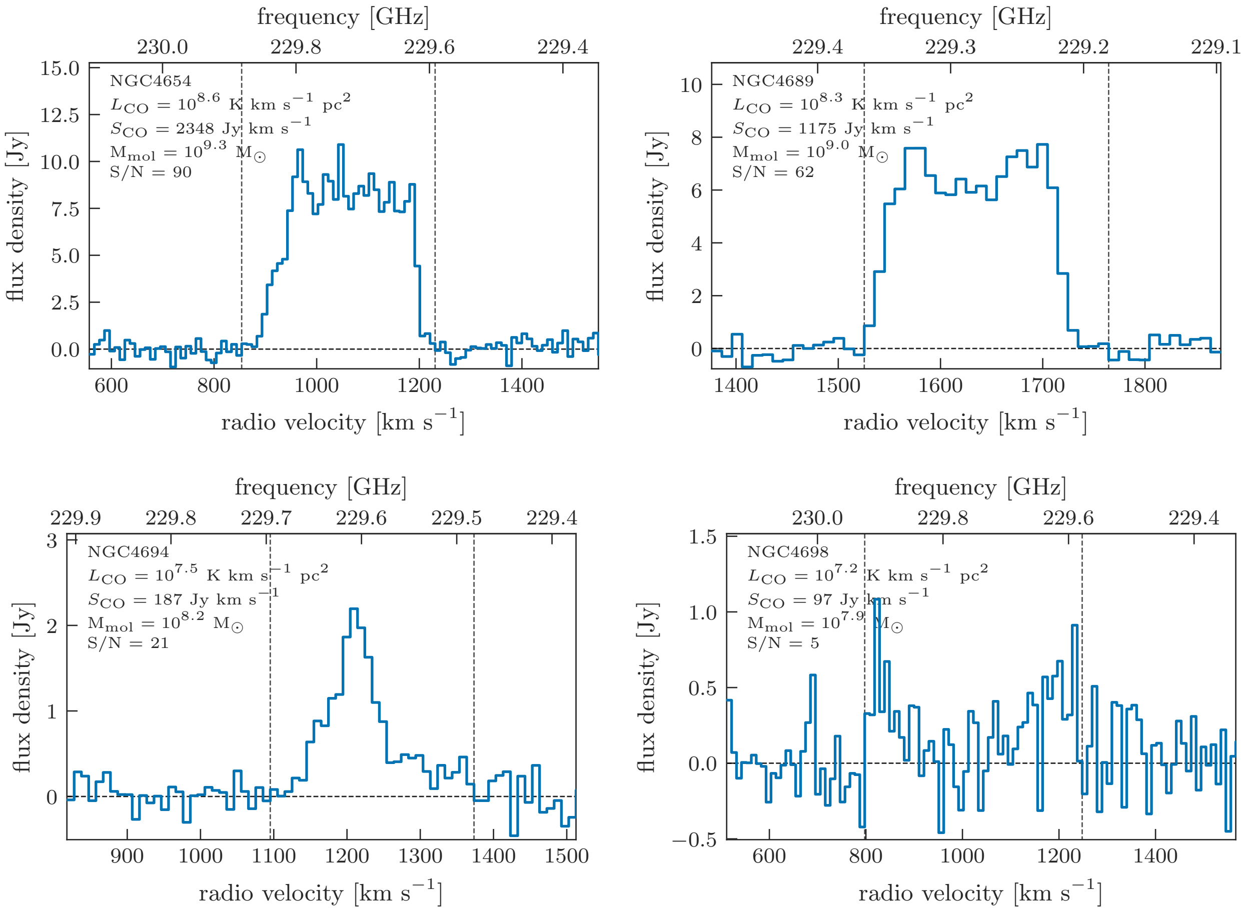

Figure 13.8. As Figure 13.1.

Lee, B., & Chung, A. 2018, ApJL, 866, L10, doi: 10.3847/2041-8213/aae4d9

Lee, B., Chung, A., Tonnesen, S., et al. 2017, MNRAS, 466, 1382, doi: 10.1093/mnras/stw3162

Leroy, A. K., Walter, F., Brinks, E., et al. 2008, AJ, 136, 2782, doi: 10.1088/0004-6256/136/6/2782

Leroy, A. K., Walter, F., Bigiel, F., et al. 2009, AJ, 137, 4670, doi: 10.1088/0004-6256/137/6/4670

Leroy, A. K., Bolatto, A., Gordon, K., et al. 2011, ApJ, 737, 12, doi: 10.1088/0004-637X/737/1/12

Leroy, A. K., Walter, F., Sandstrom, K., et al. 2013, AJ, 146, 19, doi: 10.1088/0004-6256/146/2/19

Leroy, A. K., Sandstrom, K. M., Lang, D., et al. 2019, ApJS, 244, 24, doi: 10.3847/1538-4365/ab3925

Leroy, A. K., Schinnerer, E., Hughes, A., et al. 2021a, arXiv e-prints, arXiv:2104.07739. https://arxiv.org/abs/2104.07739

Leroy, A. K., Hughes, A., Liu, D., et al. 2021b, arXiv e-prints, arXiv:2104.07665. https://arxiv.org/abs/2104.07665

Lin, L., Li, C., He, Y., Xiao, T., & Wang, E. 2017, ApJ, 838, 105, doi: 10.3847/1538-4357/aa657a

Lin, L., Li, C., Du, C., et al. 2020, MNRAS, 499, 1406, doi: 10.1093/mnras/staa2913

Livio, M., Regev, O., & Shaviv, G. 1980, ApJL, 240, L83, doi: 10.1086/183328

Lizée, T., Vollmer, B., Braine, J., & Nehlig, F. 2021, A&A, 645, A111, doi: 10.1051/0004-6361/202038910

Martin, D. C., Fanson, J., Schiminovich, D., et al. 2005, ApJL, 619, L1, doi: 10.1086/426387

McLaughlin, D. E. 1999, ApJL, 512, L9, doi: 10.1086/311860

McMullin, J. P., Waters, B., Schiebel, D., Young, W., & Golap, K. 2007, in Astronomical Society of the Pacific Conference Series, Vol. 376, Astronomical Data Analysis Software and Systems XVI, ed. R. A. Shaw, F. Hill, & D. J. Bell, 127

Mei, S., Blakeslee, J. P., Côté, P., et al. 2007, ApJ, 655, 144, doi: 10.1086/509598

Mok, A., Wilson, C. D., Knapen, J. H., et al. 2017, MNRAS, 467, 4282, doi: 10.1093/mnras/stx345

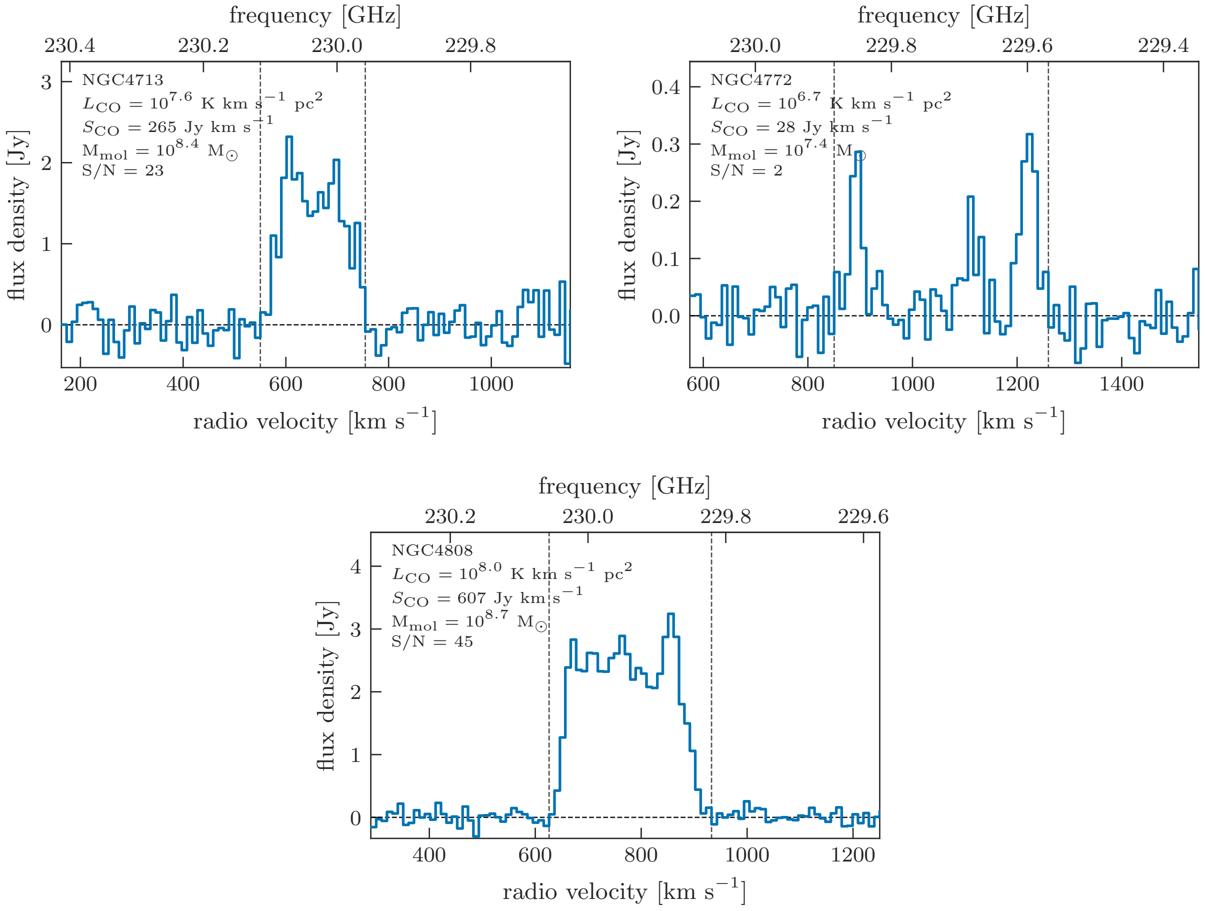

Figure 13.9. As Figure 13.1.

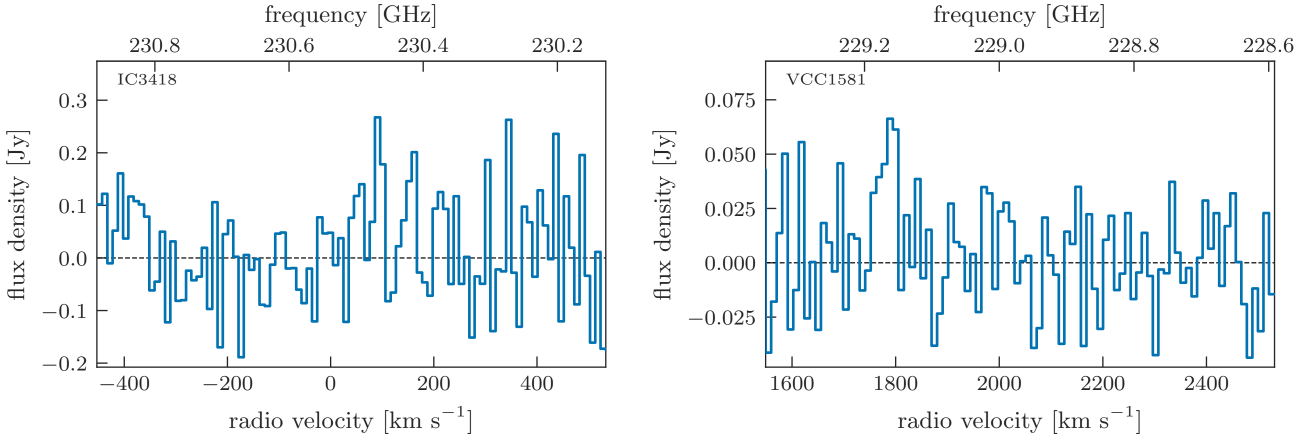

Figure 13.10. Spectra covering the expected frequency of ^{12}CO(2 − 1) calculated from the velocity listed in Table 1 for the two VERTICO non-detections, IC3418 and VCC1581. The velocity resolution is 10.6 km s^{-1}.

Mok, A., Wilson, C. D., Golding, J., et al. 2016, MNRAS, 456, 4384, doi: 10.1093/mnras/stv2958

Moore, B., Katz, N., Lake, G., Dressler, A., & Oemler, A. 1996, Nature, 379, 613, doi: 10.1038/379613a0

Moore, B., Lake, G., & Katz, N. 1998, ApJ, 495, 139, doi: 10.1086/305264

Moore, B., Lake, G., Quinn, T., & Stadel, J. 1999, MNRAS, 304, 465, doi: 10.1046/j.1365-8711.1999.02345.x

Moretti, A., Paladino, R., Poggianti, B. M., et al. 2018, MNRAS, 480, 2508, doi: 10.1093/mnras/sty2021

—. 2020a, ApJ, 889, 9, doi: 10.3847/1538-4357/ab616a

—. 2020b, ApJL, 897, L30, doi: 10.3847/2041-8213/ab9f3b

Morokuma-Matsui, K., Kodama, T., Morokuma, T., et al. 2021, arXiv e-prints, arXiv:2103.05867. https://arxiv.org/abs/2103.05867

Muñoz-Mateos, J. C., Gil de Paz, A., Zamorano, J., et al. 2009, ApJ, 703, 1569, doi: 10.1088/0004-637X/703/2/1569

Mun, J. Y., Hwang, H. S., Lee, M. G., et al. 2021, Journal of Korean Astronomical Society, 54, 17, doi: 10.5303/JKAS.2021.54.1.17

Muraoka, K., Sorai, K., Kuno, N., et al. 2016, PASJ, 68, 89, doi: 10.1093/pasj/psw080

Narayanan, D., Krumholz, M., Ostriker, E. C., & Hernquist, L. 2011, MNRAS, 418, 664, doi: 10.1111/j.1365-2966.2011.19516.x

Narayanan, D., Krumholz, M. R., Ostriker, E. C., & Hernquist, L. 2012, MNRAS, 421, 3127, doi: 10.1111/j.1365-2966.2012.20536.x

Nehlig, F., Vollmer, B., & Braine, J. 2016, A&A, 587, A108, doi: 10.1051/0004-6361/201527021

Nulsen, P. E. J. 1982, MNRAS, 198, 1007, doi: 10.1093/mnras/198.4.1007

Nulsen, P. E. J., & Bohringer, H. 1995, MNRAS, 274, 1093, doi: 10.1093/mnras/274.4.1093

Olsen, K. P., Greve, T. R., Brinch, C., et al. 2016, MNRAS, 457, 3306, doi: 10.1093/mnras/stw162

Pappalardo, C., Bianchi, S., Corbelli, E., et al. 2012, A&A, 545, A75, doi: 10.1051/0004-6361/201219689

Poggianti, B. M., Jaffé, Y. L., Moretti, A., et al. 2017, Nature, 548, 304, doi: 10.1038/nature23462

Price-Whelan, A. M., Sipőcz, B. M., Günther, H. M., et al. 2018, AJ, 156, 123, doi: 10.3847/1538-3881/aabc4f

Regan, M. W., Thornley, M. D., Helfer, T. T., et al. 2001, ApJ, 561, 218, doi: 10.1086/323221

Saintonge, A., & Spekkens, K. 2011, ApJ, 726, 77, doi: 10.1088/0004-637X/726/2/77

Saintonge, A., Kauffmann, G., Kramer, C., et al. 2011, MNRAS, 415, 32, doi: 10.1111/j.1365-2966.2011.18677.x

Saintonge, A., Catinella, B., Tacconi, L. J., et al. 2017, ApJS, 233, 22, doi: 10.3847/1538-4365/aa97e0

Salim, S., Rich, R. M., Charlot, S., et al. 2007, ApJS, 173, 267, doi: 10.1086/519218

Salpeter, E. E. 1955, ApJ, 121, 161, doi: 10.1086/145971

Sánchez Almeida, J. 2020, MNRAS, 495, 78, doi: 10.1093/mnras/staa1108

Sandstrom, K. M., Leroy, A. K., Walter, F., et al. 2013, ApJ, 777, 5, doi: 10.1088/0004-637X/777/1/5

Schindler, S., Binggeli, B., & Böhringer, H. 1999, A&A, 343, 420. https://arxiv.org/abs/astro-ph/9811464

Schruba, A., Leroy, A. K., Walter, F., et al. 2011, AJ, 142, 37, doi: 10.1088/0004-6256/142/2/37

Sheth, K., Vogel, S. N., Regan, M. W., Thornley, M. D., & Teuben, P. J. 2005, ApJ, 632, 217, doi: 10.1086/432409

Shetty, R., Glover, S. C., Dullemond, C. P., et al. 2011, MNRAS, 415, 3253, doi: 10.1111/j.1365-2966.2011.18937.x

Shibata, R., Matsushita, K., Yamasaki, N. Y., et al. 2001, ApJ, 549, 228, doi: 10.1086/319075

Smith, M. W. L., Eales, S. A., Gomez, H. L., et al. 2012, ApJ, 756, 40, doi: 10.1088/0004-637X/756/1/40

Solomon, P. M., & Vanden Bout, P. A. 2005, ARA&A, 43, 677, doi: 10.1146/annurev.astro.43.051804.102221

Sorce, J. G., Gottlöber, S., Hoffman, Y., & Yepes, G. 2016, MNRAS, 460, 2015, doi: 10.1093/mnras/stw1085

Speagle, J. S., Steinhardt, C. L., Capak, P. L., & Silverman, J. D. 2014, ApJS, 214, 15, doi: 10.1088/0067-0049/214/2/15

Stark, A. A., Knapp, G. R., Bally, J., et al. 1986, ApJ, 310, 660, doi: 10.1086/164717

Stevens, A. R. H., Diemer, B., Lagos, C. d. P., et al. 2019, MNRAS, 490, 96, doi: 10.1093/mnras/stz2513

Stevens, A. R. H., Lagos, C. d. P., Cortese, L., et al. 2021, MNRAS, 502, 3158, doi: 10.1093/mnras/staa3662

Sun, J., Leroy, A. K., Schruba, A., et al. 2018, ApJ, 860, 172, doi: 10.3847/1538-4357/aac326

Trujillo, I., Chamba, N., & Knapen, J. H. 2020, MNRAS, 493, 87, doi: 10.1093/mnras/staa236

Tully, R. B., & Shaya, E. J. 1984, ApJ, 281, 31, doi: 10.1086/162073

Urban, O., Werner, N., Simionescu, A., Allen, S. W., & Böhringer, H. 2011, MNRAS, 414, 2101, doi: 10.1111/j.1365-2966.2011.18526.x

Virtanen, P., Gommers, R., Oliphant, T. E., et al. 2020, Nature Methods, 17, 261, doi: 10.1038/s41592-019-0686-2

Vulcani, B., Poggianti, B. M., Gullieuszik, M., et al. 2018, ApJL, 866, L25, doi: 10.3847/2041-8213/aae68b

Wang, J., Koribalski, B. S., Serra, P., et al. 2016, MNRAS, 460, 2143, doi: 10.1093/mnras/stw1099

Wang, J., Fu, J., Aumer, M., et al. 2014, MNRAS, 441, 2159, doi: 10.1093/mnras/stu649

Wes McKinney. 2010, in Proceedings of the 9th Python in Science Conference, ed. Stéfan van der Walt & Jarrod Millman, 56 – 61, doi: 10.25080/Majora-92bf1922-00a

White, D. A., Jones, C., & Forman, W. 1997, MNRAS, 292, 419, doi: 10.1093/mnras/292.2.419

Wilson, C. D., Warren, B. E., Israel, F. P., et al. 2009, ApJ, 693, 1736, doi: 10.1088/0004-637X/693/2/1736

Wolfire, M. G., Hollenbach, D., & McKee, C. F. 2010, ApJ, 716, 1191, doi: 10.1088/0004-637X/716/2/1191

Wright, E. L., Eisenhardt, P. R. M., Mainzer, A. K., et al. 2010, AJ, 140, 1868, doi: 10.1088/0004-6256/140/6/1868

Yajima, Y., Sorai, K., Miyamoto, Y., et al. 2021, PASJ, 73, 257, doi: 10.1093/pasj/psaa119

Yoon, H., Chung, A., Smith, R., & Jaffé, Y. L. 2017, ApJ, 838, 81, doi: 10.3847/1538-4357/aa6579

York, D. G., Adelman, J., Anderson, John E., J., et al. 2000, AJ, 120, 1579, doi: 10.1086/301513

Zabel, N., Davis, T. A., Smith, M. W. L., et al. 2019, MNRAS, 483, 2251, doi: 10.1093/mnras/sty3234

Zabel, N., Davis, T. A., Sarzi, M., et al. 2020, MNRAS, 496, 2155, doi: 10.1093/mnras/staa1513

Zahid, H. J., Dima, G. I., Kewley, L. J., Erb, D. K., & Davé, R. 2012, ApJ, 757, 54, doi: 10.1088/0004-637X/757/1/54